INVESTIGATION OF THE INFLUENCE OF CADMIUM PROCESSING ON $Zn_{1-x}Ga_2O_{4-x}$:Mn THIN FILMS FOR PHOTOLUMINESCENT AND THIN FILM ELECTROLUMINESCENT APPLICATIONS

By

Michael John Flynn, B.Sc. (Eng.)

Submitted to the School of Graduate Studies
In Partial Fulfillment of the Requirements
For the Degree
Doctor of Philosophy

McMaster University

LUMINESCENCE FROM CADMIUM PROCESSED ZN(1-X)GA2O(4-X):MN

DOCTOR OF PHILOSOPHY (2003) McMaster University

(Engineering Physics) Hamilton, Ontario

TITLE: Investigation of the Influence of Cadmium Processing on $Zn_{1-x}Ga_2O_{4-x}$:Mn Thin Films for Photoluminescent and Thin Film Electroluminescent Applications

AUTHOR: Michael John Flynn, B.Sc. (Eng.) (Queen's University)

SUPERVISOR: Professor A.H. Kitai

NUMBER OF PAGES: xii, 199.

To My Friends and Family, and Everyone Who Loves Me

Abstract

Cadmium processing of $ZnGa_2O_4$ films provides a new fabrication route for phosphor powders and thin films. It relies on the enhanced diffusion due to the large vacancy concentration left by the sublimation of cadmium. Photoluminescent powders can be made with a single high temperature firing. Thin film devices can be processed at a significantly lower temperature, expanding the range of available substrates.

Powders and thin films of $ZnGa_2O_4$:Mn were fabricated using starting materials in which between 0% and 50% of the ZnO was substituted by CdO. It was found that the emission spectra of the various compositions was unaffected by the change in composition, peaking at 504 nm, with the colour coordinates $x=0.08$ and $y=0.69$. The invariance of the emission spectrum is due to the spinel crystal structure exhibited by the compound. However, the maximum PL brightness was obtained from powders in which 10% of the ZnO had been substituted by CdO in the starting materials. The improved brightness is the result of better manganese incorporation which resulted from CdO sublimation during processing. This left a large vacancy concentration which enhanced the diffusion, and hence the manganese incorporation. In the case of thin films sputtered from cadmium processed targets, the composition of the films as deposited closely mirrored that of the target starting materials. The as deposited films were not luminescent and had to be annealed in vacuum in order to activate the manganese. EDX of these films showed that all of the cadmium had sublimed during the anneal. Very long anneal times also resulted in the loss of zinc. The decomposition products were amorphous or nanocrystalline. These films had an identical PL emission to the powders.

The loss of cadmium correlated with the onset of bright 254 nm photoluminescence in the films, indicating that cadmium loss aided in the activation of the manganese. This was the result of the enhanced diffusion due to the large vacancy concentration left by the sublimed material, which aided the incorporation and activation of the manganese. The cadmium in the sputtering targets also impacted the crystal structure of the films. Films from cadmium free targets exhibited a strong (111) x-ray diffraction peak, while those from cadmium processed targets more closely resembled the powder structure. The optimum thin film electroluminescent performance was obtained for films sputtered from targets processed with between 5% and 15% cadmium substituted for zinc. This was the result of improved diffusion during the anneals, due to the sublimation of cadmium oxide and the resulting large vacancy concentration. The best performance was obtained for films annealed at between 875°C and 900°C for 6-12 hours. These films exhibited both the maximum luminance (55 cd/m^2 at 60 Hz) and the lowest transferred charge (~20 $\mu C/cm^2$). This combined for a peak efficiency of 0.5 lm/W at 60 Hz). Beyond 12 hours at 900°C or temperatures higher than this, EL performance degraded due to the decomposition of the thin film. It was concluded that the luminescent performance of this material is strongly influenced by the loss of cadmium during processing. The enhanced diffusion afforded by the cadmium sublimation results in improved EL performance at annealing temperature lower that that of pure zinc gallate.

Acknowledgements

This thesis would not have been possible with out the support and direction of my supervisor, Adrian Kitai. I am also grateful for the guidance and support provided to me by my supervisory committee, John Preston and Jacque Barbier.

I also wish to express my thanks to the many members of the McMaster community who aided me throughout my years in graduate school: Jim Garret, Bruce Collier, Doris Stevanovic, Andy Duft, Jim Forster, Yosh Kitamura, Michael Palme, Paul Bray, Wen He Gong, George Timmins, Peter Jonasson. I would also like to thank the administrative staff, current and former, who smoothed the way for as much as they could. I am also grateful to the myriad others at McMaster who provided with aid and assistance during my time in graduate school.

Lastly, I would like to thank my family and friends, without your support none of this would have been possible.

Table of Contents

Section **Page**

List of Figures

List of Tables

Chapter 1

Introduction

The two most dominant information displays are the cathode ray tube (CRT) used in television sets and computer monitors, and the liquid crystal display (LCD) which is predominantly used in laptops but is also making inroads into the desktop monitor market. While these two technologies dominate high information density displays, other technologies like light emitting diode (LED) displays are used for large signs and vacuum fluorescent displays (VFD) are used in radios, VCRs and other low information content applications. Except for LEDs, all of these displays use inorganic phosphors as the source of light, although in the case of LEDs it is possible to alter the spectral output by incorporating phosphors into the plastic casing which encapsulates the device. By and large, the phosphors used in these displays were developed many years ago, and the improvements in these displays have been a result of improvements in other aspects of their respective technologies.

In the past decade or so, phosphor research has been reinvigorated by the emergence of several new display technologies. As its name suggests, field emission displays (FED) excite phosphors using a beam of electrons field emitted from a series of needle sharp electrodes formed by micro-lithography. Using phosphors developed for CRTs has proven impractical however, because these sulphide based phosphors decompose under electron bombardment, and the sulphur so produced attacks the emitter tips, degrading their performance. When developers use oxide phosphors in place of sulphides however, they find their performance is inferior at the operating voltages used in FEDs. This has spurred researchers to modify existing phosphors, or develop entirely new phosphors which can fulfill the promise exhibited by these devices.

A second display system which is making advances is the plasma display panel (PDP). In this device, each sub-pixel (a pixel consists of three sub pixels: red, blue and green) is excited by a small cell in which a gas discharge is excited. The radiation from this discharge then excites the phosphor. While the traditionally used for PL phosphors is mercury, there has been an increased interest in the past few years to develop phosphors which emit efficiently when excited by xenon, which does not have environmentally deleterious properties, and requires no heat to become a vapour.

A third display technology is thin film electroluminescence (TFEL). Although development of this display technology has been conducted since the 1960s, its mass production did not occur until the early eighties and their wide spread use has been restricted due to a lack of full colour capability (Ono, 1993). This technology has found limited use in niche applications where its high contrast and ruggedness are assets. Most of the research into phosphors for these displays has focussed on sulphides, and indeed the displays which are commercially available all use ZnS:Mn as the phosphor.

One area of TFEL phosphor research which is gaining interest is the study of oxide phosphors, the first of which was Zn_2SiO_4:Mn (Minami, 1991). Improvements in this phosphor were obtained by substituting germanium for silicon, for which there is complete solid solubility (Kitai, 1997a). This had the effect of lowering the processing temperatures required to form oxide TFEL devices.

Another promising TFEL phosphor is the green emitting $ZnGa_2O_4$:Mn. In this research, $ZnGa_2O_4$:Mn was modified by substituting CdO for ZnO in the starting materials. Films sputtered from targets fabricated from materials with 5-15% CdO exhibited improved performance, relative to the pure zinc gallate devices. The enhanced properties are the result of microstructural improvements, facilitated by the large vacancy concentration left by the sublimation of CdO during the high temperature anneal of the films. This vacancy concentration enhances diffusion rates during annealing, which lead to the improved properties. The discussion of these results is preceded by a presentation of luminescence and TFEL theory, followed by a summary of the work done to date in this phosphor system.

Chapter 2

Fundamentals of Luminescence

2.1 Introduction

A phosphor consists of two components, the activator(s) and the host. The activators are atoms or ions which absorb energy from an outside source and then release it as light. The host is the material into which the activators are incorporated as a dopant. When the energy is absorbed at one impurity center and re-emitted as light by another impurity, the phenomenon is referred to as sensitized luminescence. The light which is emitted by the activator is strongly affected by the interaction between the host material and the dopant atom. Phosphors are often differentiated by the means with which the luminescence is stimulated. When the excitation energy is supplied by photons of electromagnetic energy, the phosphor is referred to as photoluminescent (i.e. fluorescent lamps). Electron beam excited phosphors are called cathodoluminescent (i.e. a television screen). In this project, the phosphors are excited by the application of an electric field, and are therefore called electroluminescent phosphors.

Although different phosphors have been optimized for different excitation sources, some basic processes occurring within the material are independent of the means of excitation. In this chapter, these fundamental aspects of phosphors will be explained. Their specific application to electroluminescence will be left to Chapter 3.

2.2 Electron Transitions in Insulators : The Configurational Coordinate Model

There are a multitude of possible electronic transitions which can take place in a crystal. The most common of these are illustrated in Figure 2-1. In this diagram, the electronic states are shown by the dark horizontal lines, and their positions relative to the conduction and valence band are shown. The first transition is the fundamental electronic transition, in which both the initial and final states are intrinsic to the host crystal. The remaining three transitions shown all depend on the presence of impurity or defect states in the band gap. In phosphors, these defect states are associated with the dopants which are deliberately added to control the luminescence. In TFEL phosphors, the transition of interest is the localized state to localized state transition shown in 2-1

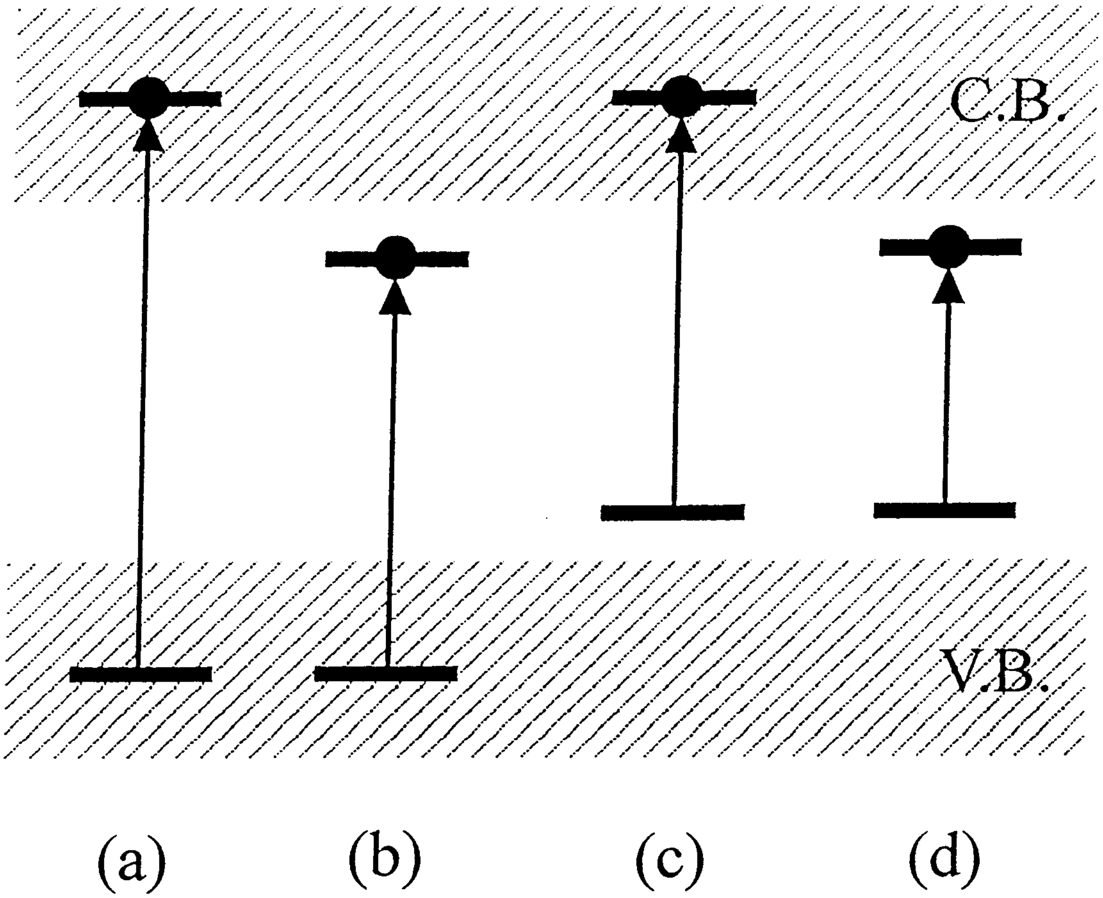

Figure 2-1) Energy states of transitions within and between energy bands in solids
a) band to band
b) band to localized state
c) localized state to band
d) localized state to localized state

(d). The reason for this will be made clear when electroluminescence is explained in more detail in Chapter 3.

Although the specific details of a phosphor's luminescence may be quite complicated, all the important features can be explained using a simple construct called a configurational coordinate diagram. This diagram shows the potential energy of the luminescent centre as a function of the configurational coordinate, which in the simplest approximation represents one vibrational mode of the defect centre. An example of a configurational coordinate diagram is shown in Figure 2-2. In this diagram, the lower parabola labeled g represents the ground state of the centre, while the parabola e is the excited state.

If the vibrational mode of the configurational coordinate is assumed to be the symmetric breathing mode, the coordinate, R, is simply the metal-ion distance. The coordinating ions are sometimes referred to as ligands, and for the purpose of our discussion here the two terms can be considered interchangeable. Although this assumption greatly simplifies the configurational coordinate treatment, it is not representative of real phosphor systems in which more complicated vibrational modes effect the luminescence (Imbusch, 1978) (These other vibrational modes will also couple to the dopant ion, and thus the shape of the emission spectrum is also dependant on the phonon density of states of the solid. Vibrational modes which lower the symmetry of the lattice sight also play an important role in increasing the emission strength of some centres.) The minimum energy of the ground state sits at R_0, while the excited state is

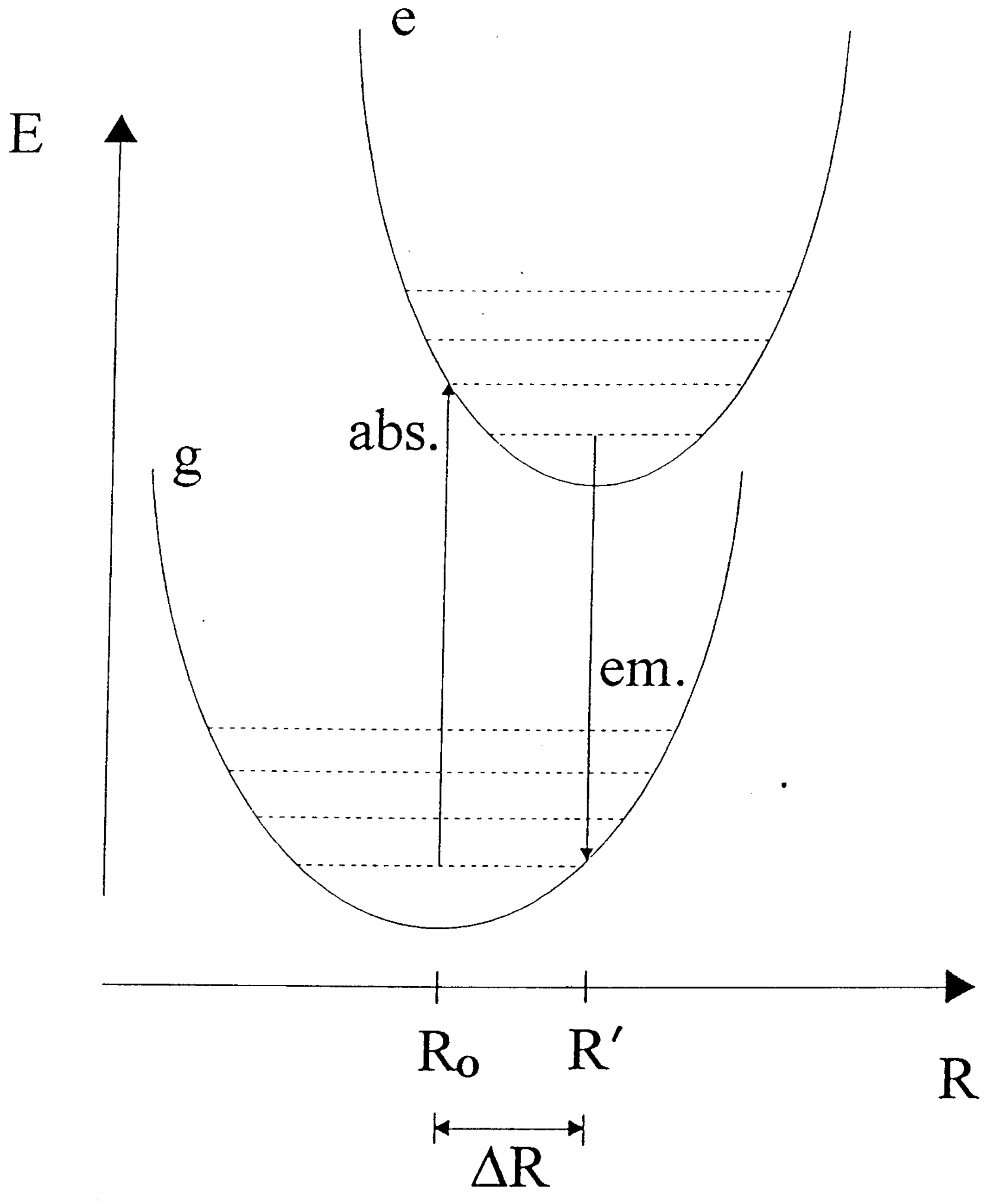

Figure 2-2) A configurational coordinate diagram showing the ground state and a single excited state. Vibrational levels are denoted by the dashed lines.

shifted relative to the ground state by a distance ΔR to sit at R'. The reason for this shift is that the change in electron density distribution around the ion when it shifts to the excited state alters the interaction of the centre with its neighbors, and hence the bond length changes.

Superimposed upon the potential energy parabolas are the vibrational levels of the system. The ion behaves as a quantum mechanical oscillator, vibrating about its equilibrium bond length. This is a straight forward problem which can be solved using relatively simple quantum mechanics (Brehm and Mullin, 1989). The solution is a series of quantised levels with energy $E_n = \hbar\omega(n+½)$, where $\hbar$ is Plank's constant divided by 2π, ω is the angular frequency of the vibrational mode and n is any integer ≥ 0 which labels each successively higher vibrational state. Like in the case of the classical pendulum, the ion is most likely found at the edges of the parabola.

During the absorption or emission of a photon, an electron in the luminescent centre moves from the ground state parabola to that of the excited state. The excitation or relaxation of the electronic system is assumed to occur much faster than the rearrangement of the ionic component. This is know as the adiabatic approximation. As a result of this, the configurational coordinate, R, does not change during the transition, just the energy of the electron (Hayes and Stoneham, 1985). This is referred to as the Frank-Condon principle. Once the electron is in its new state, the lattice relaxes to accommodate the new electronic configuration by emitting phonons.

If the system is at an extremely low temperature, the electron will be sitting in the lowest vibrational level of the ground state. If the system undergoes a transition to the upper state, the electron will move from the lower parabola to the upper. Because the solutions to the quantum oscillator problem show the highest probability at the edges of the parabola, this is where the electron will most likely end up after the absorption of the excitation energy. This is shown by the line marked abs. in Figure 2-2. The actual absorption band of a phosphor will have a finite width even at absolute zero due to the zero point motion of the ground state as well as the possibility of lower probability transitions which put the excited electron at a position within the excited state parabola. The result of this is a broad intensity band when absorption is plotted versus transition energy as illustrated in Figure 2-3.

Once the electron reaches the excited state, the system rearranges itself to accommodate this new electron configuration. During this process, the system releases phonons, and the electron will move down the upper parabola to a lower vibrational level. This relaxation results in the average metal-ion separation shifting from R_0 to R'. Finally, the electron will return to the ground state in a process mirroring the excitation. The electron goes from the minimum in the upper parabola to the ground state with no change in the configurational coordinate. Once in the ground electronic configuration, the lattice will relax to its original position at R_0 by emitting phonons.

During these transitions the total energy of the system must be conserved. Therefore all the energy released by both the radiative return to the ground state as well

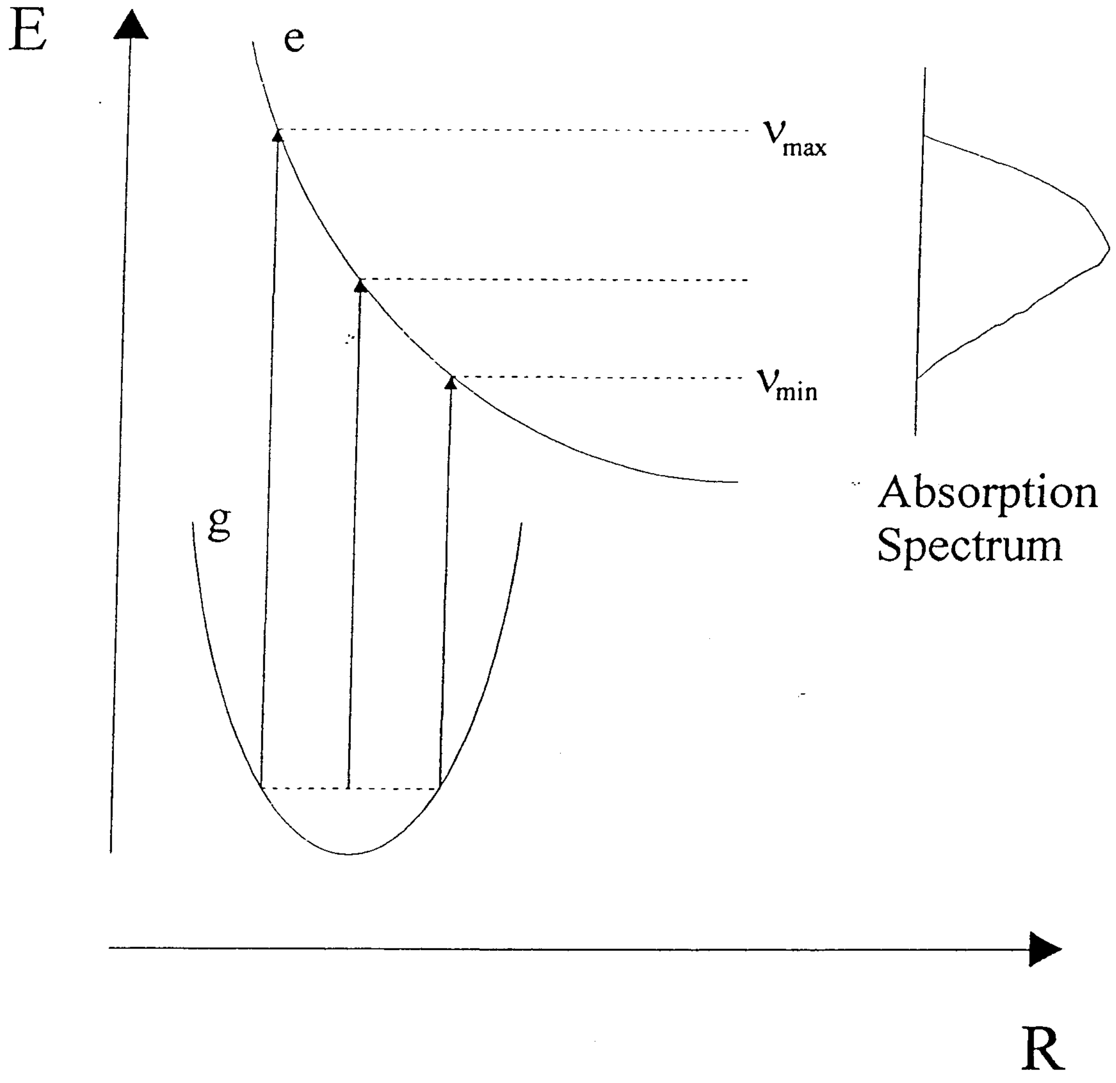

Figure 2-3) Configurational coordinate diagram showing the effect of higher vibrational levels on the shape of the absorption band.

as the phonons emitted during the relaxation of both the excited and ground states, must be equal to the absorbed excitation energy. Because energy is lost to phonons, the emitted photon must have less energy than the total absorbed energy. This difference in energy between the absorption and emission is called the Stokes shift. The larger the difference between R_0 and R_0', the larger the Stokes shift. This corresponds physically to the strength of the coupling between the luminescent centre and the host lattice. The stronger the coupling, the larger the Stokes shift.

Nonradiative return to the ground state can also be described using the configurational coordinate scheme. In these instances, all of the excitation energy is dissipated via processes which do not generate any luminescence. These processes occur in all phosphors and an understanding and control of them is vital to producing bright and efficient phosphors. There are two basic manners in which the electrons can deexcite nonradiatively. In the first case, the nonradiative route is intrinsic to the isolated luminescent centre. In the second possibility, the excitation energy is dissipated at a site removed from the initial absorption.

For nonradiative transitions occurring at the same centre as the absorption, we have two possible avenues to the ground state. The first of these possibilities is illustrated in Figure 2-4. Here, the centre has a single state into which the electron can be excited. Due to the coupling of the luminescent centre to the lattice, the excited state parabola is shifted relative to the ground state. In this situation, it is possible that a vibrational level of the excited state can overlap with one from the ground state. This

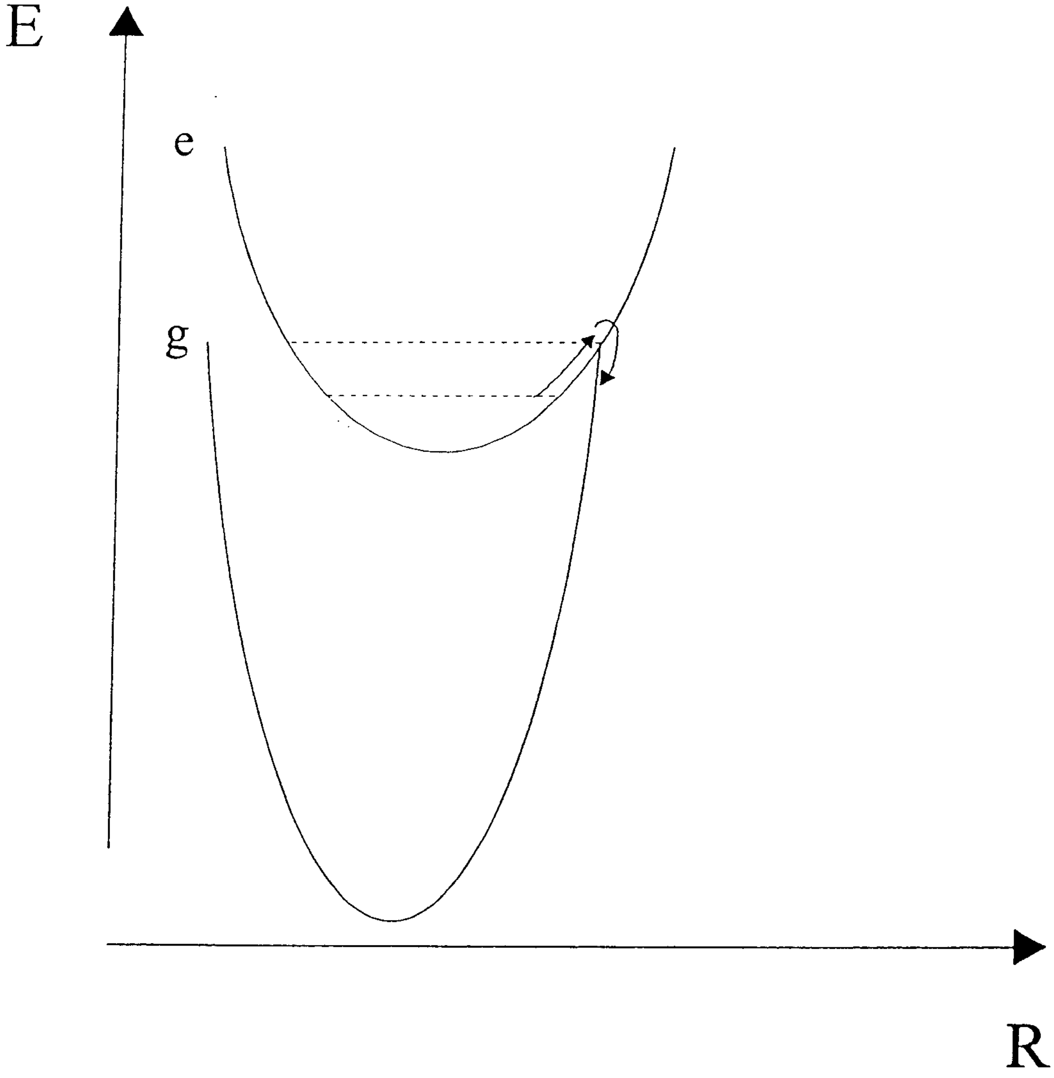

Figure 2-4) Nonradiative relaxation of an optical centre via the vibrational overlap of the ground and excited state.

allows for the thermal excitation of the electron from the excited state into the ground state. This transition will only occur near where the two parabolas overlap. This is a result of the quantum harmonic oscillator. Since an electron has the highest probability of being near the edge of the parabola, as opposed to in the centre, the only region in which there is a reasonable probability of the electron shifting from one electronic state to the other is near where the two parabola meet. This would be followed by a relaxation of the ground state via the emission of phonons.

The second nonradiative relaxation route can occur if the centre has several relatively closely spaced electronic excited states. This is shown schematically in Figure 2-5. Similar to the single excited state situation, this transition is dependent on an overlap between the vibrational levels of the various states. As for the single electron case, the transition will have the highest probability of occurring if enough thermal energy can be supplied that the electron is in a vibrational state which places it near the intersection of the parabolas defining the two states. Once the electron finds itself back in the ground state configuration, it will give up its remaining energy through phonon emission.

It is also possible for the energy to be dissipated at sites removed from the initial excitation. This is referred to as luminescent quenching. In this case, there is an electric or magnetic multipolar interaction between the two centres. Rather than emitting a photon, the energy is directly coupled from one centre to another. When the centre to which the energy is coupled is the same ionic species as the site of the initial excitation,

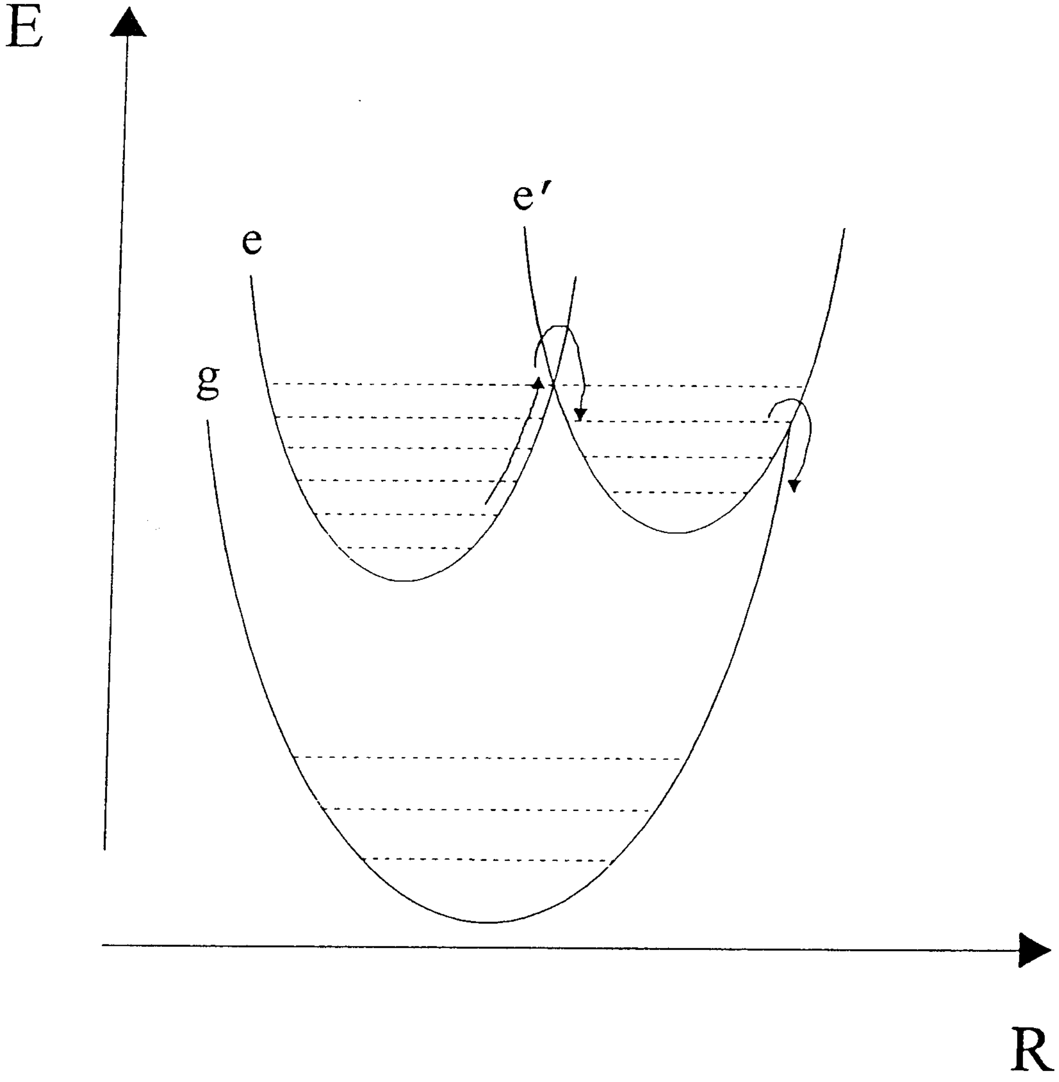

Figure 2-5) Nonradiative relaxation of an optical centre via the vibrational overlap between two closely spaced excited states, e and e′ , and the ground state.

the energy can eventually migrate to a site at which nonradiative relaxation can occur easily. This effect occurs in virtually all phosphors, and is referred to as concentration quenching. The dopant concentration at which this effect becomes important will depend on both the dopant ion and the lattice into which it is substituted. There are several forms for the centre at which the nonradiative deexcitation occurs: an intrinsic host defect; dopant complexes (i.e. dopant atoms forming some sort of more complex, coupled centre); impurity atoms which have found their way into the host, particularly transition metal elements. These defects tend to release the excitation energy as a combination of phonons (heat) and photons of infra-red energy.

2.3 Quantum Mechanics and Luminescence

Although the configurational coordinate scheme is strictly a qualitative description of luminescence, it is standing on firm ground. A quantum mechanical description of luminescence can justify all the arguments used in the configurational coordinate model. It provides the rigorous foundation which allows more complicated optical phenomena to be explained within the context of the more qualitative simple model. Most importantly, it explains the complicated shape of low temperature optical transitions.

For a transition between two states to occur they must be connected by some suitable interaction. In the case of display phosphors, this is the electric dipole interaction. The probability of a transition occurring, P_{fi}, is determined by the probability amplitude of the transition:

$$P_{fi} = \left|\int \Psi_f^* e\mathbf{r}\Psi_i d\tau\right| \tag{2-1}$$

where Ψ_i and Ψ_f are the eigenfunctions of the initial and final states and $e\mathbf{r}$ is the electric dipole operator. In the case of the one electron atom, this results in the familiar selection rules:

$$\Delta l = \pm 1 \tag{2-2a}$$

$$\Delta m_s = \pm 0 \tag{2-2b}$$

with l being the angular momentum quantum number and m_s is the spin quantum number. Equation (2-2a) is the parity selection rule, and forbids transitions between any initial and final state which are formed by the same orbital type (i.e. no s→s or p→p transitions). Equation (2-2b) is the spin selection rule which forbids any transition in which the spin of the electron switches orientations.

In multi-electron atoms the situation becomes more complicated. The behavior of the optically active electrons is no longer determined strictly by the interaction between the electrons and the nucleus. It now becomes important to take into account the interactions between the various electrons in the atom or ion. There are three interactions which must be elucidated. These are:

1) The coulombic interaction between the various electrons

2) The spin-orbit interaction, which couples the spin and orbital angular momentum of the electrons

3) The exchange interaction, which couples the spins of the electrons in the atom.

The first of these effects causes the electrons in the outer shell of the atom to experience a non-spherically symmetric potential, as would be experienced by a single electron orbiting a nucleus. The result of the spin-orbit interaction is that the total angular momentum will play a role in the selection rules. Finally, the exchange interaction will partially dictate how the electrons organize themselves across the available energy states.

These various effects are typically handled using the LS coupling scheme. This treatment allows for accurate calculation of the properties of atoms with intermediate atomic number, such as the first and second row transition metal atoms and ions. It proves less effective for heavier elements such as the lanthanides. A more detailed explanation of LS coupling can be found in numerous excellent texts (Eisberg and Resnick, 1985; Cotton, 1966; Sharpe, 1992). The result of this coupling is a more complicated set of selection rules:

1) The transitions only occur between states with different quantum numbers *n* and *l* of a single electron. This means two or more electrons can not be simultaneously involved in transitions between subshells.

2) The restriction on the *l* quantum number is the same as the single

electron case (i.e. $\Delta l = \pm 1$).

3) Due to coupling between the various electrons the total spin quantum number s', the total orbital angular momentum l' and the total angular momentum j' are also restricted. The first two of these terms are obtained by determining the vector sum of the spin and orbital angular momenta respectively. The total angular momentum is simply the sum of both the spin and orbital momenta. Mathematically, these can be expressed by:

$$\Delta s' = 0 \tag{2-3a}$$

$$\Delta l' = 0, \pm 1 \tag{2-3b}$$

$$\Delta j' = 0, \pm 1 \tag{2-3c}$$

It should be noted that these selection rules have been derived for electric dipole radiation. Transitions which violate these selection rules can be observed and are the result of magnetic dipole or electric quadrupole radiation. However, because the transition rates for these forms of radiation are extremely low they are not of significance for display phosphors.

2.4 Energy Levels of Transition Metals in Crystals

Transition metals are characterized by a partially filled d-level. In the case of the first row transition elements such as iron, chromium and manganese, the partially filled level is the 3d shell. This has two important effects. The first is that the ions can incorporate in a number of different oxidation states, and hence can exist in numerous diverse crystal environments. The second effect is that there are in general several optically active electrons (i.e. electrons which are able to move between allowed energy levels via the absorption and emission of photons of electromagnetic radiation. In this particular treatment band-to-band transitions are being ignored, although these can also be important electronic transitions in cases such as LEDs). It is the interaction of these optically active electrons with their environment that determines the optical properties of the ion.

When the ion is placed in a crystal, the electron energy levels are disturbed by the electric field associated with the neighboring ions. If the field associated with the coordinating ions is spherically symmetric, the only effect is to raise the energy of all five d-shells by an equal amount. In real crystals though, the field is not spherically symmetric, but rather is determined by the symmetry of the host crystal. This reduced symmetry crystal field lifts the degeneracy of the d-levels of the transition metal ion.

The effect of the crystal field is most easily visualized for the case of a single d electron in an octahedral crystal field. For the purposes of this discussion, we will assume that the transition element lies at the origin of a three dimensional coordinate system, and the six coordinating ions are arrayed along the three axes, each equidistant from the origin. In the first approximation, the coordinating ligands are treated as point charges, which are arranged symmetrically about the central metal ion, along the x,y and z axes. The five different d-orbitals have different spatial geometries, as illustrated in Figure 2-6. Because of these different orientations, the electrons spend different amounts of time in the region of the coordinating charges. Because electrons in the $d_{x^2-y^2}$ and the d_{z^2} orbitals are focused towards the ligands, the repulsive electrostatic interaction raises the energy of these two levels relative to the case of a spherically symmetric charge distribution. The d_{xy}, d_{xz} and d_{yz} orbitals on the other hand are directed into regions of space between the ligands. This results in a lowering of the energy of these orbitals with respect to the spherically symmetric case. The pair of higher energy orbitals is labeled the e_g level, while the three lower energy levels are labeled t_{2g}. The total energy of the five orbitals is equal to that of the case for a spherical charge distribution. Therefore, the combined energies by which the t_{2g} orbitals are lowered is equal to the combined energy by which the e_g orbitals have been raised. The total energy separating the two sets of levels is labeled Δ_o for the octahedral case. This is illustrated schematically in Figure 2-7. The magnitude of Δ_o is

$$\Delta_o = \frac{5}{3}\left\{\frac{ze^2\langle r^4\rangle}{a^5}\right\} \tag{2-4}$$

where ze is the anion charge, $\langle r^4\rangle$ is the average value to the fourth power of the distance of the electron from the nucleus (this is typically ~ 1Å for 3d electrons) and a is the bond

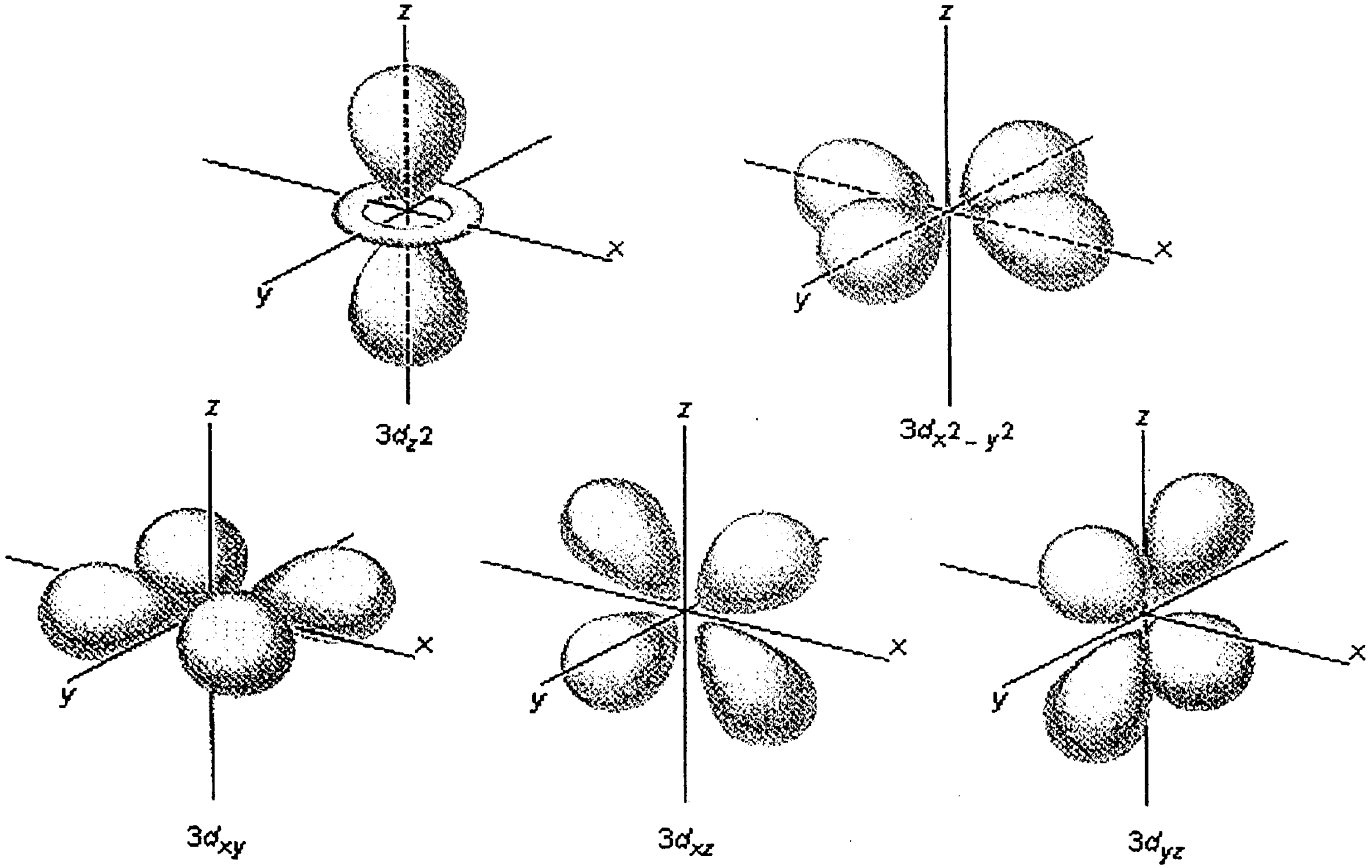

Figure 2-6) Spatial orientation of the d-orbitals

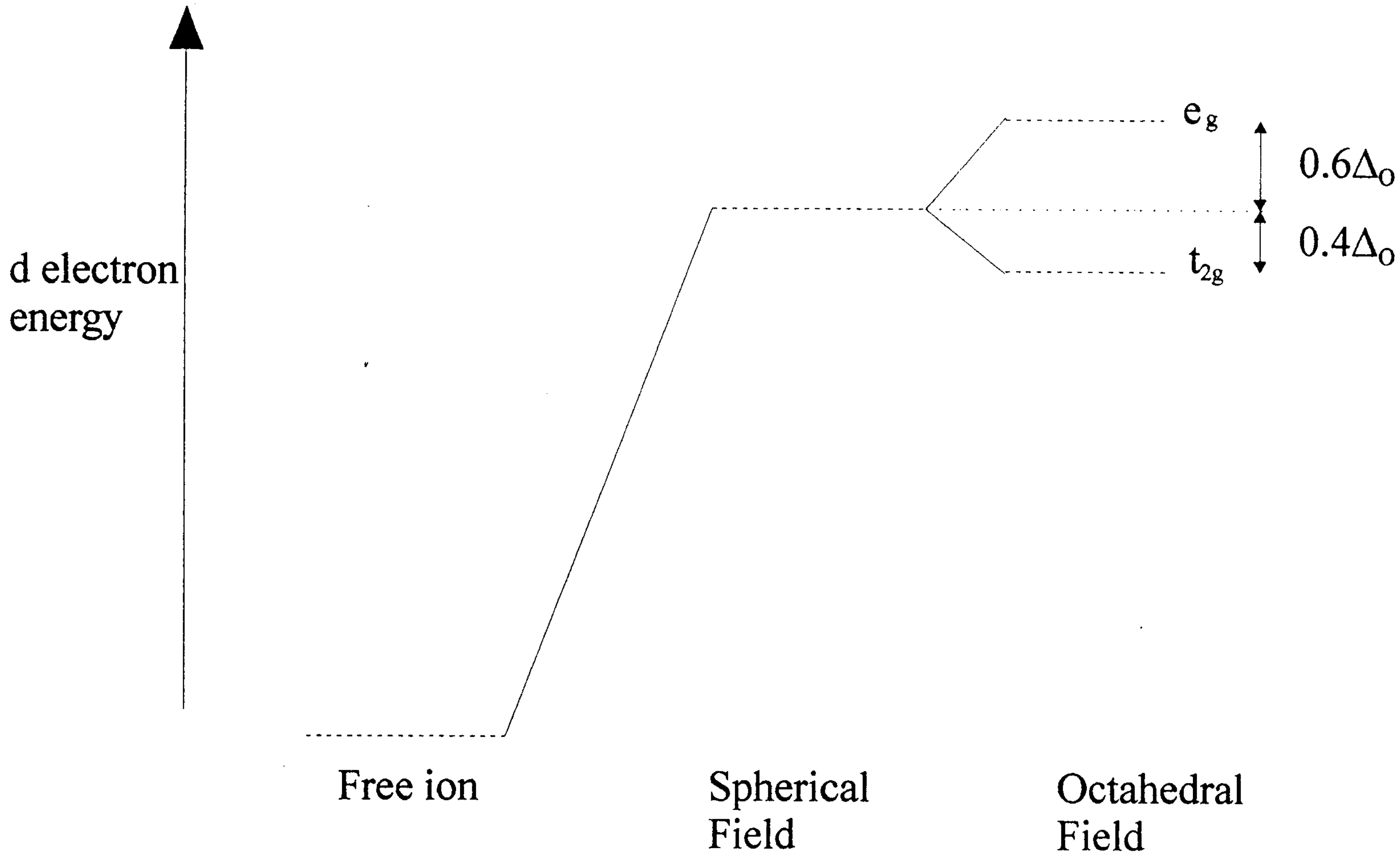

Figure 2-7) The effect of a spherical and an octahedral charge distribution on the energies of the d electrons.

length. As can be seen, the splitting depends strongly on bond length. This equation is derived by assuming the coordinating ligands are point charges.

If the optically active ion is substituted into a tetrahedrally coordinated crystal site, the splitting is not as intuitive. A sketch of this situation is shown in Figure 2-8. Although it is not immediately obvious, because both the octahedral and tetrahedral cases are both subclasses of cubic symmetry, they have similar d-level splitting. The two sets of levels are simply switched, with the t_{2g} levels being raised in energy while the e_g levels move lower. Total splitting is reduced, with the separation for the tetrahedral case being Δ_t=-4/9Δ_o. The negative sign indicates that the order of the terms is inverted.

As for the case of an isolated atom or ion, the situation becomes more complicated when more than one electron is involved. Once again spin-orbit, exchange and coulombic interactions must be taken into account. This problem was tackled separately by Orgel (1955) and Tanabe and Sugano (1954a;1954b). The result of both sets of analysis was a set of diagrams, one for each d-ion, which expresses the energy separating each distinct electronic configuration versus the strength of the crystal field. The diagram for a $(3d)^5$ ion is shown in Figure 2-9. The crystal field strength is plotted along the abscissa, while the relative energy of the various configurations is plotted on the ordinate. All excited configurations are plotted relative to the ground state configuration. The terms are labeled by a capital letter representing the degeneracy (A singly, E doubly and T triply degenerate). The superscript is the spin multiplicity (2S+1 where **S** is the total spin) and the subscript is the total angular momentum (**S**+**L**, where **L**

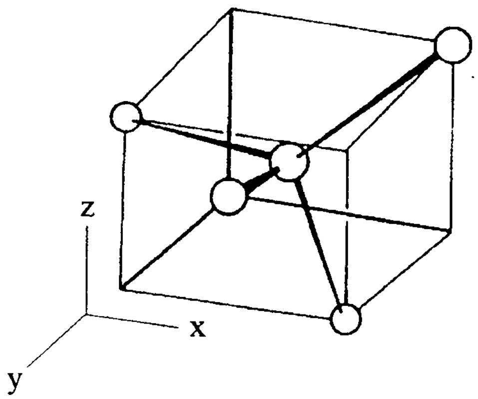

Figure 2-8) Orientation of ligands relative to a tetrahedrally coordinated ion (after, Atkins 1978).

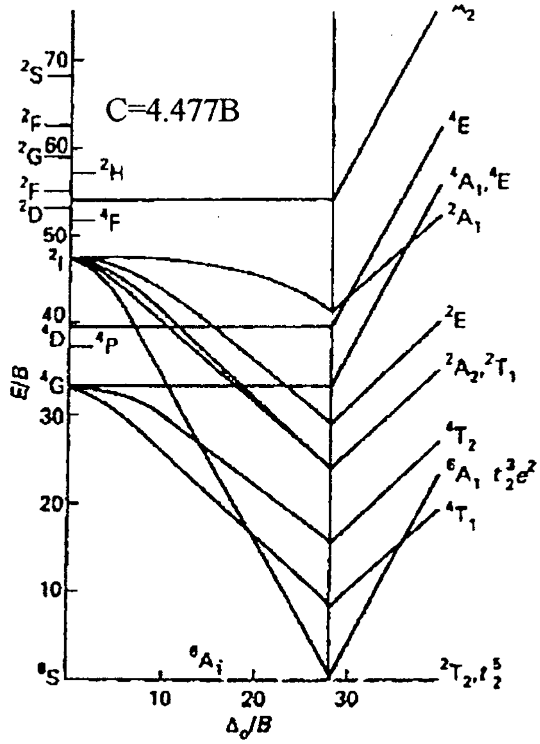

Figure 2-9) Tanabe-Sugano diagram for a d^5 ion (after Tanabe and Sugano, 1955).

is the total orbital angular momentum).

Both axes are normalized by the Racah B parameter, which is a measure of the electron interaction. There are three Racah parameters (A,B and C). The A term is required if the absolute energy of a configuration is needed, while the C term is more or less constant for the first row transition elements. Therefore, in order to obtain the energy levels of an ion, one needs only the crystal field strength and the Racah B parameter. Unfortunately, these are not easily evaluated. In practical situations, the problem is approached from the opposite direction. The energy of several configurations is measured, and the Tanabe-Sugano diagram is used to determine approximate values of Δ and B.

The Tanabe-Sugano diagram is divided into two regions. At low values of Δ is the weak field case. This is the situation below $\Delta_o/B \lesssim 28$. Here, the splitting of energy levels by the crystal field is treated as a perturbation of the energy levels of the free ion. As the crystal field strength increases up to $\Delta_o/B \approx 28$ the ground state is the $^6A_1$ configuration. At high values of $\Delta_o/B \geq 28$ is the strong field case. Here, the interactions between the various electrons are treated as a perturbation of the crystal field split one electron states. Note that the ground state energy level changes from the $^6A_1$ configuration to the $^2T_2$ state. In the low field case, the energy required to spin pair electrons in a single d-orbital is greater than the energy required to promote an electron to a higher energy orbital, and hence there is a tendency for the electrons spins to line up. Since this results in a large total spin quantum number, this is referred to as the high spin case. In strong crystal fields, the opposite effect occurs. The electrons will spin pair, resulting in the low spin configuration. Below $\Delta_o/B \approx 28$, the five different d shells each contain a single electron with all five spins aligned. Above $\Delta_o/B \approx 28$, the exchange energy is less than the splitting of the different energy levels, and the total energy of the ion can be reduced by moving electrons from the higher energy d levels into the lower levels, with electrons paired up with opposite spins.

Diagrams were developed for ions with between 1 and 9 d electrons octahedrally coordinated. The d^1 through d^5 configurations were determined by evaluating ions with between 1 and 5 electrons. The remaining configurations were evaluated by performing identical calculations, but using holes instead of electrons. The diagrams can also be applied to tetrahedrally coordinated ions, since both octahedral and tetrahedral configurations are subsets of cubic symmetry. For the tetrahedral case the term splitting can be described by:

$$d^n_{tet} = d^{10-n}_{oct} \tag{2-5}$$

where n is the number of d electrons. The most interesting aspect of this symmetry is that the term splitting is the same for d^5 ions in both tetrahedral and octahedral configurations. It should be noted however that the values of both B and Δ are different and hence the absolute energies separating the levels will be quite different. Due to the significantly larger value of Δ in the octahedral complexes these are shifted to lower energies than for the tetrahedral case. It is also interesting to note that for the case of Mn^{2+}, there are no known low spin complexes with tetrahedral coordination.

Because there is an abrupt change in the approximations used to describe crystal field and electron interactions, Tanabe-Sugano diagrams can only be used qualitatively. While the lack of concrete information is somewhat unsatisfying, the diagrams do provide solid guidance when attempting to explain observed trends. They allow the correlation between host lattice properties and the absorption and emission spectra, since the bonding between the lattice and the dopant will define the energy levels of the optical centre. It should be noted that while the values of Δ and B are also affected by the specific transition metal element and its charge state, the difference in spectra between two different metal ions tends to be quite large. Therefore, when developing new phosphors, the optical centre is chosen first, and the absorption and emission properties are adjusted by manipulating the host crystal.

Chapter 3

Thin Film Electroluminescence

3.1 Introduction

Electroluminescence (EL) is the emission of light with the application of an electric field. The most commonly used form of electroluminescence is injection electroluminescence. In this phenomenon, light is generated by the recombination of electrons and holes injected across a forward biased p-n junction (Sze, 1985). These devices use single crystal, direct-gap semiconductors. The other form of electroluminescence is the high-field variety. Here, the light is generated by the application of a large electric field across a phosphor material, and is the form of electroluminescence in which we are interested here.

High-field electroluminescence was first observed by Destriau in the 1930s

(Destriau, 1936). Light was generated when a large field was applied across a suspension of Cu doped ZnS suspended in oil. The technology was largely ignored until the 1950s when attempts were made to use powder EL phosphors for wall lighting (Tannas, 1985). These devices were limited by their low luminance and efficiency, as well as poor device lifetimes.

Powder electroluminescence made major leaps throughout the 1960s with the goal of producing multiplex addressed information displays (Ono, 1993). These devices were operated under both ac and dc drive conditions (Vecht et al., 1968). These devices were made possible by advances in materials science and device fabrication technology. Powder electroluminescent devices have now been used in such applications as night/emergency lights and backlights for liquid crystal displays.

Thin film devices using a single insulator showed the potential of this technology for display applications (Kahng, 1968; Chase et al., 1969). An important breakthrough in EL came in 1967 when the double insulating thin film electroluminescent (TFEL) device structure was proposed (Russ and Kennedy, 1967). This device was the foundation of virtually all EL devices made today. In this form, the phosphor layer is sandwiched between a pair of dielectric layers. Using this structure the first stable, high brightness, efficient devices were fabricated by Sharp corporation (Inoguchi et al., 1974). These devices showed the potential for TFEL as a viable information display technology. The first mass produced monochrome TFEL display came on the market in 1983 (Takeda et al., 1983).

Since Sharp first demonstrated the potential of this technology a great many advances have been made, driven by the demands of the display industry. Multicolour displays were introduced by Planar Systems shortly after the first monochrome devices (Coovert et al., 1982). These displays have been relegated to niche markets due to the lack of full colour capabilities. The development of full colour displays has been hampered by the lack of a suitable blue phosphor.

The current market for TFEL displays involve applications in which the high contrast, wide viewing angle and ruggedness of these displays give a sufficient advantage over cathode ray tubes or liquid crystal displays. These types of applications include medical equipment as well as military and industrial applications.

3.2 Device Structure

The original thin film electroluminescent device was based on a double insulating structure shown in Figure 3-1. The phosphor layer is sandwiched between two dielectric films. These three films are deposited on an indium-tin oxide (ITO) coated high-temperature glass substrate, such as Corning 1737 (useful to ~666°C). The ITO is a transparent degenerate semiconductor which is used as one of the electrodes. A metal electrode deposited on top of the film stack completes the device. Light is emitted when an ac signal is applied across the thin film stack. This light is observed by the viewer through the glass substrate.

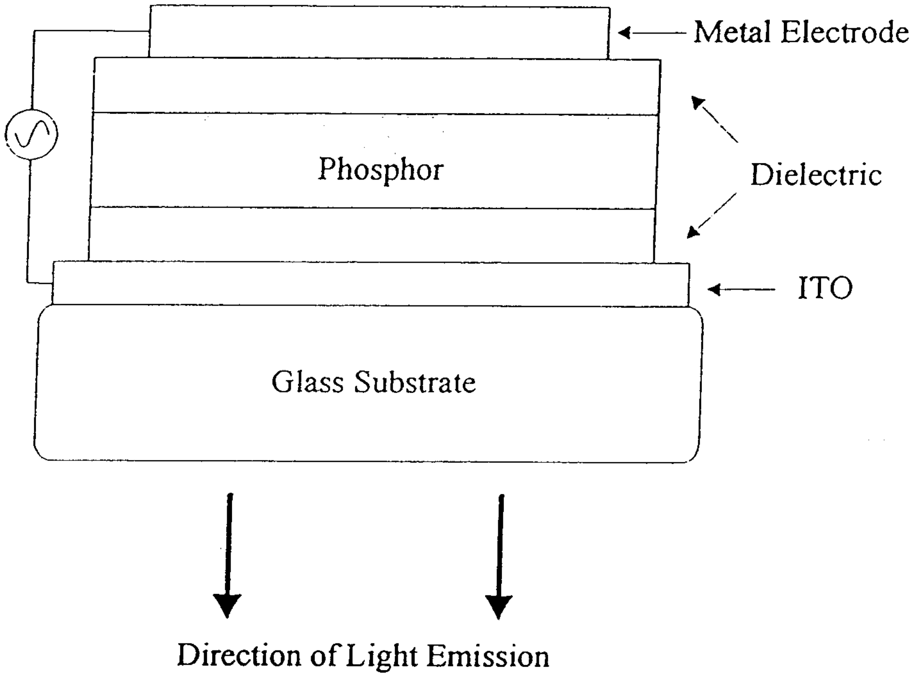

Figure 3-1) The double insulating TFEL device.

An alternative to this design is the so called inverted structure, shown in Figure 3-2. Here the metal and ITO electrodes are reversed, and the observed light is no longer viewed through the substrate. The advantage of this design is that the substrates are no longer required to be transparent, opening up a wider range of materials options. In one variation of the inverted structure, a high dielectric constant insulator such as barium titanate is used both as the substrate and the bottom dielectric layer (Nanto et al., 1988). The advantage of a ceramic substrate is that it allows post-deposition film processing at much higher temperatures (>1000°C). As will be shown in the following section, the high dielectric constant, k, of the substrate enhances the electrical performance of the EL cell.

One important thing to note about the device shown in Figure 3-2 is the lack of a second dielectric layer. The device will still luminesce with one electrode directly on the phosphor, however it is not as bright or efficient. However, it does make the fabrication simpler, so for comparing different phosphors this is a convenient device structure.

3.3 Device Operation and Physics

Light is emitted from a TFEL device when a large electric field ($>10^6$ V/cm) is applied across the thin film stack. When the field reaches a threshold strength determined by the phosphor and dielectric layers, there is an electrical breakdown within the phosphor layer and light is emitted. This threshold behaviour, along with the

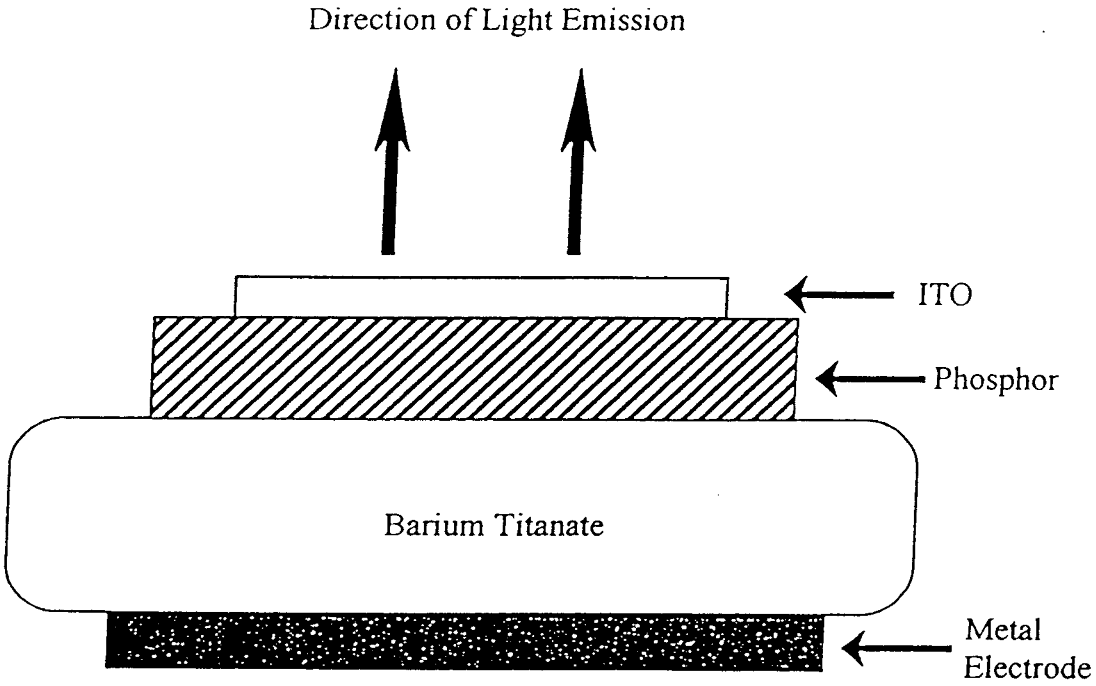

Figure 3-2) The inverted TFEL structure using a ceramic substrate as the only insulating layer.

simplicity of the device structure leads naturally to the equivalent circuit illustrated schematically in Figure 3-3.

The device is modeled as two series capacitors, C_d being the dielectric layers and C_p the phosphor layer. In parallel with the phosphor layer is a pair of back-to-back Zener diodes. Below the threshold, the application of a voltage results in a build up of charge on the capacitors. Once the reverse bias breakdown voltage of the Zener diodes is reached, the phosphor layer is short circuited and charge flows. Because of the breakdown characteristics of the diodes, a very large current will flow at very small voltages above threshold. It is while this current is flowing that light emission is observed.

While this adequately describes the electrical behaviour of the device it provides no fundamental insights into what is actually happening inside the film stack. Furthermore, it says nothing about the luminescent characteristics of the phosphor layer. This electrical behaviour must therefore be rationalized with the device structure and the luminescent properties of the phosphor layer. This understanding is facilitated by examining the band diagram for the device when it is operating above threshold, as shown in Figure 3-4.

There are four basic processes which occur in every TFEL device. The breakdown is initiated by electrons which tunnel out of interface states as shown in Figure 3-4 (a). These electrons are then accelerated by the high electric field within the phosphor layer. Once the electrons gain enough energy from the field they can either

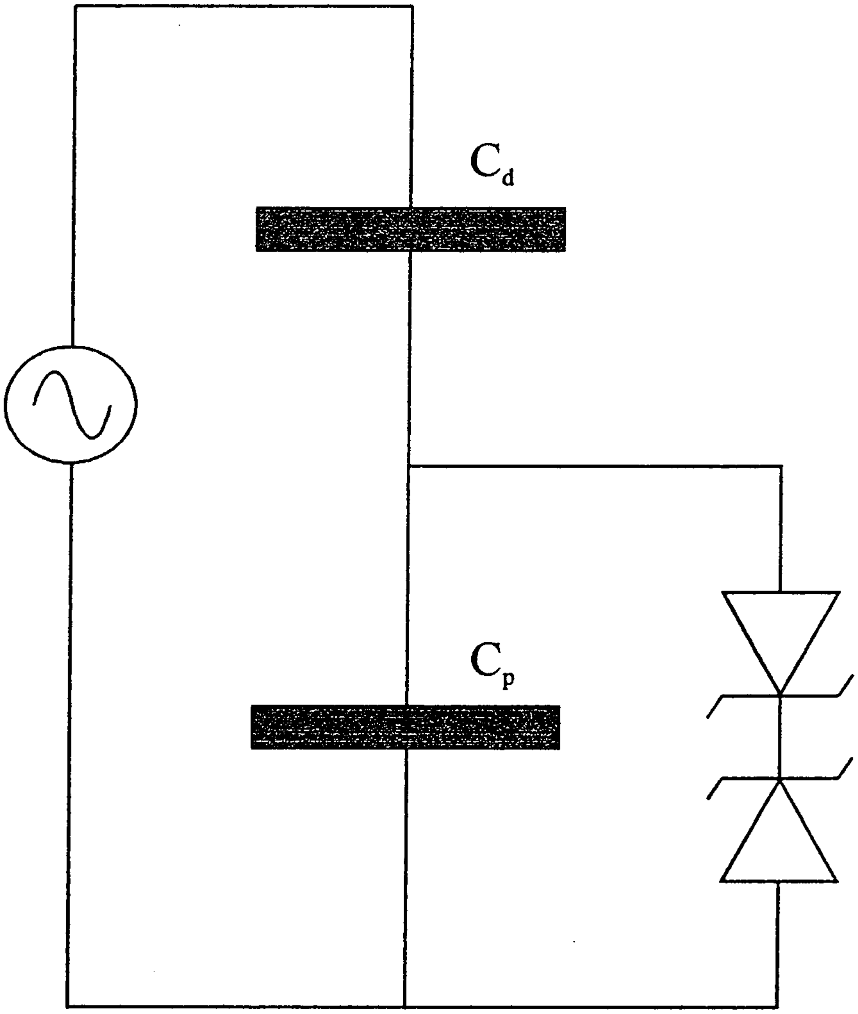

Figure 3-3) The equivilant circuit of a simple TFEL device.

impact excite luminescent centers (3-4 (b)) or ionize centres thus adding to the avalanche current (3-4 (c)). Finally, when the electrons reach the opposite side of the phosphor layer, they are once again trapped at interface states, to be released again when the polarity is reversed (3-4 (d)).

The diagram shown in Figure 3-4 is for the case of a double insulating layer device such as that illustrated in Figure 3-1. In this case, the injection is from the insulator-phosphor interface for both polarities. Electrons are injected from this interface via tunnel emission from interface states (Tanaka et al., 1999). This is made possible by the band bending within the phosphor, induced by the electric field. For tunnel emission, the current density, J, depends predominantly on the electric field strength, E, and is described by:

$$J \approx E^2 \exp\left(\frac{-4(2m^*)^{1/2}(q\Phi_B)^{3/2}}{3q\hbar E} \right) \tag{3-1}$$

where m^* is the electron effective mass, q is the electronic charge, Φ_B is the barrier height and $\hbar$ is Planck's constant divided by 2π. The barrier height is the depth of the electron traps below the conduction band edge of the phosphor layer. Trap depth and density depend not only on the phosphor and insulator materials, but also on the fabrication process. While this has been studied for the case of metal-semiconductor junctions, little work has been done for the case of insulator-insulator interfaces. Some work has been done on interface control to enhance tunnel injection, but has only shown limited success (Rack and Holloway, 1998).

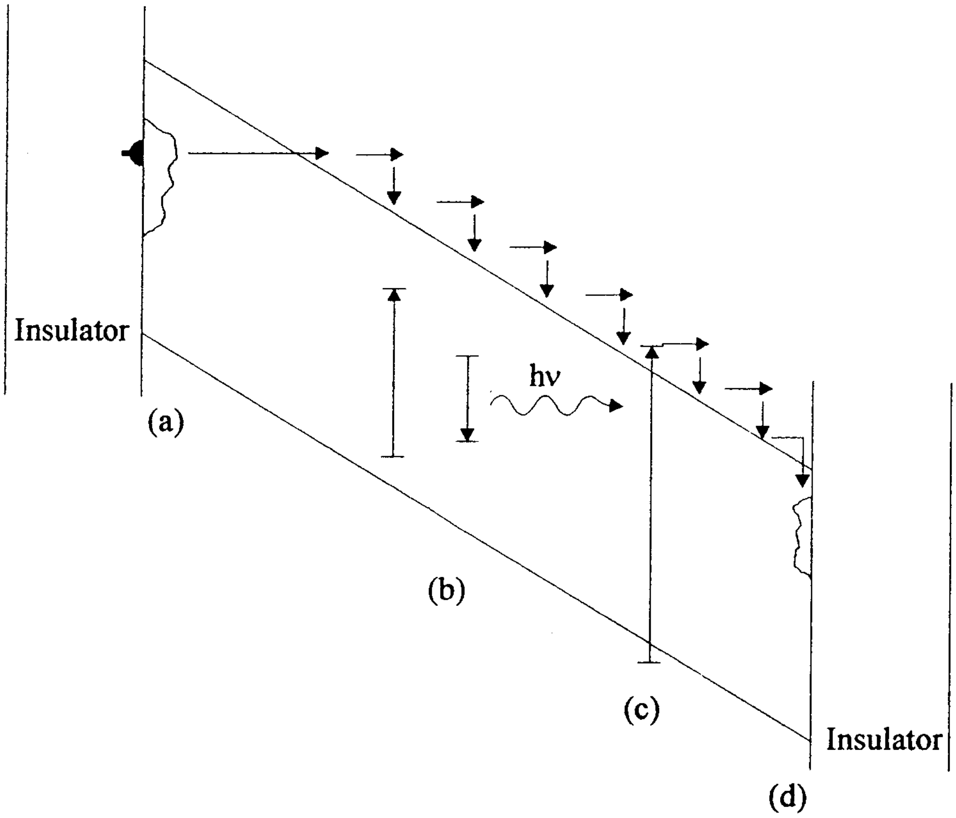

Figure 3-4) Band diagram showing the processes occuring inside the phosphor layer at voltages above threshold. (a) tunnel injection of electrons from interface states. (b) Excitation of luminescent centre and emission of light. (c) Avalanche multiplication of charge. (d) Recapture of electrons at interface states.

In the case of the inverted device structure of Figure 3-2, the electrode directly on the surface of the phosphor must be examined separately. In this case the interface is between a conductor and an insulator. The injected charge originates not from interface states, but rather from filled electron states near the Fermi level of the electrode. The barrier encountered by the electrons is referred to as a Schottky barrier. Electrons are thermionically emitted from the electrode into the insulator. When an electric field is applied, the barrier between the insulator and the electrode is lowered, thus increasing the current density. The combined temperature and electric field dependent current density is described by:

$$J \approx AT^2 \exp\left(\frac{-q\Phi_B - (qE/4\pi\varepsilon_P)^{1/2}}{kT}\right) \tag{3-2}$$

where A is a constant, T is the absolute temperature, ϵ_P is the phosphor dielectric constant and k is Boltzmann's constant.

The most significant difference between the two injection modes is that in the case of the Schottky barrier, injection can occur at zero electric field. In practice, the Schottky barrier is lower than the barrier for tunnel emission, which results in charge injection at lower electric fields. This manifests itself in a pronounced asymmetry in the EL brightness as a function of voltage polarity (Mueller-Mach et al., 1996,1999).

Once the electrons are injected into the phosphor, they are accelerated to high enough energies to impact excite luminescent centres or electron-hole pairs. Electron-hole pairs do not contribute significantly to the luminescence, since the large electric field immediately accelerates them to high energies which makes their capture by luminescent centres unlikely. What the electron-hole pairs do cause is the formation of a space charge region. Holes tend to be captured by deep traps, while the electrons travel to the phosphor-dielectric interface, thus polarizing the device. This space charge orientation is then reversed when a voltage pulse of the opposite polarity is applied.

Surprisingly, electric current and space charge generation has been treated as an afterthought by most researchers. The space charge formation is assumed to be self-limiting. The field induced by the space charge acts to counter the generation of more electron-hole pairs, and therefore for a given initial applied field there is a maximum amount of transferred charge possible. Although the amount of work in this area is limited, recent SPICE based models have been able to very accurately simulate the electrical behaviour of ZnS:Mn devices. These models are considerably more complicated than the simple back-to-back Zener diode model shown in Figure 3-3. They include components to account for space charge and defect states, which result in much better agreement with the measured device characteristics (Bender and Wager, 2000).

Excitation of the luminescent centres themselves is also a relatively poorly understood phenomenon. The impact excitation rate, P, is:

$$P \propto \int_{\varepsilon_o}^{\infty} \sigma(\varepsilon,\gamma) f(\varepsilon) d\varepsilon \qquad (3\text{-}3)$$

Where ε_o is the threshold energy for excitation, $\sigma(\varepsilon,\gamma)$ is the impact excitation cross-section to the excited state γ and $f(\varepsilon)$ is the energy distribution of the electrons in the phosphor. The impact excitation cross section has proven difficult to determine, even in the case of ZnS:Mn, the most extensively studied EL phosphor. Calculations taking into account dielectric screening, electron scattering vectors and electric dipole transitions in ZnS:Mn have yielded cross sections several orders of magnitude too small to be useful (Allen, 1989). It is believed that a failure to take into account exchange and correlation effects led to the discrepancy. The electron energy distribution is also poorly understood, and has proven difficult to measure and model. Such experiments have only been done for ZnS and ZnSe, with most of the effort focussed on the former. Hot-electron cold cathode measurements of electron energies have proven inconclusive, with electron energies ranging from 5-11 eV (Müller et al., 1991). These experiments were repeated, and the electron energy distribution was found to peak in the 5-7 eV range (Carkner and Kitai, 1992). Theoretical models have yet to predict electron energies approaching the values measured experimentally.

3.4 Electrical Behaviour of TFEL Devices

The simple model which has been presented for TFEL devices allows for a rather straight forward analysis of the electrical properties of EL devices. The analysis is based upon the assumption that the insulators act as ideal capacitors and that the phosphor layer is an ideal capacitor below the threshold voltage, V_{th}. Above threshold, a current flows within the phosphor layer and light is emitted. The analysis applies both to single insulating and double insulating layer devices. In the double insulating case, the capacitances of the two layers are connected in series to give a total insulator capacitance.

Below threshold, the applied voltage falls across both the insulator and the phosphor layer:

$$V_a = V_I + V_p, \quad V_a < V_{th} \tag{3-4}$$

Where V_a is the voltage applied across the thin film stack, V_I is the voltage across the insulator and V_p is the voltage drop across the phosphor layer. The applied voltage is divided across the two layers capacitively, such that:

$$V_I = \frac{C_p}{C_I + C_p} V_a \tag{3-5}$$

$$V_{EL} = \frac{C_I}{C_I + C_p} V_a \tag{3-6}$$

Here, C_I is the insulator capacitance per unit area and C_p is the phosphor layer capacitance per unit area. This is simply the dielectric constant of the layer, ϵ, divided by its thickness, d. Equations 3-5 and 3-6 apply for all voltages below threshold.

Above threshold, charge begins to flow inside the phosphor layer. The voltage drop across the phosphor remains constant, so enough charge must flow such that the sum of the voltage across the phosphor and the insulator remains equal to the applied voltage.

Thus the maximum voltage drop across the phosphor layer is:

$$V_{p,\max} = V_{p,th} = \frac{C_I}{C_I + C_p} V_{th} \tag{3-7}$$

The maximum voltage drop across the insulator is:

$$V_{I,\max} = V_a - V_{p,\max} = V_a - \frac{C_I}{C_I + C_p} V_{th} \tag{3-8}$$

The amount of voltage transferred to the insulator versus the case where the phosphor is below threshold, ΔV is:

$$\Delta V = \frac{C_I}{C_I + C_p}(V_a - V_{th}) \tag{3-9}$$

The insulators continue to act as an ideal capacitor above threshold, therefore any increase in voltage across them results in an increase in charge transferred to them. This increased transferred charge on the insulators above threshold , ΔQ, is:

$$\Delta Q = (C_I + C_p)\Delta V \tag{3-10}$$

If a second pulse of the same polarity is applied no current will flow within the phosphor due to the built up space charge. If the device is driven by a bipolar waveform, the cycle merely repeats itself with each pulse, the charge flowing back and forth across the device, with light pulses being emitted at twice the drive frequency. For this case, the steady state transferred voltage and charge are:

$$\Delta V = 2\frac{C_I}{C_I + C_p}(V_a - V_{th}) \tag{3-11}$$

$$\Delta Q = 2C_I(V_a - V_{th}) \tag{3-12}$$

Charging and discharging the capacitors requires work, so the total input power density, P, is:

$$P = 4fC_I(V_a - V_{th})V_{p,th} \tag{3-13}$$

Equation 3-13 includes the pulse frequency, f, defined as the number of positive electrical pulses per unit time.

3.5 Device Efficiency

Numerous factors contribute to the overall efficiency of a TFEL device.

Factorization of the total efficiency allows specific mechanisms to be isolated and actions taken to optimize each particular component of the efficiency. This has been done for the simple model of EL devices (Mach and Mueller, 1984) leading to the following expression:

$$\eta_{tot} = \eta_{hot} * \eta_{exc} * \eta_{lum} * \eta_{out} \tag{3-14}$$

Here, η_{tot} is the total efficiency; η_{hot} is the fraction of electrons able to excite the luminescent centres; η_{exc} is the fraction of electrons with enough energy to excite a centre which actually do so; η_{lum} is the fraction of excited centers which relax radiatively and η_{out} is the fraction of the emitted photons which escape from the thin film stack.

In practice, it is very difficult to directly measure these terms. The outcoupling efficiency, $\eta_{out,}$ can be estimated if the optical properties of the various layers in the thin film stack are known. For the case of optically smooth films, this works out to be on the order of 10% for ZnS films (Mueller, 2000). The presence of a rough interface can increase the amount of light which escapes by up to 400% (Mach et al., 1988, 1990).

Suitable methods for determining values for the remaining terms in equation 3-14 continue to raise debate. Efforts to estimate η_{hot} depend on a determination of the interaction cross section, σ. The most recent calculations require a cross section two orders of magnitude larger than the geometric cross section of the luminescent centre, which seems highly unlikely (Ono, 1995).

The other two terms, η_{exc} and η_{lum} work against each other to a certain degree.

The excitation efficiency increases linearly with dopant concentration, however, the luminescent efficiency begins to drop above a certain optimum concentration due to cross center relaxation processes. Because the later concentration quenching effect decreases the luminescent efficiency more strongly than the linear increase in excitation efficiency, the overall efficiency decreases. It is therefore important to determine the optimum doping level for each phosphor material.

Measuring Efficiency

In practice, only the overall external efficiency of a TFEL device is measured. For displays, the efficiency is expressed as the luminance per unit of input power. The input power of an EL device is given by equation 3-13. The practical means of measuring the power utilizes a Sawyer-Tower circuit, shown in Figure 3-5. In this setup, the applied voltage is divided capacitively across the EL device, C_{EL}, and an external sense capacitor, C_s. By making C_s suitably large, virtually the entire voltage drops across the EL device. Because the capacitors are in series, the charge, Q, is the same on both.

By plotting the applied voltage on the x-channel of an oscilloscope and the voltage across the sense capacitor on the y-channel, a charge transfer vs. voltage loop is obtained. The charge transferred can be converted from a voltage, V_y, to units of charge by multiplying by the sense capacitance ($Q=V_y \bullet C_s$).

A plot of transferred charge vs. applied voltage is shown in Figure 3-6. At low applied voltage, the trace shows a shallow slope as the applied voltage is divided across

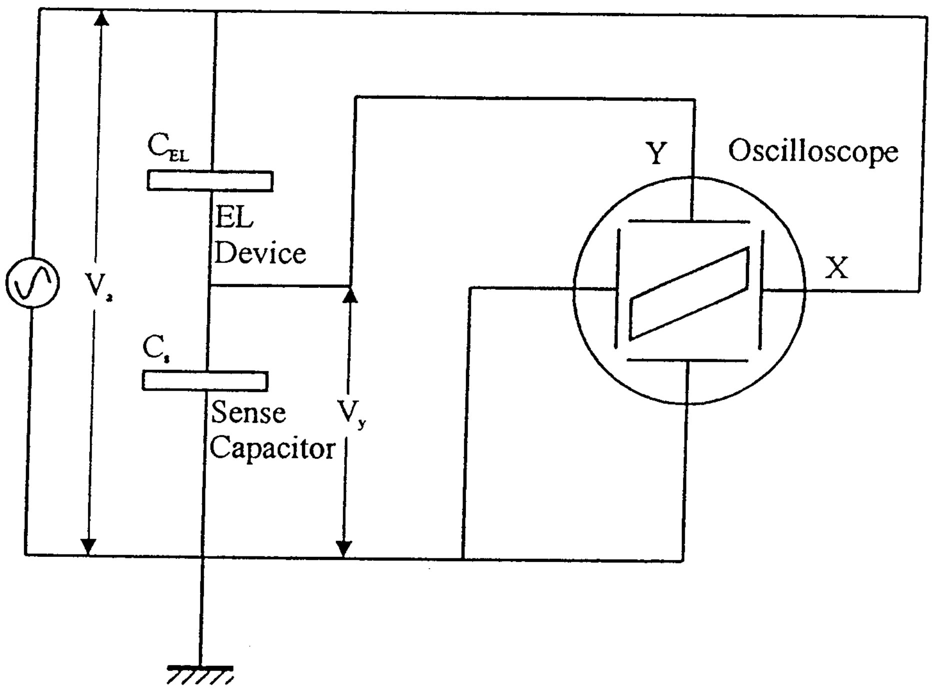

Figure 3-5) The Sawyer-Tower measurement circuit. The total voltage is applied to the x-channel of the oscilloscope, while the y-channel shows the voltage drop across the sense capacitor. C_{EL} is the total capacitance of the EL device, while C_s is the sense capacitance.

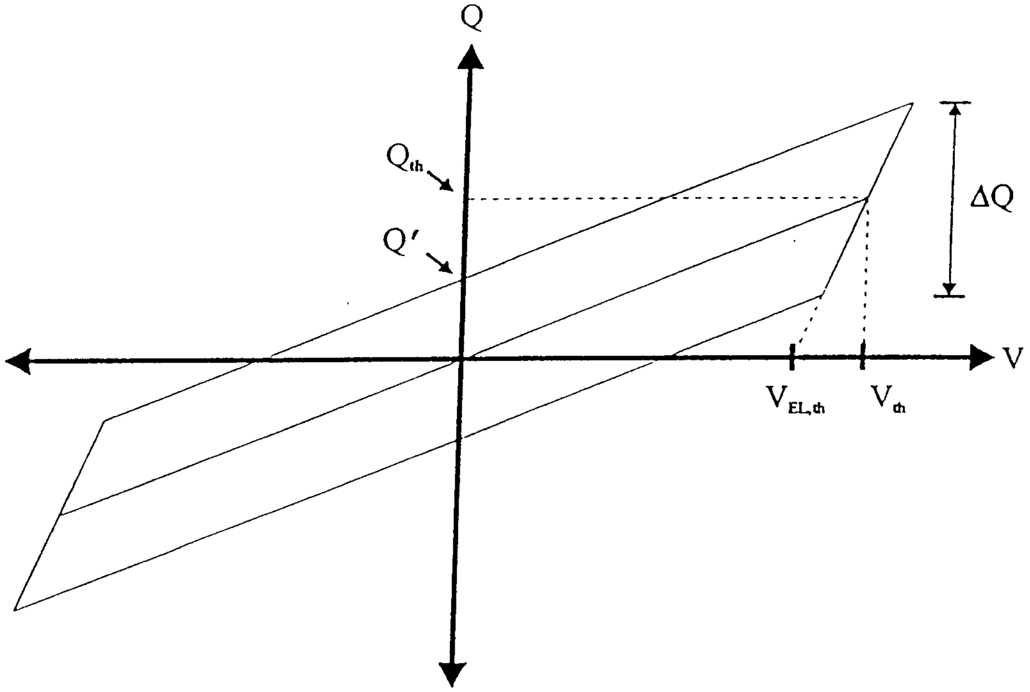

Figure 3-6) Charge density vs. voltage diagram. V_{th} is the threshold voltage of the EL device; $V_{EL,th}$ is the threshold voltage of the phosphor layer; Q_{th} is the threshold charge density; ΔQ is the transferred charge density; Q' is the residual charge in the device when V=0.

both the insulator and the phosphor layer. The slope of this line gives the capacitance of the EL stack. Above the threshold voltage, there is an abrupt change in capacitance as the phosphor layer breaks down. In this region, all the increase in voltage drops across the insulator, building up the excess transferred charge, ΔQ, given by equation 3-12. When the applied voltage is lowered, there is still a residual charge on the capacitors due to the space charge generated within the phosphor layer, which has a value of Q' at zero volts.

It can be shown that the area enclosed by the charge transfer-voltage loop is proportional to the power dissipated on each voltage cycle. In fact, equation 3-13 can be rewritten as:

$$P = f \times A \times C_s \tag{3-15}$$

Here, P is once again the input power, C_s is the value of the sense capacitance and A is the area of the charge-voltage hysteresis loop in V^2. This provides for a simple means of calculating the electric power dissipated by the EL device.

The light output of the device can be measured using a photometer or any of several other standard optical instruments. The brightness, B in cd/m^2, is measured perpendicular to the emissive surface. The ac efficiency of the device is then:

$$\eta = \frac{\pi \cdot B \cdot A}{P} \tag{3-16}$$

In equation 3-16 A is the area of the pixel in m^2. The brightness, B, is the photometric brightness which takes into account all of the visible light emitted by the TFEL device.

3.6 Materials for TFEL Displays

3.6.1 Substrates

By far the most common substrate for TFEL displays is glass. Low alkali glasses are used to prevent migration of ions from the substrate into the phosphor which may degrade the device performance. Several high temperature glasses exist which can be used as EL substrates. Which glass is selected is determined by the processing required for the films which are to be deposited on the substrate. The most commonly used glass is Corning 1737, which has a strain point of 666°C. The strain point is still well below the temperature at which viscous flow of the glass occurs, however above this temperature care must be taken in designing the annealing process to limit the effect of thermal expansion mismatch between the substrate and the films (Leskelä et al., 2000).

If temperatures well above the strain point of a glass substrate are required in order to process the phosphor, a ceramic substrate may be used instead. Because ceramic substrates are translucent, the inverted device structure shown in Figure 3-2 must be used. The substrate can be used merely as a support for subsequent layers in the device (Wu, 1996), or, if a suitably thin ceramic sheet is available it can serve as both the substrate and the bottom insulator (Nanto et al., 1988).

3.6.2 Electrodes

Selection of the metal electrode is generally quite straightforward. High conductivity, and ease of deposition and patterning dictate the choice of metal. By far the most common material used is aluminum. In addition to its excellent electrical properties, it also exhibits self-healing breakdown characteristics when used in combination with many common dielectric materials. In self-healing breakdown, any pin holes in the dielectric which act as breakdown pathways become electrically isolated due to the local melting of the aluminum electrode. This prevents the pixel from being destroyed by defects in the insulator layer. Deposition and patterning techniques for aluminum have been well developed by the semiconductor industry. In some more exotic display schemes which require high temperature processing after metallization, refractory metals must be used for the electrodes (King, 1996).

For the transparent electrode, doped oxide ceramics are used. The most common material is indium tin oxide (ITO). Indium oxide is electrically conductive when undoped due to oxygen deficiency. This conductivity is further enhanced by substituting roughly 10% of the indium with tin. Because of the higher valence of tin (4+) relative to indium (3+), tin doping results in the generation of donor states a few meV below the conduction band edge. These donor states become ionized at room temperature resulting in electronic conduction. Because the electron concentration is lower than in metals, the plasma frequency lies in the infra-red and the material is therefore transparent to visible light (Fan and Goodenough, 1977). The most commonly used alternative to ITO is ZnO, which, like ITO, is conductive due to oxygen vacancies. By doping ZnO with elements such as Al or Ga the conductivity is enhanced.

3.6.3 Insulators

The insulators play a key role in the operation of TFEL displays. They must be stable under the high electric fields used to drive the device (1-2 MV/cm) and therefore require a high electric breakdown strength. They must also be fabricated in such a fashion as to eliminate pinholes to prevent breakdown and charge leakage.

The necessary electrical characteristics of the insulators can be illustrated by examining once again the electrical characteristics of the TFEL device. According to Maxwell's equations, the displacement field, D, is continuous perpendicular to an interface, therefore:

$$D = \varepsilon_i E_i = \varepsilon_p E_p \tag{3-17}$$

Where ε_i is the dielectric constant of the insulator, E_i is the electric field in the insulator, ε_p is the dielectric constant of the phosphor and E_p is the electric field in the phosphor.

When a voltage is applied across the TFEL stack the voltage across the phosphor and insulator layers is proportional to both the electric field and the layer thicknesses:

$$V_p = \left[\frac{\varepsilon_I d_p}{\varepsilon_I d_p + \varepsilon_p d_I}\right] V_a \tag{3-18}$$

Equation 3-18 applies only when the phosphor field is below threshold. The phosphor voltage reaches it's maximum when the threshold field for breakdown is reached. This can be expressed as follows:

$$V_{th} = \left[1 + \frac{\varepsilon_p d_I}{\varepsilon_I d_p}\right] E_{p,th} d_p \tag{3-19}$$

where $E_{p,th}$ is the electric field in the phosphor at threshold, and is simply the voltage across the phosphor divided by the layer thickness. What equation 3-19 shows us is that thin, high permittivity materials would result in the lowest operating voltages. Thickness of the insulator layer is limited by the breakdown field strength of the material.

The product of the breakdown field strength and the permittivity is used as a Figure of merit for TFEL insulators. A selection of dielectrics which have been used in TFEL devices is shown in Table 3-1. Also shown in the table is the breakdown mode of the insulator, with SH being self-healing breakdown and P propagating breakdown. When a material which exhibits self-healing properties undergoes a localized breakdown, the heat generated causes the metal electrode to melt. Because of the high surface energy, the liquid electrode balls up, isolating the short circuit and ending the

Material	ϵ_r	E_{BD}(MV/cm)	$\epsilon_o\epsilon_r E_{BD}$ (μC/cm^2)	Breakdown Mode
SiO_2	4-5	6-11	2-5	SH
Si_3N_4	8	6-8	4-6	SH
SiO_xN_y	6-7	7-8	4-4.5	SH
SiAlON	8	8-9	5-6	SH
Al_2O_3	8-9	5-8	3.5-6	SH
Al_2O_3/TaO_2	10-20	4-6.6	2-6	SH
Al_2O_3/TiO_2	9-18	5-6.7	5.5-10	SH
Y_2O_3	12	3-5	3-5	SH
a-$BaTiO_3$	14-20	3	3-5	SH
$BaTaO_5$	22-23	3.5-5	7-10	SH
Ta_2O_5	23-25	1.5-3	3-7	SH/P
$Sr(Zr,Ti)O_3$	100	3	26	P
$SrTiO_3$	140	1.5-2	19-25	P
$PbTiO_3$	150-190	0.5	7-9	P

Table 3-1) Dielectric properties of potential TFEL insulator materials.
SH = Self-healing
P = Propagating
(After Leskelä et al., 2000).

breakdown. In the propagating case, the metal does not ball up, and heat continues to build up, spreading the breakdown across the entire pixel catastrophically.

Unfortunately, the materials with the highest Figure of merit also exhibit propagating breakdown. This can be overcome by using thicker dielectric layers, which can support a larger voltage before breakdown (Wu, 1996). While this does allow the use of these dielectrics, it does result in an increased threshold voltage, as shown by equation 3-19.

3.6.4 Phosphors

The phosphor layer must meet several criteria in order to be used in TFEL devices. These include i) the bandgap must be large enough to emit visible light; ii) the material must be capable of being doped with suitable luminescent centres; iii) the material must be able to support large electric fields (10^6 V/cm) and still behave as an insulator below threshold; iv) the material must be compatible with thin film deposition technology and any necessary post-deposition processing. This has led to only a limited number of phosphors being useful for TFEL applications.

3.6.4.1 Sulphides

The earliest, and only commercially used thin film electroluminescent phosphor is ZnS:Mn. This material emits in a broad yellow band centred at 580 nm. The brightness at 40 V above threshold is approximately 300 cd/m^2 with an efficiency of 5 lm/W. This high brightness and efficiency has been exploited in monochrome display panels. In order to expand the information content of EL displays, red and green filters can be applied to the ZnS:Mn emission in order to make a multicolour display. The use of filters however significantly reduces the total brightness and efficiency of the device.

A bright green phosphor can be made by doping ZnS with Tb. In order to improve the brightness and efficiency, the material is codoped with oxygen and fluorine (ZnS:TbOF). The fluorine compensates the excess positive charge of the terbium, while the oxygen isoelectronically substitutes for sulphur in the lattice, and due to its smaller size, reduces the strain required to substitute the large terbium ion for zinc. This results in a phosphor with a brightness greater than 100 cd/m^2 and an efficiency of 1.7 lm/W (Yoshino et al., 1992).

Obtaining an efficient blue phosphor using sulphides has proven elusive. Early hopes were placed on SrS:Ce which peaks at 480 nm and has a shoulder at 535 nm, resulting in a blue-green emission. In order to obtain suitable colour purity, filters must be employed which block 70-80% of the emitted light, significantly reducing device performance (Rack and Holloway, 1998). In order to avoid the use of colour filters, SrS:Cu and SrS:Cu,Ag have been explored. These emit at peak wavelengths below 470 nm, depending on the amount of Ag introduced in the films (Sun, 1998). Most recently, the phosphor $BaAl_2S_4:Eu^{2+}$ has been investigated. In general, Eu^{2+} is not stable in the high electric fields used in TFEL, becoming ionized to Eu^{3+} in the large field. In this host however Eu^{2+} is stable, and emits in a single band peaking at 466 nm (Kawanishi et al., 1999). Unfortunately, chemical stability of the host has proven a problem. While these materials show great promise, more work is required before they can be commercialized.

3.6.4.2 Oxides

In the past ten years oxide phosphors have shown promise for use in EL displays. They combine high chemical stabilities with a broad range of structures and compositions which can be used to span the entire colour gamut. On the down side, the generally wide band gaps result in the need for large electric fields in order to excite the phosphors. Many also exhibit poor efficiency, however in the case of several phosphors, optimization of the deposition conditions and post-deposition processing has resulted in dramatic improvements in device performance. The films also require high post-deposition annealing temperatures (>800°C), which limits the range of substrates that can be used.

The first oxide phosphor which showed promise for TFEL devices was Zn_2SiO_4:Mn, which was a well known photoluminescent phosphor (Minami et al., 1990). The phosphor shows a bright green luminescence peaking at 528 nm and has an efficiency 0.78 lm/W. Performance of this phosphor can be improved by the substitution of germanium for silicon. The peak wavelength is slightly red shifted, moving from 528 nm to 535 nm while maintaining equivalent EL performance. The chief advantage is that this performance can be obtained using a post-deposition annealing temperature of 700°C, as opposed to the 1000°C required for Zn_2SiO_4 (Xiao et al., 1997a). This has subsequently been utilized to create oxide TFEL devices on Corning 1737 glass (Kitai et al., 1999). Zinc silicate devices can also be made on glass, however in order to crystallize the films the post deposition anneal was conducted at a pressure of 12 atm. (Park et al., 2002). Powder phosphor are typically processed with alkali- or alkaline earth halides fluxes in order to lower the firing temperature (Narita, 1999). While incorporation of fluxes in thin films has lead to improved short term performance, the mobility of the fluxing agents in the high electric fields resulted in a rapid degradation of the devices (Bender et al., 2002).

Rare earth activated gallium sesquioxide and alkaline earth gallates have also proven themselves to be useful phosphors for EL applications and provide the possibility of covering the entire visible spectrum. Efficient red EL has been obtained from Ga_2O_3:Eu (Kitai et al., 1997). This phosphor has the advantage of being bright in its as deposited form. Bright green emission has also been reported for $Ga_2O_3:Mn^{2+}$ (Minami et al., 1997a). In the case of alkaline earth gallates, the $M^{2+}Ga_2O_4$ phase (M=Ca, Sr) has proven the most useful of the many possibilities. In the case of $CaGa_2O_4$, Eu^{2+} emits a bright red line at 615 nm (Xiao et al, 1997b). Using Tm^{3+} and Dy^{3+}, a blue emission is obtained, however it requires filters to eliminate undesirable emission lines which shift the colour coordinates. A more complete list of oxide phosphors is shown in Table 3-2.

Phosphor	L_{max} @1 kHz (60 Hz) (cd/m^2)	η (lm/W)	Colour
Zn_2SiO_4:Mn	3020 (230)	0.78	Green
Zn_2GeO_4:Mn	341 (39)	0.08	G
$CaGa_2O_4$:Mn	2790 (592)	0.25	Yellow
$ZnGa_2O_4$:Mn	758 (235)	1.2	G
$ZnAl_2O_4$:Mn	21	0.01	G
$ZnGa_2O_4$:Cr	196 (9)	0.02	Red
Ga_2O_3:Mn	1018 (227)	1.7	G
Ga_2O_3:Cr	375 (34)	0.04	R
$CaGa_2O_4$:Eu	215 (19)	0.03	R
$ZnGa_2O_4$:Eu	62	0.14	R
Y_2O_3:Eu	144	0.01	R
Ga_2O_3:Eu	153	0.38	R
$CaGa_2O_4$:Dy	30	0.02	Y
Y_2SiO_4:Ce	13	0.05	Blue

Table 3-2) Oxide phosphors investigated for TFEL applications (after Leskelä et al., 2000).

Chapter 4

The $Cd_xZn_{1-x}Ga_2O_4$ Phosphor System

4.1 Introduction

The spinel structure originally applied to the compound $MgAl_2O_4$. Subsequently, hundreds of chalcogenides and fluorides have been discovered which have identical or related structures to the original spinel. Furthermore, spinels are important building blocks in more complicated structures. This tremendous variability in structure and composition make spinels excellent hosts for phosphors. It opens up the possibility of using a wide range of dopant atoms and host manipulations in order to optimize the properties of the phosphor.

One spinel compound in particular, $ZnGa_2O_4$, has long been known as an efficient phosphor when activated with a range of dopant ions (Leverenz, 1950). More recently, this phosphor has been investigated for use in thin film electroluminescent applications

(Minami et al., 1995). Because of its tremendous potential, this phosphor makes an excellent candidate for further exploration.

4.2 The Spinel Structure

Spinels are a class of compounds with the basic chemical formula AB_2X_4, where A and B are cations and X is one of several possible anions (ie. O,S,Se,Te,F). Within the family of spinels, A and B can be any of a wide range of possible elements, as long as the charge balance is maintained. In the case of $ZnGa_2O_4$ we are dealing with what is referred to as a 2-3 spinel. In this case the A ion (Zn) has a formal charge of +2, while the B ion (Ga) has a formal charge of +3. Other possible spinels are the 4-2 and 6-1, which will only be mentioned briefly in this discussion.

The basic structure of the spinel is shown in figure 4-1. The unit cell contains eight formula units, and is defined by a face centred cubic array of oxygen ions. Such an arrangement produces a total of 96 interstitial lattice sites. Of these, 64 are tetrahedrally coordinated and 32 are octahedrally coordinated. In the case of $ZnGa_2O_4$, the Zn^{2+} ions sit in tetrahedral sites, while the Ga^{3+} ions are located in the octahedral sites. The size of the interstitial holes is determined by the size of the ions they contain, which tend to dilate the oxygen sublattice, which would ideally be cubic close packed.

The relative position of the anions in spinel systems are exactly specified by a parameter labelled u. Variations in this parametre reflect the adjustment of the spinel

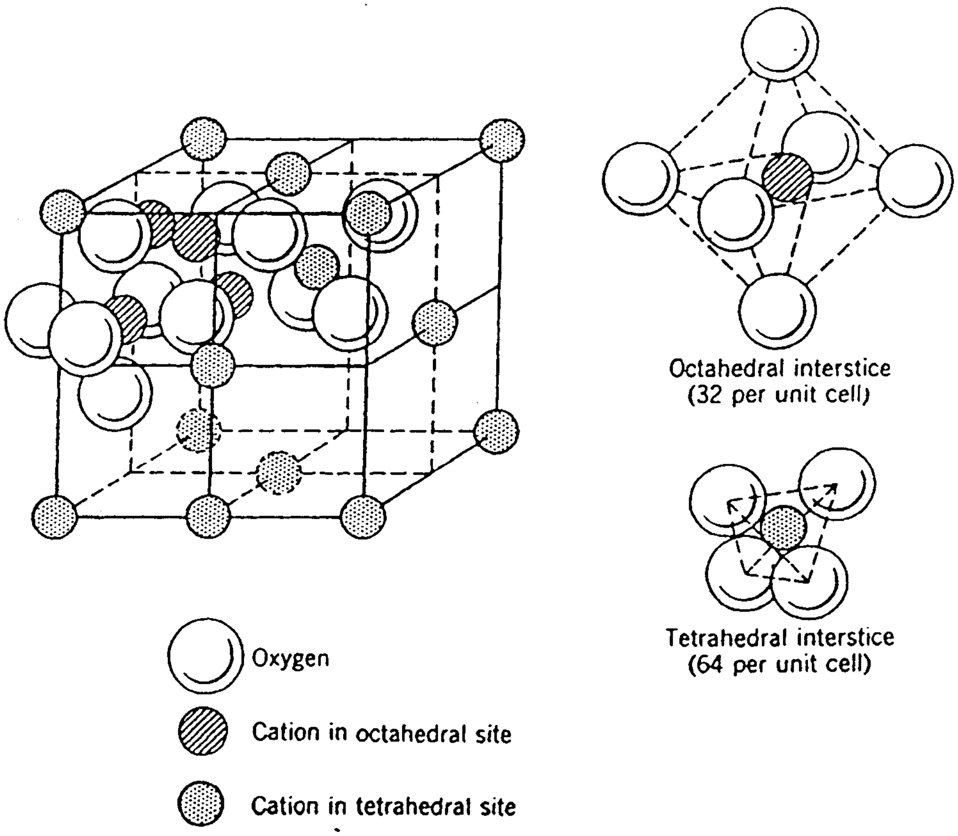

Figure 4-1) The spinel structure (After von Hippel, 1954).

structure to accommodate different cations and cation distributions. This term has a value of 0.375 for the ideal face centred close packed arrangement, and increases as the lattice expands. As the lattice expands, the tetrahedral holes expand uniformly and maintain their symmetry, while the octahedral holes contract and their symmetry is lowered. Although it is possible to have u values of less than 0.375, a survey 135 spinels for which the u parameter is known reported only 6 with u values lower than 0.375 (Hill et al., 1979).

Of importance in understanding the behaviour of spinels is the coordination of the various polyhedra. The tetrahedral sites are all isolated from one another and have no contact, but share corners with the octahedral sites. The octahedral sites are edge-sharing and form chains along the $\langle 110 \rangle$ direction. Because the octahedral sites are edge sharing, the distance between neighbouring Ga^{3+} ions is quite small.

The arrangement of ions exhibited by $MgAl_2O_4$ is referred to as the normal spinel structure. Another possible arrangement is the inverse spinel in which all of the A ions switch places with half of the B ions. Thus, the A ions are now octahedrally coordinated while the B ions are evenly distributed between the tetrahedral and octahedral sites. An example of a spinel with the inverse structure is $Fe[NiFe]O_4$ (Blasse, 1964). A vast number of compounds lie somewhere between these two extremes. The degree of inversion, γ, is the fraction of A cations which are situated in octahedral sites. It has a value of $\gamma=0$ for normal spinels, $\gamma=1$ for inverse spinels and $\gamma=\frac{2}{3}$ for a completely random distribution. The compound $MnFe_2O_4$ is an example of a partially inverse compound and has an inversion parameter of $\gamma \approx 0.29$ (Wyckoff, 1965). Partial inversion can be induced in the normal spinel $MgAl_2O_4$ by nonstoichiometry. If Al is substituted for Mg in a 2:3 ratio, the excess aluminum substitutes for magnesium on the tetrahedral sublattice. This gives the material the composition $Mg_{1-3x}Al_{2+2x}O_4$ and results in the formation of x vacancies on the tetrahedral sublattice (West, 1988). There is a high solubility for excess Al_2O_3 at high temperatures. At 1400°C the $MgO:Al_2O_3$ ratio can be as high as 2:3, as opposed to the 1:1 ratio in the stoichiometric material (Roy et al., 1953).

The degree of inversion is determined by i) temperature, ii) the electrostatic contribution to lattice energy, iii) cationic radii, iv) cationic charge and v) crystal-field effects. The interactions between these various effects is quite complicated and beyond the scope of this work. Several excellent reviews of the spinel structure provide a more complete explanation of the factors affecting cation distribution (Blasse, 1964; Sickafus and Wills, 1999)

One important thing to note is that the degree of inversion does not obey Vegard's law. Between the endpoints, the inversion parameter can display complex behaviour which is not easily explained (Arean and Diaz, 1982; Porta et al., 1974; Porta and Anichini, 1980).

4.3 The Structure of $ZnGa_2O_4$, $CdGa_2O_4$ and $Cd_xZn_{1-x}Ga_2O_4$

The structure of $ZnGa_2O_4$ has long been known to be cubic spinel (Buschendorf, 1931). The structural determination was incomplete however, since the cation distribution could not be determined. Because Zn^{2+} and Ga^{3+} have virtually identical electronic structures, their x-ray scattering powers are too close for them to be differentiated using conventional x-ray techniques. Using anomalous dispersion, the material was determined to be a normal spinel, within the limits of the technique (Goffin et al., 1961). Subsequent x-ray structural refinements were performed in order to model the properties of impurity centres in $ZnGa_2O_4$ assumed a perfectly normal spinel (Hornstra and Keulen, 1972).

There is limited evidence to suggest that there is some small degree of inversion in $ZnGa_2O_4$. Electron paramagnetic resonance (EPR) measurements of Mn^{2+} and Fe^{3+} show some disordering in the material (Krebs et al., 1979). This has been supported by more recent Mössbauer spectroscopy (Schiessl et al., 1994). In both cases, no attempt has been quantify the degree of inversion. More accurate measurements have been made in order to determine the u parameter without making any assumptions regarding the cation distribution (Wendschuh-Josties et al., 1995). The authors found a measurable shift in the u parameter with the equilibration temperature of the sample. This strongly implies thermally induced disordering of the cations. It is the author's intent to integrate this x-ray study with new anomalous dispersion measurements, however this work has

Compound	Lattice Parameter (Å)	u Parameter	Degree of Inversion, β	Tetrahedral Site Size (Å)	Octahedral Site Size (Å)
$ZnGa_2O_4$	8.3300	0.387	0.000	0.600	0.620
$CdGa_2O_4$	8.5700		0.25	0.703	0.661

Table 4-1) The structural properties of $ZnGa_2O_4$ and $CdGa_2O_4$ (after Hill et al., 1979).

yet to be published.

The structure of $CdGa_2O_4$ is also a spinel (Rudorff and Reuter, 1947). Although the initial study did not quantify the degree of inversion, the authors did conclude that there was some disorder. The inversion parameter was later determined to be ~25% (Huber, 1959; Huber and Bénard, 1965). Although this value for the inversion is generally accepted, there has also been an argument put forward that the observed shift in x-ray intensity is actually the result of excess Ga_2O_3 dissolved in the spinel lattice, due to the evaporation of CdO (Datta and Roy, 1968). Because the vapour pressure of CdO reaches $1x10^{-4}$ torr at just 530°C, cadmium oxide sublimation during compound formation does impact the stoichiometry of the final material Table 4-1 compares the observed structural data for $ZnGa_2O_4$ and $CdGa_2O_4$.

The structure of the solid solution of $ZnGa_2O_4$ and $CdGa_2O_4$ has only been studied once (Irgaslev and Sirazhiddinov, 1975). The authors reported a strong composition dependant variation in the inversion parameter. At $X_{Cd}<0.4$, the Cd was reported to substitute for Zn in tetrahedral sites. For X_{Cd} in the range of 0.4-0.6, the spinel was disordered. The amount of disorder decreased as the Cd content was increased further. No absolute values were provided for the inversion parameter of the solid solution.

4.4 Luminescence in the $Cd_xZn_{1-x}Ga_2O_4$ Powder System

Luminescence was first reported in $ZnGa_2O_4$ when doped with Mn^{2+} several decades ago, but did not attract a great deal of attention (Leverenz, 1950). The next major study of $ZnGa_2O_4$:Mn was conducted as part of a broader investigation of Mn^{2+} activated gallate phosphors (Hoffman and Brown, 1968). The phosphor showed green luminescence, peaking at 513.5 nm under both PL (254 nm excitation) and CL excitation. No attempt was made to optimize the activator concentration. The same paper reported no PL or CL from $CdGa_2O_4$:Mn.

In recent years, there has been a resurgence of interest in $ZnGa_2O_4$ in both its doped and undoped forms. This interest has been driven by the development of new display technologies. Most of the work has revolved around the use of this phosphor for field emission displays and vacuum fluorescent displays, which use cathode ray excitation. The traditional sulphide phosphors used in CRTs are not suitable for these applications, since gasses evolved in electron bombardment damage the cathodes (Itoh et al., 1989).

The undoped phosphor emits a broad blueish-white spectrum centred at ~470 nm. This emission has colour coordinates of x=0.170 and y=0.130, and a luminous efficiency of 0.7 lm/W when used in vacuum fluorescent displays (Itoh et al., 1991). While this phosphor exhibited excellent long term stability, the poor colour saturation makes it unsuitable for full colour display applications.

More interest has been shown in $ZnGa_2O_4$:Mn since the emission is relatively narrow and bright. A CL brightness of over 350 ft-L was obtained using uncoated, unoptimized phosphors (Vecht et al., 1994). The brightness of $ZnGa_2O_4$:Mn powder under CL excitation can be dramatically improved by coating the phosphors with a conductor, such as In_2O_3 (Kim et al., 2000). The authors reported a brightness increase of over 4x as a result of the elimination of charge build up withing the phosphor layer. It was shown that the efficiency is dependent on forming only islands of In_2O_3 on the surface of the phosphors rather than a continuous coating.

While cathodoluminescent studies may reveal whether the phosphor is suitable for CL displays, photoluminescent studies are more useful for understanding the fundamental processes occurring within the phosphor. Both excitation and absorption data provides information about dopant incorporation and the site of excitation energy absorption.

Early photoluminescent investigations of $ZnGa_2O_4$ reported a manganese emission at 513.5 nm (Hoffman and Brown, 1968). More recent studies all place the emission at approximately 505 nm, although there is some processing induced variability (Poort et al., 1997). Because the luminescence is both spin and parity forbidden, it has a decay time of approximately 4 ms (Tran et al., 1995). The decay time is dependent on the manganese content, extending to over 8 ms at low manganese contents (Endo et al., 1996). This was attributed to the formation of Mn^{2+}-Mn^{2+} pairs. The authors found the optimum doping level to be 0.4% of the Zn sites. This compares favourably with the value of 0.5% and a decay time of 4 ms, reported in an earlier study, (Tran et al., 1995). Still another examination of $ZnGa_2O_4$:Mn reported a maximum PL intensity with Mn substituted for 0.6% of the Zn (Shea et al., 1994). The excellent correspondence between these measurements instills a great deal of confidence in their accuracy. Undoped, the material exhibits a self-activated luminescence peaking between 430 nm and 450 nm, depending on the exact stoichiometry of the material (Yu and Lin, 1996a). This luminescence has a decay time on the order of microseconds.

Studies of the luminescence excitation of $ZnGa_2O_4$ show an excitation maximum at 435 nm in the undoped material (Shea et al., 1994). With the addition of manganese substituting for zinc, the 505 nm emission band appears at the expense of the 450 nm self-activated luminescence. The self-activated centre does not appear to sensitize the manganese luminescence, but rather that the transmission of excitation energy to manganese is a more efficient process (Jia et al., 1995). The maximum in the excitation spectrum remains at 435 nm when manganese is present, however, a lower energy shoulder forms which corresponds to the direct excitation of the manganese ion.

The work on $Cd_xZn_{1-x}Ga_2O_4$ is much more limited. Cathodoluminescent studies of the undoped compound found that the self-activated luminescence red shifted and decreased in intensity, while a new peak near 500 nm appeared (Choi et al., 1998). This has also been observed using photoluminescent excitation (Endo et al., 1996). In this case however, only a single emission peak was observed. Below $x=0.2$ cadmium, there was virtually no shift in the emission. At $x=0.2$, the emission abruptly jumped from 435 nm to 500 nm. The emission is gradually red shifted with increased cadmium content above $x=0.2$.

When doped with manganese, $Cd_xZn_{1-x}Ga_2O_4$ emits a single green peak, which red shifts only slightly with increased cadmium content up to x=0.4 (Kim et al., 1999). It should be noted that this shift is of the same order as the variation in manganese luminescence in $ZnGa_2O_4$ which is induced by variations in stoichiometry. Since the powders in this study were fired at 1200°C followed by a reduction firing in 5% H_2 this could have introduced a degree of nonstoichiometry, which increased with x, due to the volatility of CdO. Because the stoichiometry was not determined, it is impossible to state whether or not Cd or Zn loss during processing impacted the properties of the materials.

4.5 Luminescence of Thin Film $ZnGa_2O_4$

The vast majority of the work done on thin film $ZnGa_2O_4$ has used RF sputtered films. Loss of zinc during sputtering has been reported, and attributed to the high vapour pressure of zinc relative to gallium (Hsieh et al., 1994a; Kim et al., 1998). Stoichiometric films can be obtained by using a suitably low substrate temperature, although there is significant variation in the maximum possible temperature at which stoichiometry can be obtained. Generally, the substrate temperature has been limited to below 450°C. Stoichiometry of films deposited by pulsed laser deposition were obtained by using excess ZnO in the target and high oxygen partial pressures during deposition (Lee et al., 2000). This allowed for substrate temperature in excess of 700°C. When films were deposited by CVD, the composition could be controlled by holding the temperature of the zinc source constant and adjusting the temperature of the gallium source (Minami et al., 1996).

Generally speaking, films tend to be poorly crystallized when deposited at low substrate temperatures. The films deposited at temperatures below ~450°C tend to be dominated by the 222 or 400 peaks (Hsieh et al., 1994b; Kim et al., 1998; Lee et al., 2000). This does not appear to have much substrate dependence (i.e. Si vs quartz vs ITO coated glass) except in the case of the pulse laser deposited films which were deposited on (100) MgO, and showed a sharp 400 line even at extremely high (>600°C) substrate temperatures. Sputtered films deposited at temperatures above 450°C or films which have been annealed show a rotation of the texture towards the random powder orientation, which is dominated by the 311 peak.

In the case of undoped $ZnGa_2O_4$ films deposited with no heating, no luminescence is observed under CL excitation (Hsieh et al., 1994a). With substrate heating or post deposition annealing, the films show a blue CL emission centred at ~450-480 nm. This is slightly shifted relative to the 435 nm emission reported for powders (Lee at al., 2000). The changes in emission properties of the films appears to be related to the nonstoichiometry. Shifts in the self-activated luminescence of powders with varying Zn:Ga ratios has been reported (Jeong et al., 1998).

When activated with manganese, the host lattice emission of the films is quenched and only the manganese emission centred at 505 nm is observed. Both the excitation and emission spectra are broadened in the film relative to the powder (Yu and

Lin, 1996b). This has been attributed to the zinc deficiency in the films, which resulted in inhomogeneous broadening. Films annealed on glass were not as bright as films annealed on silicon, which the authors claimed was a result of the difference in heat transfer characteristics of the two substrate materials (Kim et al., 1998).

Thin film electroluminescence of manganese doped films has also been examined. The films were sputtered, and were reported to have the same stoichiometry as the targets (Minami et al., 1995). Optimum EL performance was obtained from targets with 1:1 $ZnO:Ga_2O_3$ ratios, however the peak luminance was independent of composition for a zinc deficiency of up to 10 atomic%. The best devices had a luminance of 710 cd/m^2 and an efficiency of 1 lm/W at 1 kHz. These films required a post deposition annealing step at 1020°C. When comparing CVD films to sputtered films, it was found that the CVD films had superior performance as deposited, however upon annealing above 1000°C the two sets of devices showed no significant difference (Minami et al., 1996).

Other dopants have been examined in TFEL $ZnGa_2O_4$ devices in order to span the visible spectrum (Minami et al., 1997b). While luminescence was obtained with Cr (red), Ce (blue) and Eu (red), none of these dopants were as bright or efficient as manganese. Further study is required in order to evaluate the potential of these activators in practical display applications.

Chapter 5

Experimental Technique

5.1 Phosphor Preparation

5.1.1 Powder Samples

Samples for photoluminescence measurements were fabricated by hand grinding ZnO (99.999%, Alfa Aesar), CdO (99.995%, Alfa Aesar), Ga_2O_3 (99.9999%, Eagle-Pritcher) and $MnCO_3$ (99.99%, Alfa Aesar). The manganese was substituted for 2% of the Group II elements. The cadmium was substituted for zinc in 5% intervals ranging from 0% cadmium up to 25% cadmium. Samples containing 50% cadmium were also produced. The total weight of the powders was 5 g. Pellets were pressed to 10 tonnes in a 1¼″ stainless steel die set. The pellets were fired in a vacuum furnace at 1000°C for

12 hours at pressures of less than 5×10^{-6} torr.

After firing, the pellets were ground into a powder using an alumina mortar and pestle. A mixture of 120-150 mg of powder in 5 ml of ethanol was then made, and shaken in order to form a suspension. The powders were then allowed to settle on a 1 cm x 1 cm square of borosilicate glass, and the ethanol evaporated. The resultant layer of phosphor powder was stable enough to be handled easily.

5.1.2 Sputter Target Preparation

Targets were fabricated by reacting a mixture of ZnO (99.999%, Alfa Aesar), CdO (99.995%, Alfa Aesar), Ga_2O_3 (99.9999%, Eagle-Pritcher) and $MnCO_3$ (99.99%, Alfa Aesar). The manganese was substituted for 2% of the Group II elements. Target compositions were the same as the compositions used in the photoluminescence component of this study. These materials were mixed in a mortar and pestle, and then loaded into alumina combustion boats. The targets were fired for 12 hours at 1000°C to form the spinel phase. Targets were formed by cold pressing 12-15 grams of the reacted powders to 10 tonnes in a 2″ steel die set.

5.2 Thin Film Deposition and Processing

5.2.1 Sputtering

The films were deposited by RF magnetron sputtering using a 2″ US Gun II. The substrates were 1 cm^2 pieces of $BaTiO_3$ and p-type silicon (the native oxide was not removed). The $BaTiO_3$ substrates were polished prior to film deposition in order to improve the surface finish. The substrates were rotated during sputtering in order to improve the film thickness uniformity. Because of the rotation, the substrate holder had to heated radiatively by a resistance heater. Typical sputtering conditions are shown in Table 5-1.

The film thickness was measured using a Tencor Alpha Step stylus profilometer.

Base Pressure	<5x10^{-6} torr
Sputtering Gasses Ar O_2	 10 mtorr 3 mtorr
Substrate Temperature	300°C
Source-Substrate Distance	5 cm
RF Power	100 W

Table 5-1) Sputter deposition process parameters.

5.2.2 Post-Deposition Processing

5.2.2.1 Annealing of Thin Films

Films for photoluminescence measurements were annealed in a vacuum furnace at temperatures ranging from 500°C to 900°C. The pressure during the anneal was maintained at $1\mathrm{x}10^{-6}$ torr. The furnace was brought up to the soak temperature over a two hour ramp, and was shut off after a 3 hour soak and allowed to cool.

Films for EL measurements were annealed in a separate vacuum tube furnace. The quartz tube was evacuated to better than $7.5\mathrm{x}10^{-6}$ torr by a diffusion pump prior to initiating the anneal. The pressure in the furnace further decreased to $3\text{-}4\mathrm{x}10^{-6}$ torr during the firing. The substrates were place in an alumina boat. The films were annealed at 900°C for times ranging from 1 hour to 48 hours to evaluate the effect of anneal time on the EL properties. Films were also annealed for 12 hours at temperatures ranging from 750°C to 950°C. Both of these sets of anneals were performed on all compositions. The temperature was ramped at 150°C/hour during heating, while the cooling rate was determined by the furnace insulation and averaged roughly half the heating rate. This applies to all films but those annealed for less than 6 hours. Films annealed for 1 or 3 hours were slid into and out of the preheated furnace using a quartz boat, and therefore the heating and cooling rates were much more rapid.

5.2.2.2 Electrode Deposition

The top indium tin oxide (ITO) electrode was deposited by reactive evaporation of indium:tin 90:10 alloy from a resistively heated quartz crucible. The substrates were mounted 18″ above the source and were heated to 300°C. The chamber was pumped down to below 7.5×10^{-6} torr and then back filled with UHP oxygen to a pressure of 4×10^{-4} torr during the deposition. The films were deposited at a rate of 2.5 Å/s to a total thickness of 1000Å. Deposition rate and thickness were monitored using an Inficon XTM/2.

The back electrode was silver and was deposited by electron beam evaporation. The chamber was evacuated to below 7.5×10^{-6} torr during the deposition. The films was deposited at a rate of 4-6Å/s to a total thickness of 5000Å. The thickness and deposition rate were monitored using an Inficon XTC.

5.3 Structure and Morphology

5.3.1 X-Ray Diffraction

The structure of both the films and the powders was determined by comparing observed x-ray diffraction pattern to those in the Joint Committee on Powder Diffraction database. The diffraction patterns were collected with a Nicolet diffractometer using copper K_α radiation at a scan rate of 0.5°•min^{-1}.

5.3.2 Scanning Electron Microscopy

The surface morphology of the films and substrates was observed using a Philips SEM 515. All images were collected using the secondary electron detector, with a 20 kV acceleration voltage. Energy dispersive x-ray spectra were collected using a Si:Li detector and analysis software URSA v. 1.27 developed by MekTech Inc.

5.3.3 Atomic Force Microscopy

AFM images were collected using a Digital Instruments Nanoscope IIIa operated in tapping mode. All images are 1 μm x 1μm. The grain size analysis and surface roughness was analysed using Scanning Probe Image Processor v. 2.104 by Image Metrology ApS. In order to obtain good contrast for grain size analysis the images were first filtered using a 15x15 local mean filter. In images which were located near pits, the images were first cropped in order to eliminate the pit.

5.4 Film Composition

The composition of the various films was determined using energy dispersive spectroscopy in a Maxim 2040SLI/Env scanning electron microscope, manufactured by Cam Scan. The x-ray intensities were corrected for atomic number, absorption and fluorescence (ZAF) and the atomic ratios calculated using proprietary software supplied by the manufacturer.

The films which were annealed for photoluminescence measurements were characterized by EDX in the Philips SEM 515. The as deposited films analyzed in the Maxim SEM were used as the composition standard, in order to compare relative amounts of cadmium, zinc and gallium. Qualitative EDX was also collected on numerous films used for EL measurements.

5.5 Photoluminescence Measurements

The powder samples were excited by 365 nm and 254 nm radiation from a handheld mercury lamp. A UV bandpass filter (Schott, UG 5) was used to eliminate undesirable lines from the lamp. The relative intensity of the emissions was measured with a Minolta LS-100 luminance metre. The emission spectrum was collected with an Ocean Optics S2000 fibre optic spectrometer. The excitation spectra of the powders were measured using a Perkin-Elmer LS-5 Spectrophotometer. The emission intensity was monitored at 504 nm and a filter was used in order to prevent the excitation wavelength from being detected (Schott, GG400).

Relative PL performance of the thin films was measured using the same Minolta luminance meter. The emission was excited using the 254 nm radiation from the mercury discharge lamp.

5.6 Electroluminescent Performance

The TFEL devices were driven by a trapezoidal waveform with a 270 μs pulse width. Brightness was measured with a Minolta LS-100 luminance meter. Finally, the transferred charge was measured with a Sawyer-Tower circuit, using a 235 nF capacitor. These measurements were performed at both 60 Hz and 600 Hz. In approximately half of the cases, only a single device was tested for a given set of processing parameters (i.e. anneal time and temperature, level of cadmium processing), however a large number of devices were repeated a second time using devices from a different deposition. The EL results reported for repeated samples are simply the linear average of the measured values. The uncertainty was calculated by adding in quadrature the uncertainties of the individual devices. The EL spectra were measured with the same Ocean Optics spectrometer that was used for PL measurements. The decay time of the phosphor was measured with a Thor Labs DET 110 PIN diode photodetector, which has a 20 ns rise time. Decay times reported are simply the time for the phosphor to decay to 1/e of the peak brightness. For these measurements the phosphor was pulsed by a 12 Hz drive signal from a Philips PM5715 pulse generator.

Chapter 6

Results and Discussion

6.1 Cadmium Processed $Zn_{1-x}Ga_2O_{4-x}$:Mn Powders

The unreacted powders were pressed to form pellets which were then vacuum fired in order to react the compounds to form the spinel, as well as to activate the manganese. After firing, the pellets were crushed in order to analyze their structure and luminescent characteristics. The ratios of the various components in the $ZnGa_2O_4$ and cadmium processed powders which were mixed to form the pellets is shown in Table 6-1. It should be stressed that these ratios apply only to the pellets before firing, since the loss of certain components, particularly CdO and to a lesser extent ZnO, occurs during firing. The loss of these two components sets an upper limit on the Zn:Ga ratio in the reacted material.

Pellet Number	Prefiring Stoichiometry
1	0.98 ZnO : 1 Ga_2O_3 : 0.02 $MnCO_3$
2	0.98 (0.95 ZnO : 0.05 CdO) : 1 Ga_2O_3 : 0.02 $MnCO_3$
3	0.98 (0.90 ZnO : 0.10 CdO) : 1 Ga_2O_3 : 0.02 $MnCO_3$
4	0.98 (0.85 ZnO : 0.15 CdO) : 1 Ga_2O_3 : 0.02 $MnCO_3$
5	0.98 (0.80 ZnO : 0.20 CdO) : 1 Ga_2O_3 : 0.02 $MnCO_3$
6	0.98 (0.75 ZnO : 0.25 CdO) : 1 Ga_2O_3 : 0.02 $MnCO_3$
7	0.98 (0.50 ZnO : 0.50 CdO) : 1 Ga_2O_3 : 0.02 $MnCO_3$

Table 6-1) Stoichiometry of powders prior to firing. The powders were weighed out in order to obtain a 1:2 ratio of M^{II}:M^{III} assuming the manganese is incorporated in its 2+ oxidation state, and no material is lost during firing. It is nor know how much material is lost during firing. However, as will be shown, the composition of the films as deposited is close to the stoichiometries shown in the table, indicating cadmium loss is not dramatic.

6.1.1 Powder Structure

The crystal structure of the reacted powders was determined by X-ray diffraction. For all starting mixtures the spinel phase was formed during the firing, as can be seen in the X-ray patterns shown in Figure 6-1. For all compositions, a certain amount of excess Ga_2O_3 is visible, with peaks appearing at 32° and 39°, however the peaks remain very small up to pellet 4, in which 15% of the ZnO was replaced with CdO in the unfired material. Because of its significantly higher vapour pressure, the appearance of excess Ga_2O_3 is most likely the result of CdO sublimation, although the possibility of ZnO loss can not be disregarded (CdO reaches a vapour pressure of 10^{-4} torr at 530°C, while ZnO does not reach this pressure until ~ 1800°C).

There is no visible shift in the position of the 311 peak in the X-ray diffraction zinc is systematically replaced by cadmium in the starting powders. If zinc were completely substituted by cadmium, the (311) peak located at 35.7° in $ZnGa_2O_4$ would shift 1.1° on a 2θ scale. Since the powders produced for this study never have more than 50% of the ZnO substituted by CdO prior to firing, this small shift can not be resolved in these scans. Also since some of the Cd is lost during firing, the lattice dilation will be reduced significantly by the presence of vacancies in the resulting spinel.

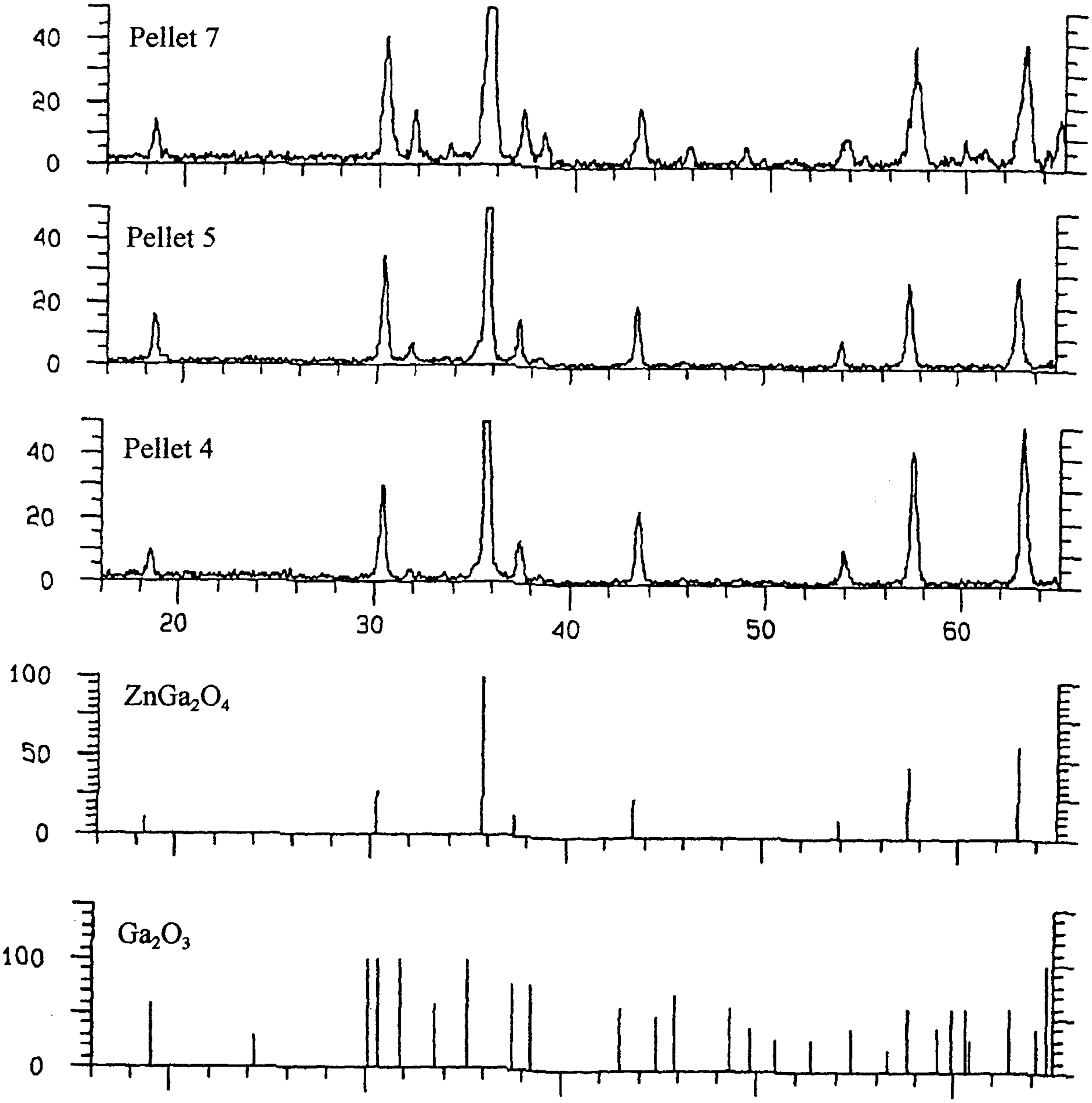

Figure 6-1) X-ray diffraction patterns for vacuum fired powders.

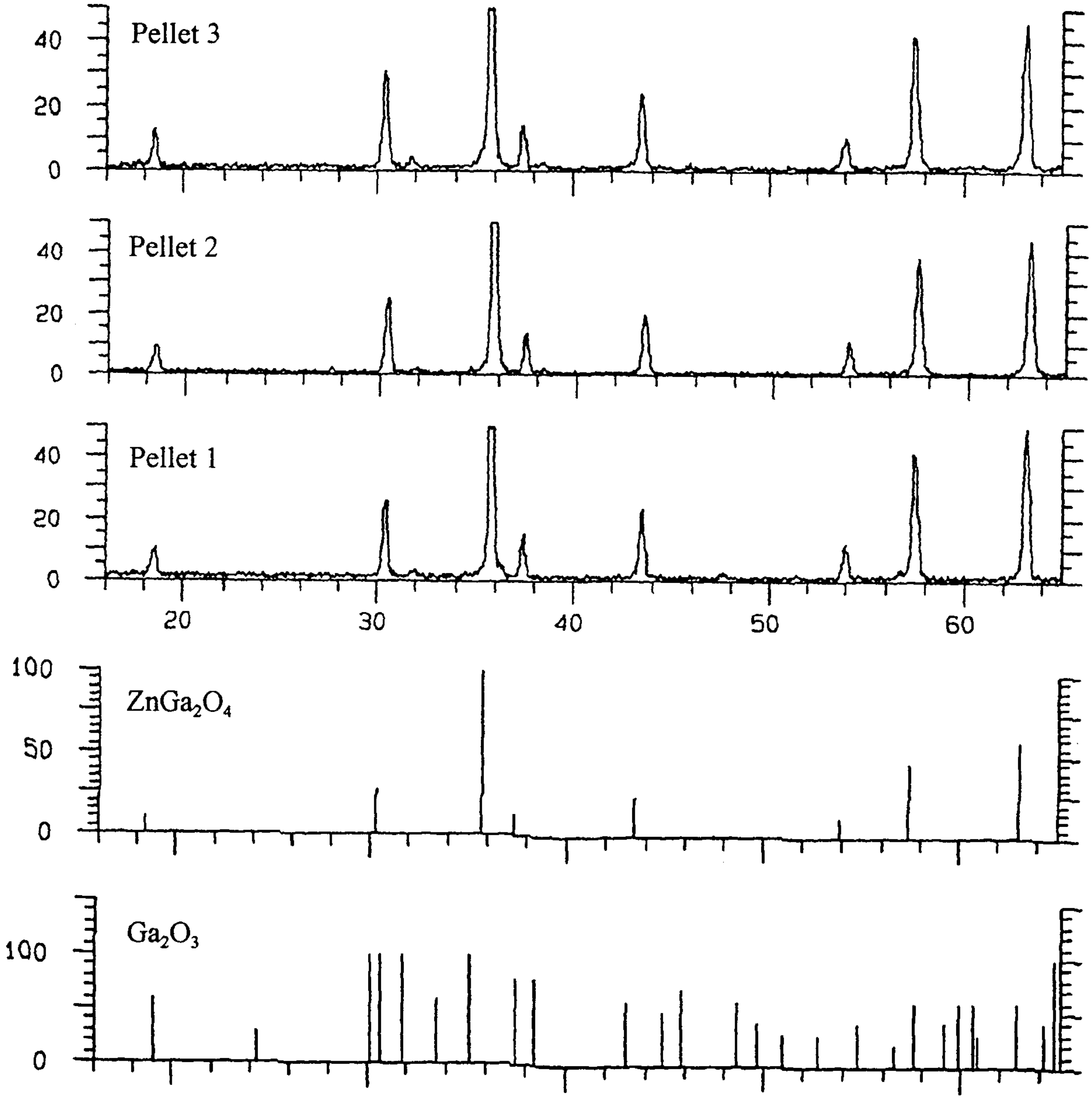

Figure 6-1 (*Continued)*

6.1.2 Powder Photoluminescence

The powders showed a green emission when excited by 254 nm radiation. No luminescence was visible when the phosphors were exposed to 365 nm light. The emission spectrum was independent of whether the powders were cadmium processed or not, peaking at 504 nm, as shown in Figure 6-2. The emission has the colour coordinates x=0.08 and y=0.69, which compares favourably with results previously reported for $ZnGa_2O_4$:Mn in the literature (Tran et al., 1995). The observed independence of the emission spectrum with changes in composition is contrary to the slight red shift with increasing cadmium in the starting materials, which has been previously observed (Kim et al., 1999).

While the emission spectrum is unchanged by the cadmium processing, there is a small but observable change in the excitation spectra of the various powders, shown in Figure 6-3. The broad hump in the range of 265 nm to 310 nm is the direct excitation of the manganese dopants. Because the absorption of energy is both parity and spin forbidden, the peak is quite small. The breadth of the peak is due to the thermal broadening of the various states into which the ion can be excited. The much more intense peak at ~240 nm corresponds to the absorption of excitation energy by the host lattice, and the subsequent transfer to the manganese ion. Because the fine structure of the manganese states is masked by the thermal broadening it is not possible from this measurement to determine if cadmium processing affects the manganese absorption

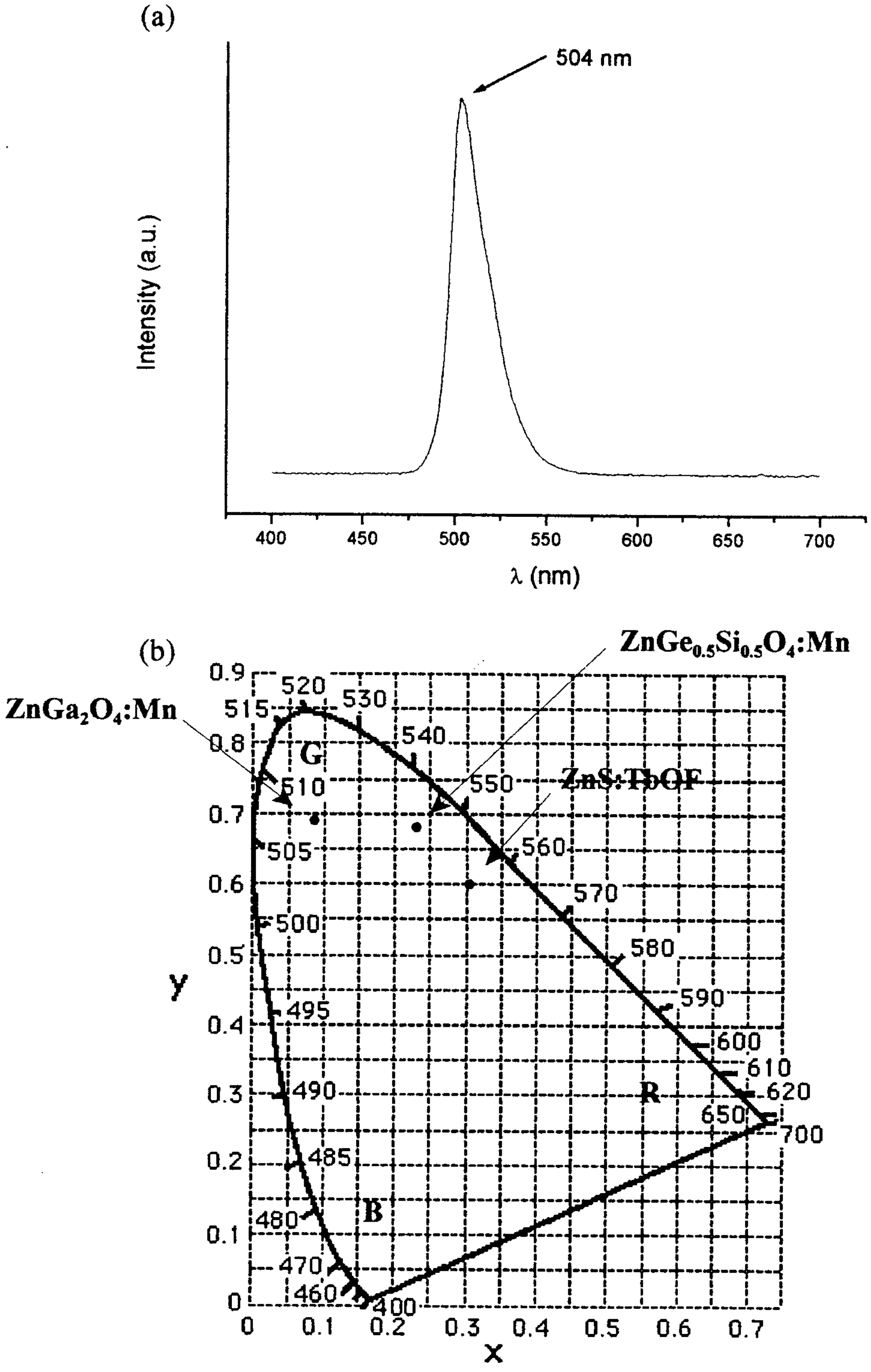

Figure 6-2) PL emission spectrum (a) and colour coordinates (b) of ZnGa$_2$O$_4$:Mn. Relative colour coordinates of other green EL phosphors are shown (Kitai, 1997a).

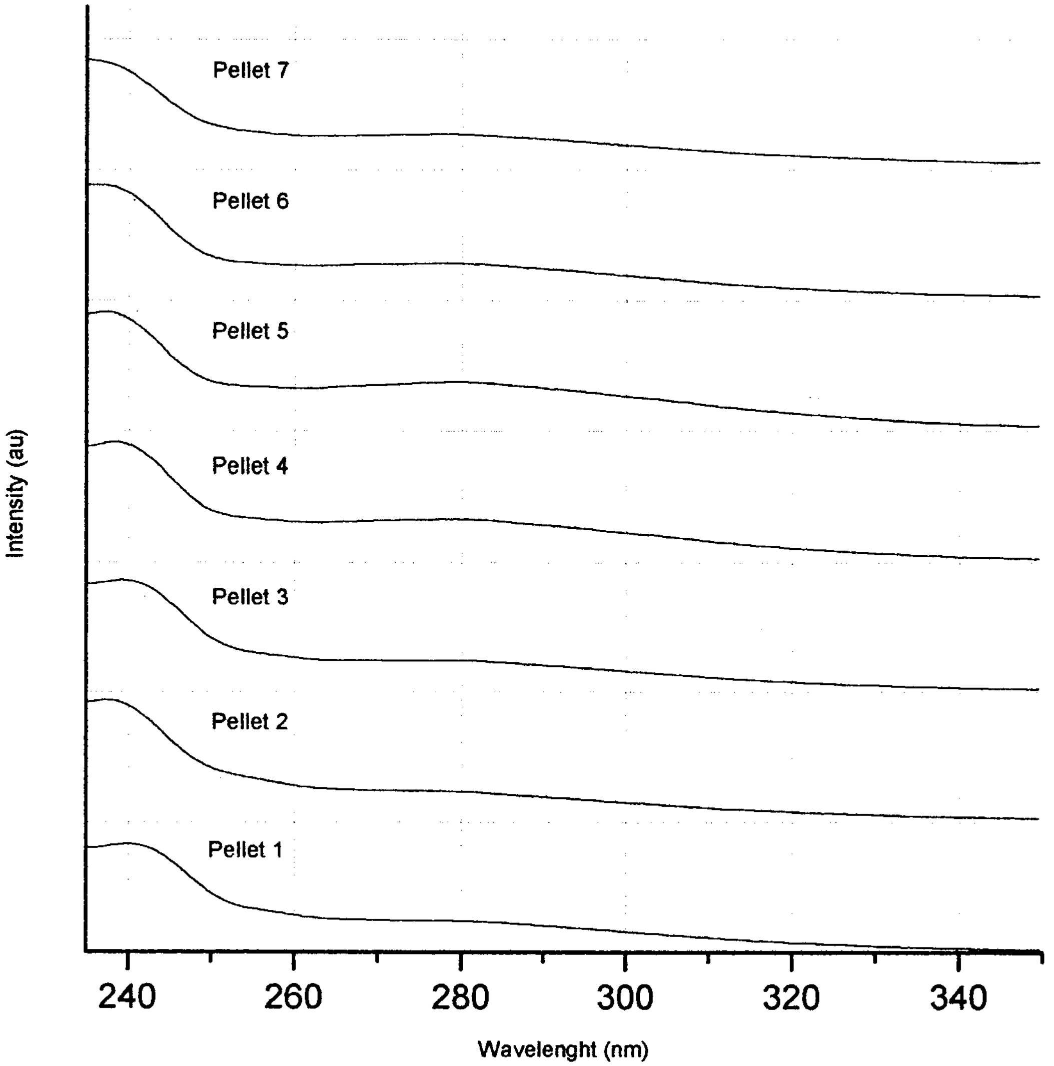

Figure 6-3) Excitation spectra of manganese activated powders. The composition of the unfired powders can be found in table 6-1. The emission was monitored at 504 nm. The small, broad peak centred at ~280 nm corresponds to the direct excitation of the manganese ions. The more intense peak at ~240 nm is due to the absorption of the excitation energy by the host crystal. This energy is then transferred to the manganese ions, which then release it as visible light.

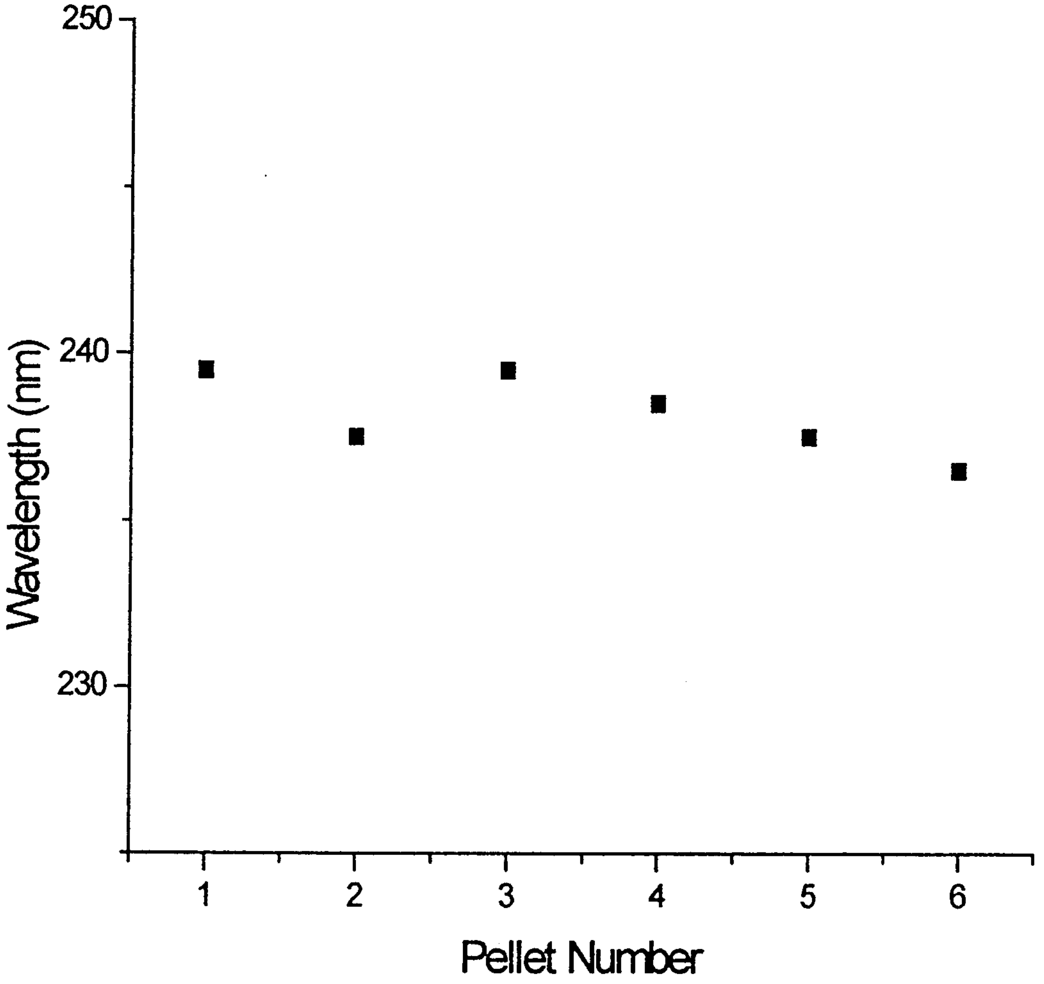

Figure 6-4) Position of the maximum of the host-lattice peak in the excitation spectra. Pellet number refers to those presented in table 6-1.

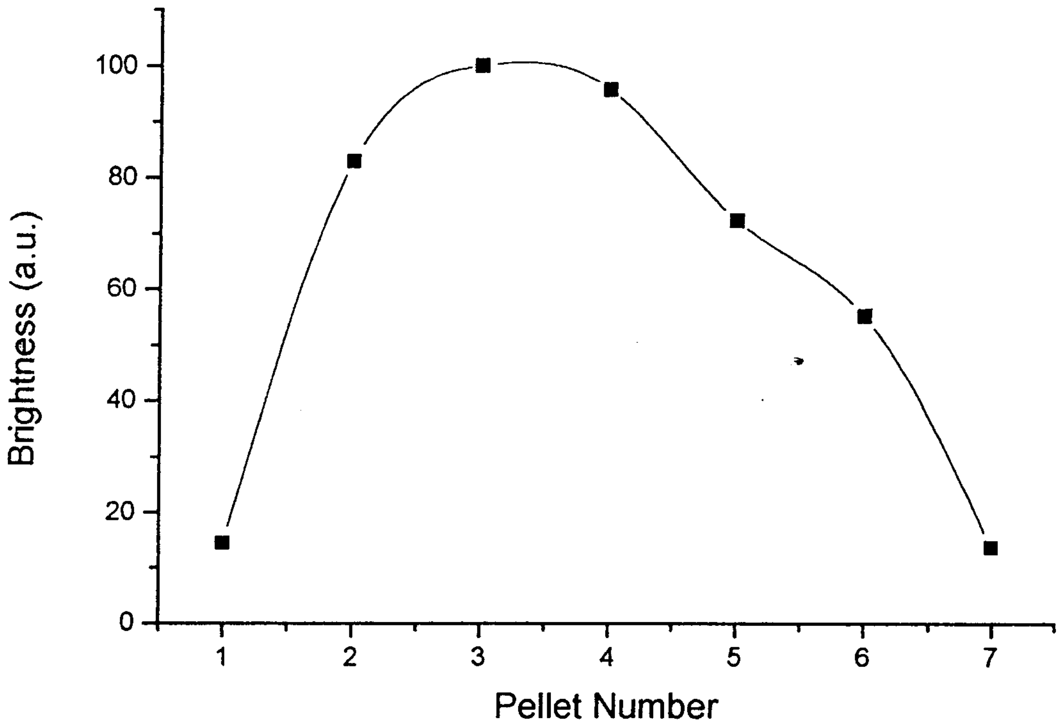

Figure 6-5) Variation in PL brightness of $Cd_xZn_{1-x}Ga_2O_4$:Mn powders fired in vacuum.

bands, however there is a measurable shift in the peak of the host lattice excitation. This is illustrated in Figure 6-4. As the cadmium content of the starting powders is increased, there is a small but progressive blue shift in the excitation peak, going from 239.5 nm to 236.5 nm with an accuracy of ±0.25 nm. The reason for the sharp deviation of the pellet 2 measurement from this overall trend is not clear, however the consistency of the shift observed in the other pellets would seem to indicate that the pellet 2 measurement is anomalous. The host lattice absorption in zinc gallate is believed to occur at the gallate group (Shea et al., 1994). This absorption may be perturbed by the substitution of cadmium for zinc since the A and the gallium occupied B sites share a common oxygen, resulting in the shift in the absorption spectrum.

The effect of cadmium processing also manifests itself in the relative PL intensity, as shown in Figure 6-5. The unmodified $ZnGa_2O_4$ material shows relatively weak PL. These powders had a slightly rose body colour indicating the presence on Mn^{3+} in the powders in addition to the desired Mn^{2+} (Shea, 1993). All cadmium processed powders had a pure white body colour, indicating that the manganese had incorporated in the desired 2+ oxidation state. The maximum PL intensity was obtained from powders processed with 10%-15% CdO substituted for ZnO in the starting materials. Improved Mn^{2+} incorporation is the result of the vacancies left by Cd sublimation, which speeds the diffusion process. Nonstoichiometry has been shown to result in a linear increase in the diffusion coefficient as the vacancy concentration is increased (Flynn, 1972). Reduction of manganese to the 2+ state also appears easier in the cadmium processed compounds.

6.2 Sputtered Thin Films

In the unfired sputtering targets, zinc was steadily substituted by cadmium in a series of increasing percentages. The fraction of zinc which was replaced in each target prior to firing is the same as the case of the powder material, and is shown again in Table 6-2. Note that the composition of the cadmium processed films after annealing is not represented by these compositions, as will be presented in the following section. It is important to note that the samples are identified according to the cadmium contents of the starting powder materials, and not the thin films.

Target	$(CdO)_x(ZnO)_{1-x}:Ga_2O_3:Mn$
1	x=0
2	0.05
3	0.10
4	0.15
5	0.20
6	0.25
7	0.50

Table 6-2) Fraction of zinc substituted by cadmium in sputtering targets prior to firing.

6.2.1 Composition, Structure and Morphology of Thin Films

As deposited, the films showed no photo- or electroluminescence, and therefore post-deposition annealing was required in order to obtain light emission. The lack of luminescence is due to the high oxygen partial pressure during deposition, which was necessary in order to avoid the loss of cadmium, and to a lesser extent zinc. The X-ray diffraction measurements were taken immediately after the anneal, while atomic force microscopy and scanning electron microscopy were performed on completed EL devices on which the electro-optic measurements had already been made.

6.2.1.1 Film Composition

The composition of the films as deposited is shown in Table 6-3. The cadmium content of the films is close to that of the starting composition of the targets. However at the lower cadmium contents there is an excess of cadmium, being as much as twice the as high as the composition of the prefired targets. At the highest cadmium contents though (targets 6 and 7) the cadmium to gallium ratio in the films is essentially identical to that of the unfired targets. The zinc content in all films is within 10% of that of the target starting materials.

The composition does not remain constant during annealing. The change in composition can be seen quite clearly in the EDX spectra of cadmium processed films

Target Number	Target Composition (Before Firing)	EDX Film Composition
1	$ZnGa_2O_4$	$Zn_{0.89}Ga_2O_n$
2	$Cd_{0.05}Zn_{0.95}Ga_2O_4$	$Zn_{0.93}Cd_{0.10}Ga_2O_n$
3	$Cd_{0.10}Zn_{0.90}Ga_2O_4$	$Zn_{0.85}Cd_{0.18}Ga_2O_n$
4	$Cd_{0.15}Zn_{0.85}Ga_2O_4$	$Zn_{0.86}Cd_{0.25}Ga_2O_n$
5	$Cd_{0.20}Zn_{0.80}Ga_2O_4$	$Zn_{0.85}Cd_{0.30}Ga_2O_n$
6	$Cd_{0.25}Zn_{0.75}Ga_2O_4$	$Zn_{0.73}Cd_{0.24}Ga_2O_n$
7	$Cd_{0.50}Zn_{0.50}Ga_2O_4$	$Zn_{0.50}Cd_{0.46}Ga_2O_n$

Table 6-3) Comparison of the target composition to that of the as deposited sputtered films. The composition was determined by EDX. Measurement uncertainty is ±10% for each element.

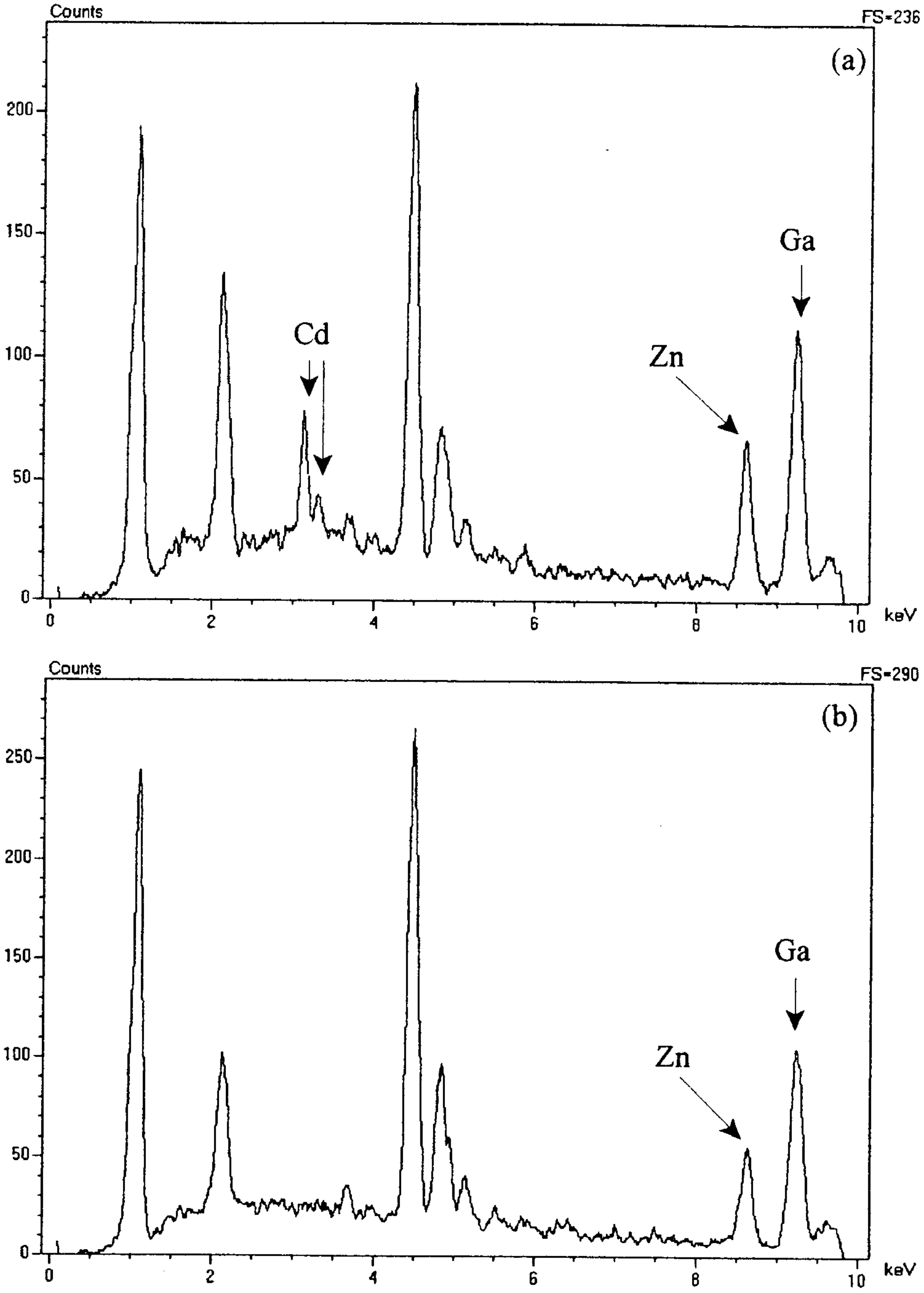

Figure 6-6) EDX spectra of thin films from target 4 annealed at (a) 600°C; (b) 700°C and (c) 900°C. All anneals were performed at 1×10^{-6} torr for 3 hours. Unlabeled peaks between 4 keV and 6 keV correspond to the substrate. The peak at ~2 keV is the gold coating on the samples, while the peak at ~1 keV is due to both the Zn and Ga L lines.

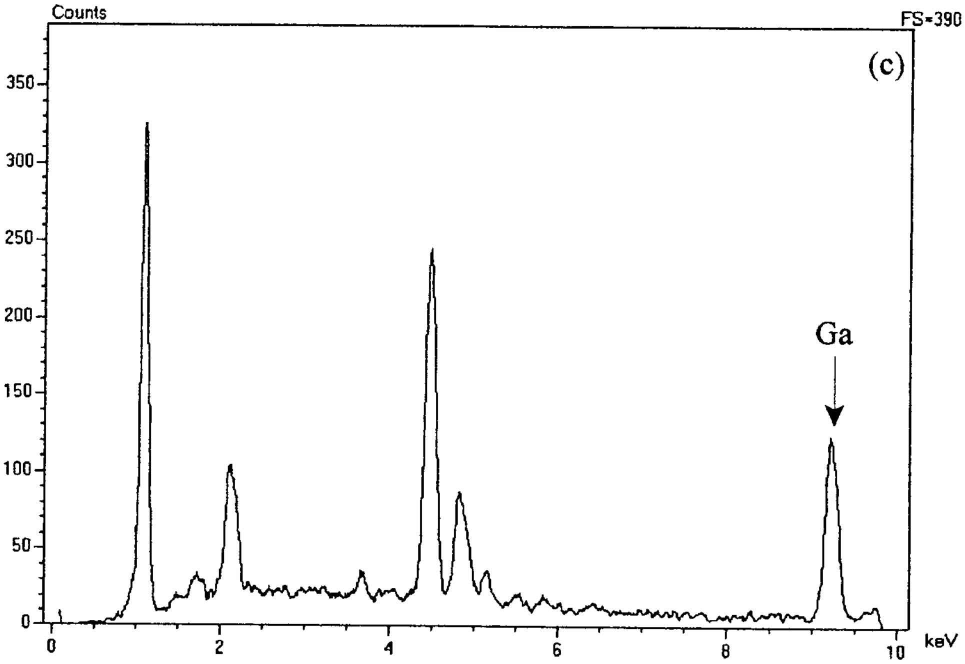

Figure 6-6 (*Continued*)

from target 4 annealed for photoluminescence measurements, as shown by the EDX spectra in Figure 6-6. The film annealed at 600°C for 3 hours at 1×10^{-6} torr still shows very strong cadmium X-ray lines, in addition to the peaks resulting from zinc and gallium. By 700°C, as shown in Figure 6-6 (b), the cadmium peaks have disappeared and only zinc and gallium are visible, indicating the complete loss of cadmium. The PL is extremely dim until all of the Cd has been lost. Annealing at still higher temperatures then results in the loss of zinc, as can be seen in the EDX spectrum of a film annealed at 900°C, Figure 6-6 (c).

The loss of cadmium and zinc is due to the low oxygen partial pressure during annealing (Cadmium reaches a vapour pressure of 10^{-4} torr at180°C versus ~530°C for CdO). The reduction of the films increases the volatility of cadmium and zinc, as is illustrated in Figure 6-7. The EDX spectrum of a film from target 7 shows strong peaks from cadmium, zinc and gallium in the as deposited film, Figure 6-7 (a). When the film is annealed in air the cadmium peaks are still easily visible, as shown in Figure 6-7 (b). When annealed in vacuum however, all of the cadmium is lost as shown in Figure 6-7 (c), indicating that the annealing atmosphere plays a dramatic role in controlling the composition of the films during post-deposition processing. Under vacuum conditions, the intensity of the zinc K_α line at 8.6 keV is also substantially reduced relative to the gallium peak. The as deposited and air annealed films showed no PL, while weak green PL was observed from the vacuum fired sample.

Loss of cadmium and zinc is also visible in the films which were used to make EL

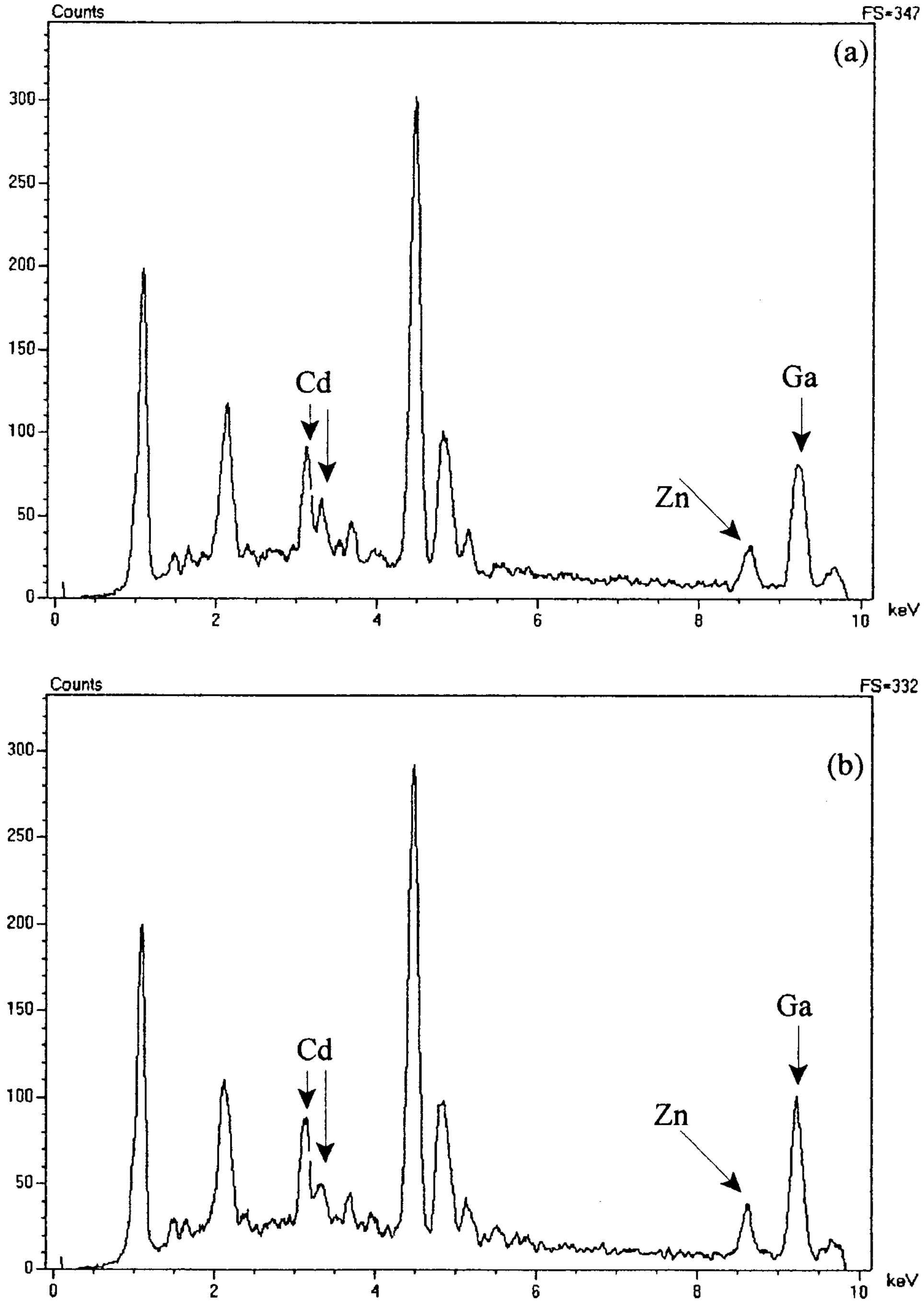

Figure 6-7) EDX of films sputtered from target 7 demonstrating the affect annealing atmosphere on cadmium loss. (a) as deposited; (b) air annealed; (c) vacuum annealed. All films were annealed for 3 hours at 750°C.

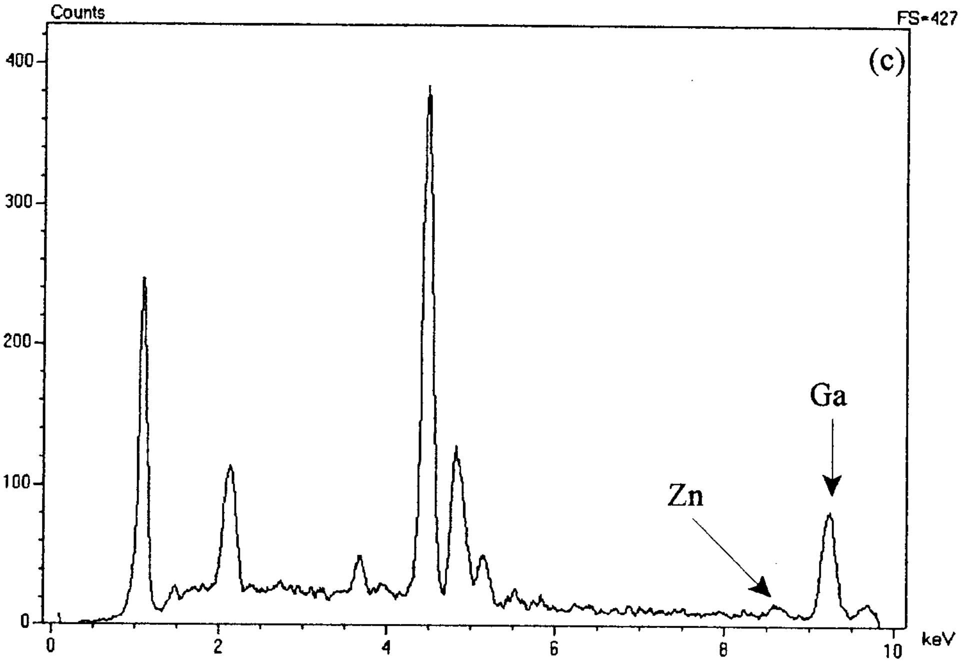

Figure 6-7 (*Continued*)

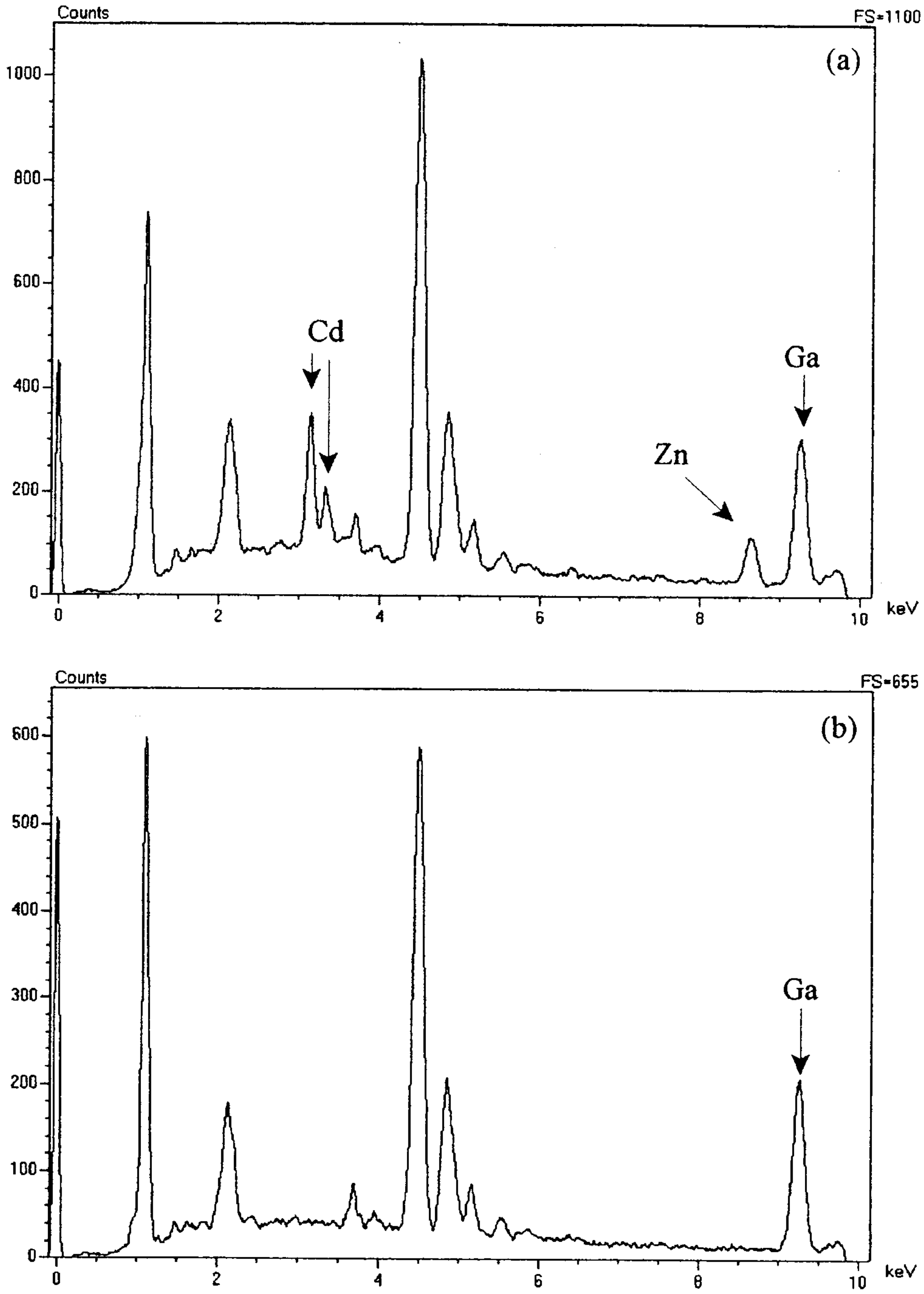

Figure 6-8) EDX spectra of films sputtered from target 7, a) as deposited; b) annealed in vacuum for 48 hours. The peak at ~1 keV is due to the zinc and gallium L lines. The peak at ~2k eV is the gold coating sputtered on the SEM samples. Peaks between 3.5 keV and 6 keV are due to the substrates. While the substrates are called barium titanate by the manufacturer, the two small peaks between 3.5 keV and 4 keV are the calcium K_α and K_β lines, respectively.

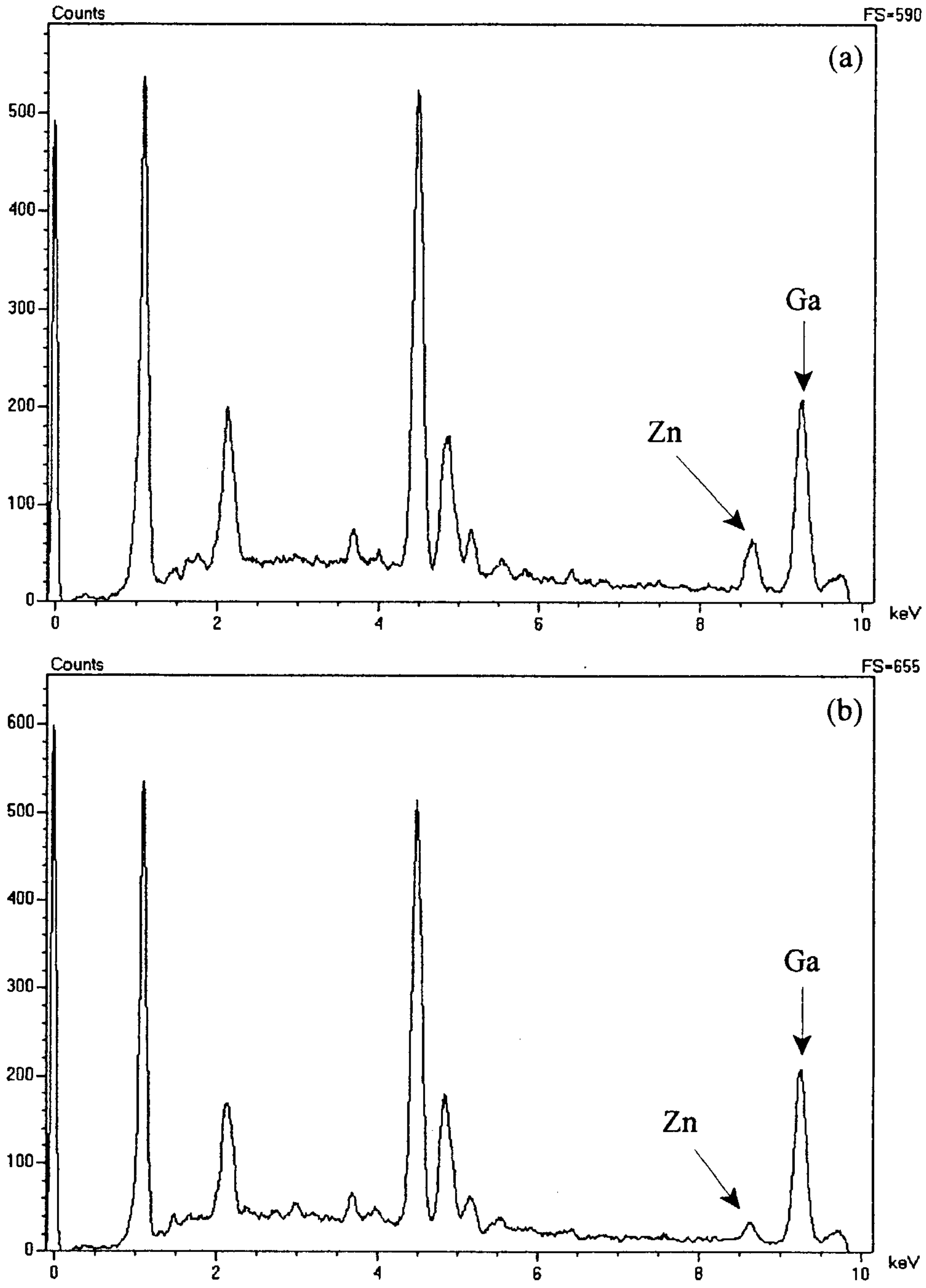

Figure 6-9) EDX spectra of films sputtered from target 6 annealed in vacuum at 900°C: a) 12 hour anneal; b) 48 hour anneal. The intensity of the zinc line drops significantly relative to that of the gallium.

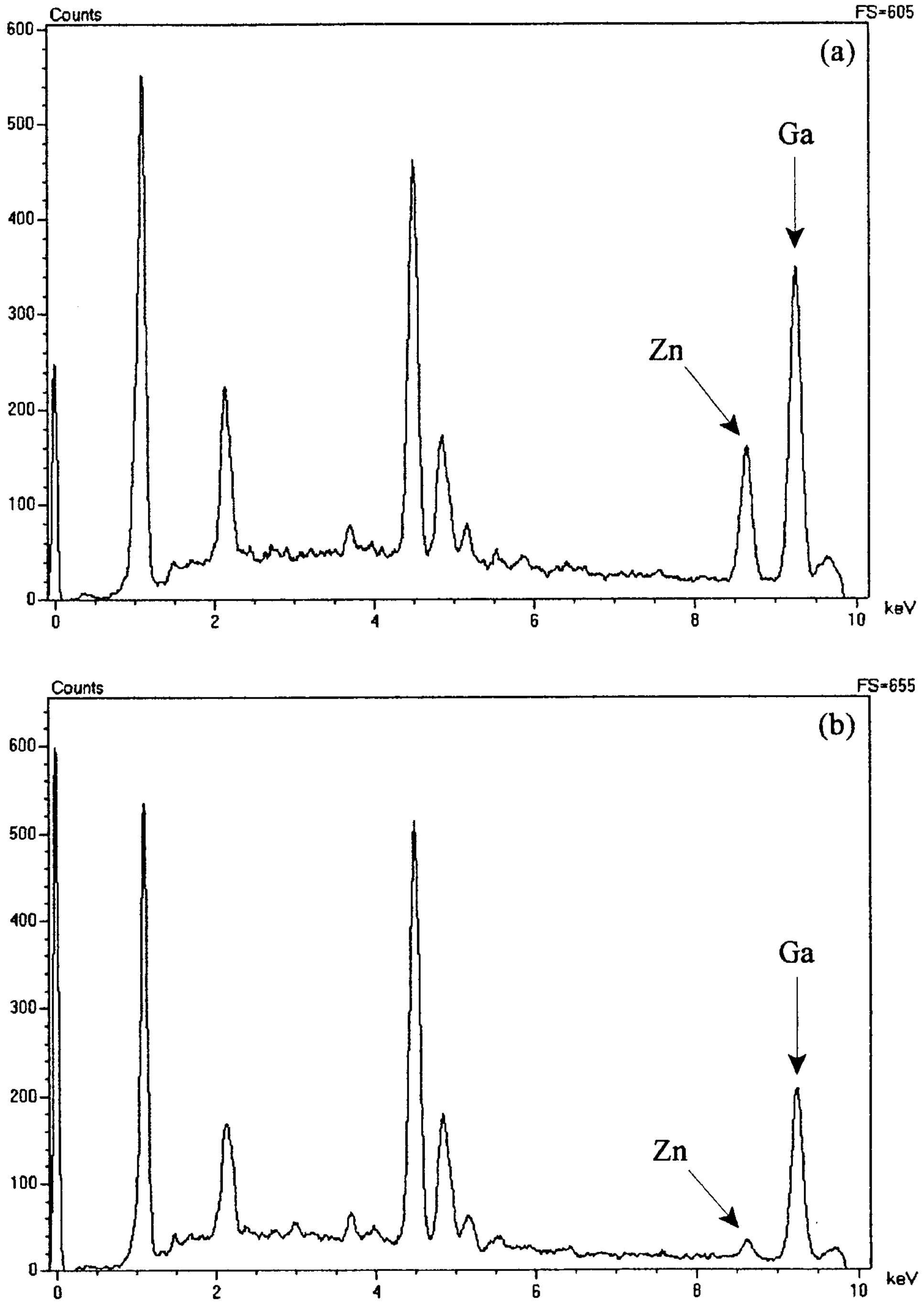

Figure 6-10) EDX spectra of films sputtered from target 1 and annealed at 900°C in vacuum: a) 12 hour anneal; b) 48 hour anneal. These films show the same zinc loss as cadmium containing films.

devices. In these cases, the pressure during the anneal was ~7.5x10^{-6} torr, almost an order of magnitude higher than the pressure in the furnace used to anneal the films for PL. Figure 6-8 shows the loss of both cadmium and zinc from films sputtered from target 7. Once again, both cadmium and zinc are clearly visible in the films as deposited, however after being annealed in vacuum for 48 hours at 900°C, all of the cadmium and zinc have been lost. Figures 6-9 (a) and (b) show cadmium processed films sputtered from target 6 annealed for 12 hours and 48 hours respectively. By 12 hours all of the cadmium is lost, however and strong zinc K_α line at 8.6 keV is still visible. In fact, EDX of films annealed for only one hour show no cadmium. The intensity of the zinc line relative to the gallium drops dramatically when the film is annealed for 48 hours. This effect is not dependent on cadmium being present in the as deposited films, as is shown in Figure 6-10. Here, a film from target 1 is shown after (a) being annealed for 12 hours, and (b) annealed for 48 hours. Once again the intensity of the zinc peaks drops dramatically relative to the gallium peak when the film is annealed for the longer time.

6.2.1.2 X-Ray Diffraction

The effect of annealing temperature on the X-ray structure of thin films is shown in Figures 6-11 and 6-12, for films sputtered from targets 1 and 2 respectively. All films were annealed in vacuum for 12 hours at 7.5x10^{-6} torr. The most obvious difference between the two sets of diffraction patterns is that films sputtered from target 1 (cadmium free; Figure 6-11) show a very strong (111) diffraction peak, relative to the $ZnGa_2O_4$ JCPD powder standard in which the (311) peak dominates. This texture is also observed in the films as deposited. As the films are annealed at higher temperatures, the intensity of the (111) peak decreases relative to that of the (311), indicating that the grains are assuming a more random distribution of orientations. For the cadmium processed films from target 2 shown in Figure 6-12, the diffraction pattern more closely resembles that of the more random orientation of the powder standard for all temperatures. In fact, this random orientation exists in these films as deposited, with the (111) line being much lower in intensity than the (311).

The change in diffraction patterns with increased annealing time is shown in Figure 6-13 for films from target 1, and in Figure 6-14 for films from target 4. Pressure during annealing was $7.5x10^{-6}$ torr. Once again the films from the cadmium free target (target 1) show a very strong (111) line relative to the (311) while the cadmium processed films (target 4) show diffraction patterns which much more closely resemble the $ZnGa_2O_4$ powder standard. Interestingly, the intensity of the (111) line relative to the (311) line in Figure 6-13 changes as the annealing time is increased. While the (111) intensity is substantially greater than that of the (311) line for films annealed for 1 to 3 hours, by 12 hours the two peaks have roughly the same intensity, suggesting a shift to a more random crystallographic orientation with longer annealing times. In both Figure 6-13 and 6-14 annealing the films for very long periods of time results in a disappearance of the diffraction lines corresponding to the spinel phase. It should be noted that this is

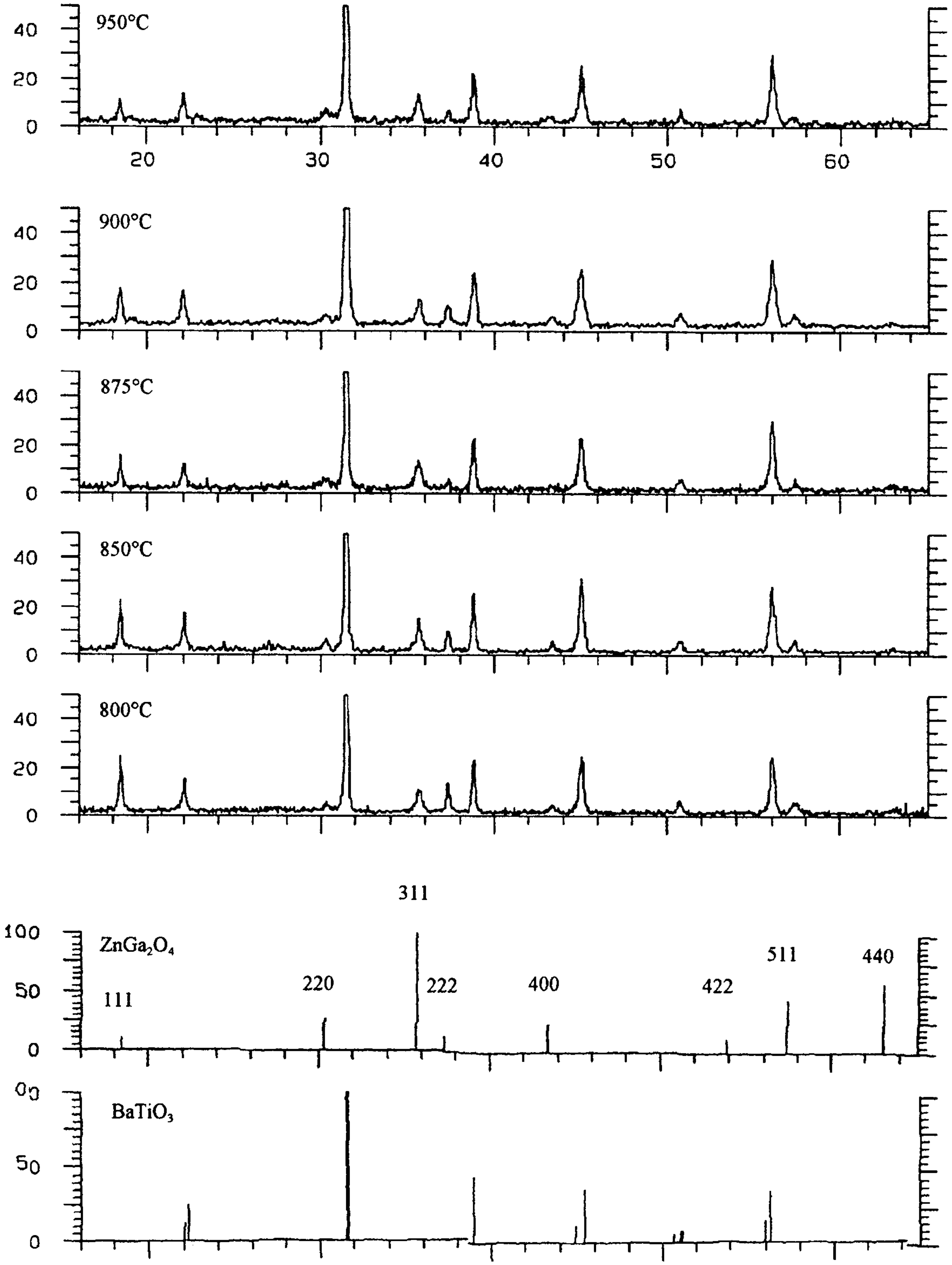

Figure 6-11) XRD patterns as a function of anneal temperature for films sputtered from target 1 annealed for12 hours.

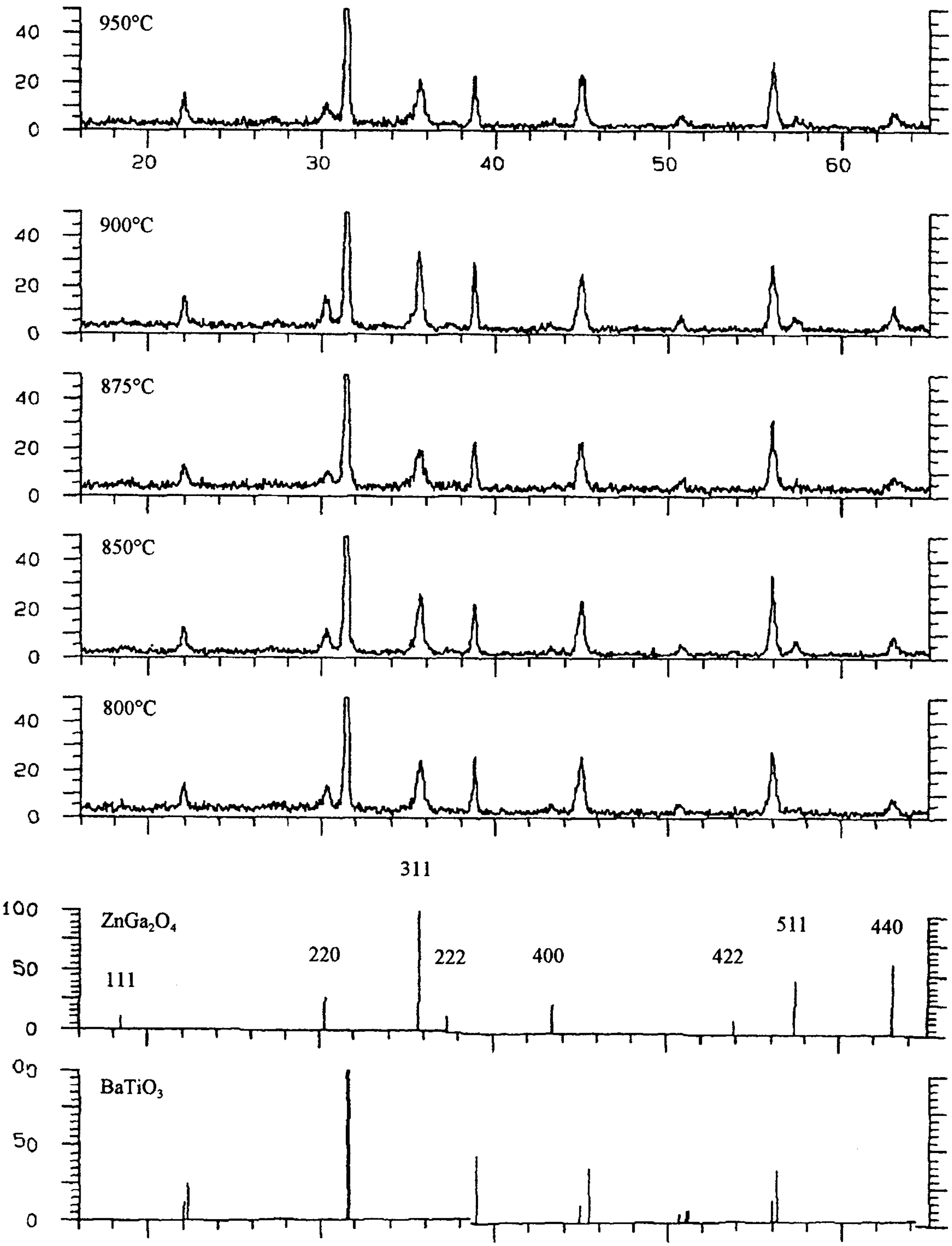

Figure 6-12) XRD patterns as a function of anneal temperature for films sputtered from target 2 annealed for12 hours.

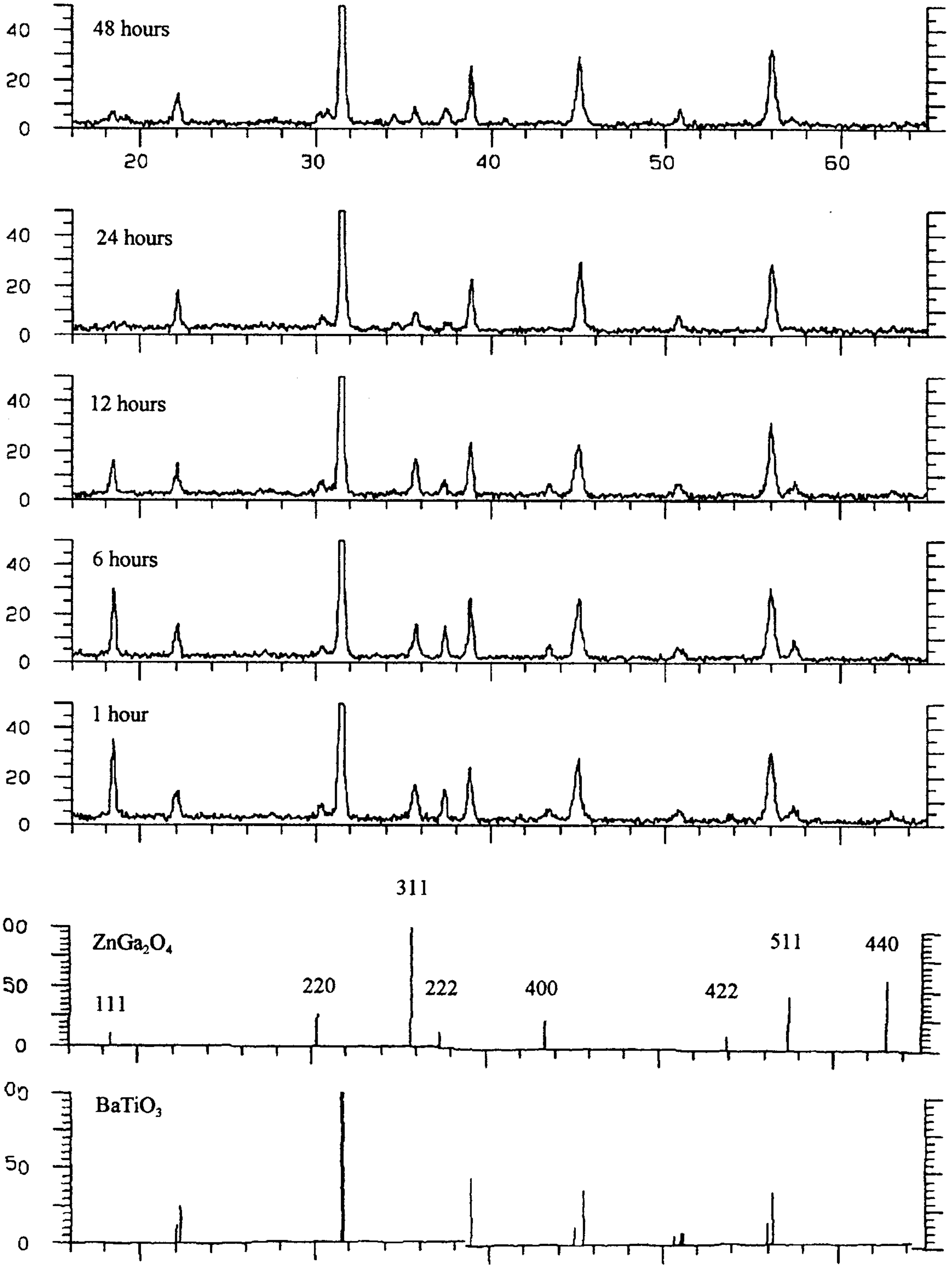

Figure 6-13) XRD patterns as a function of anneal time for films sputtering target 1 and fired at 900°C.

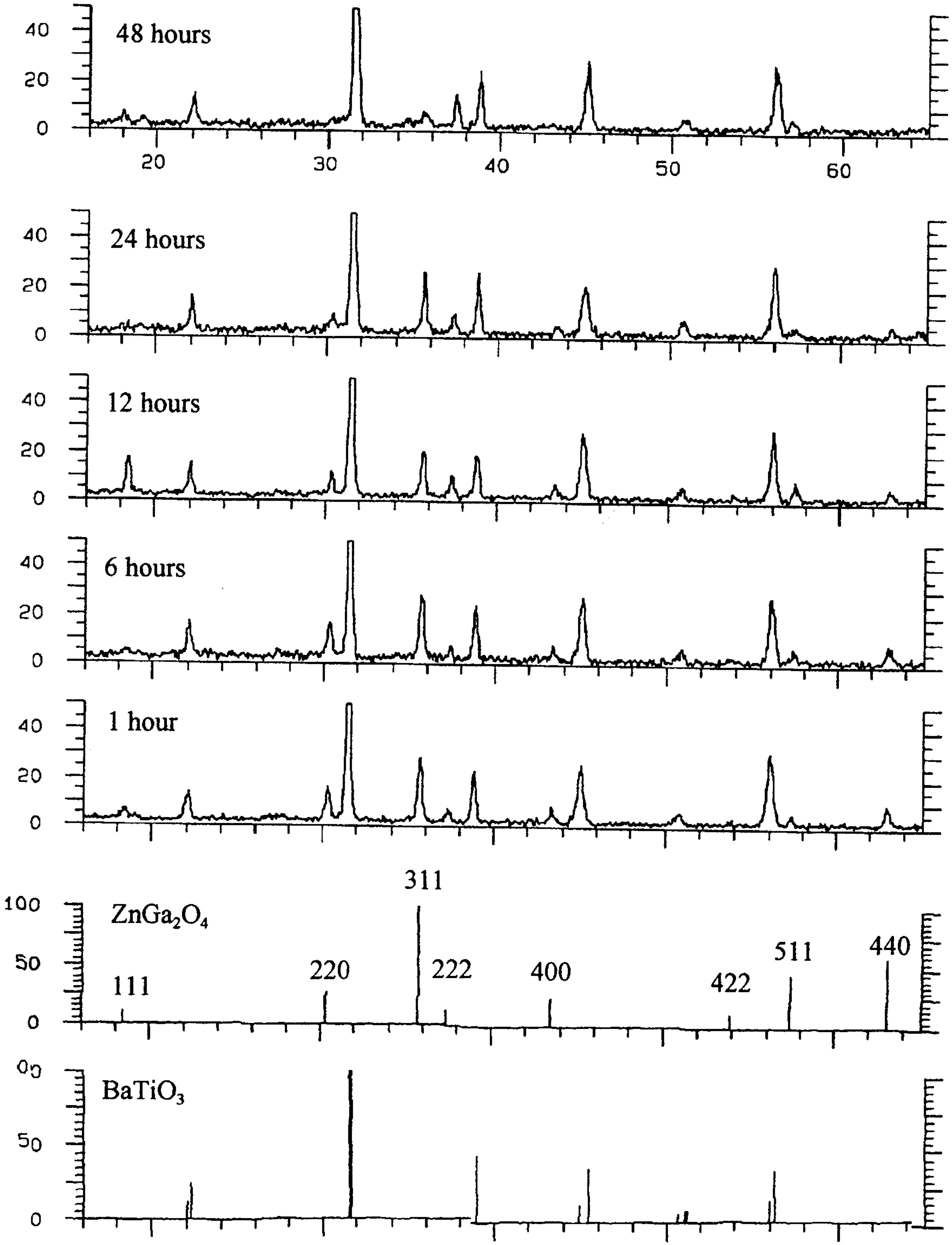

Figure 6-14) XRD patterns as a function of anneal time for films sputtered from target 4 and fired at 900°C.

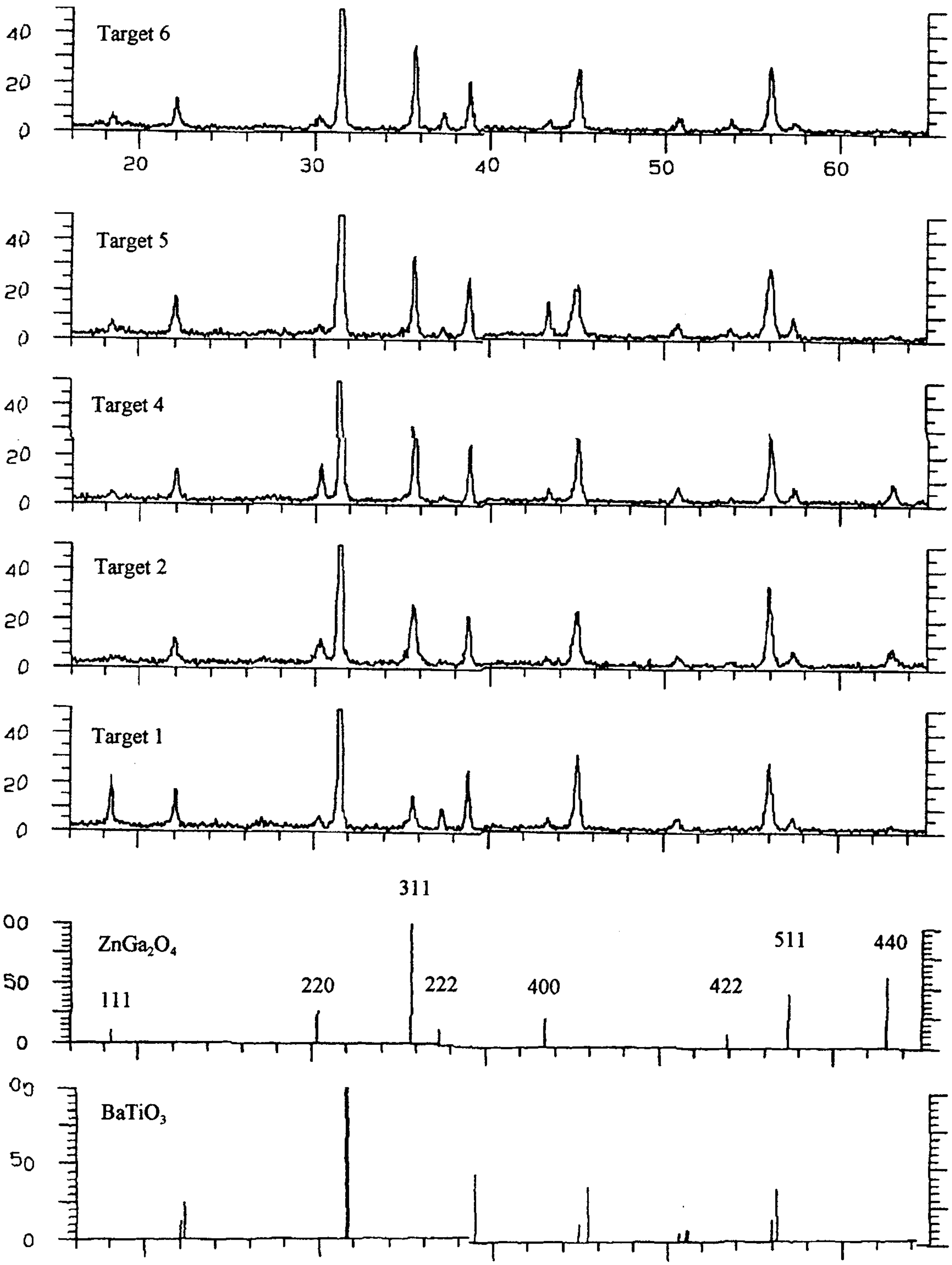

Figure 6-15) XRD patterns as a function of sputtering target for films annealed at 850°C for 12 hours.

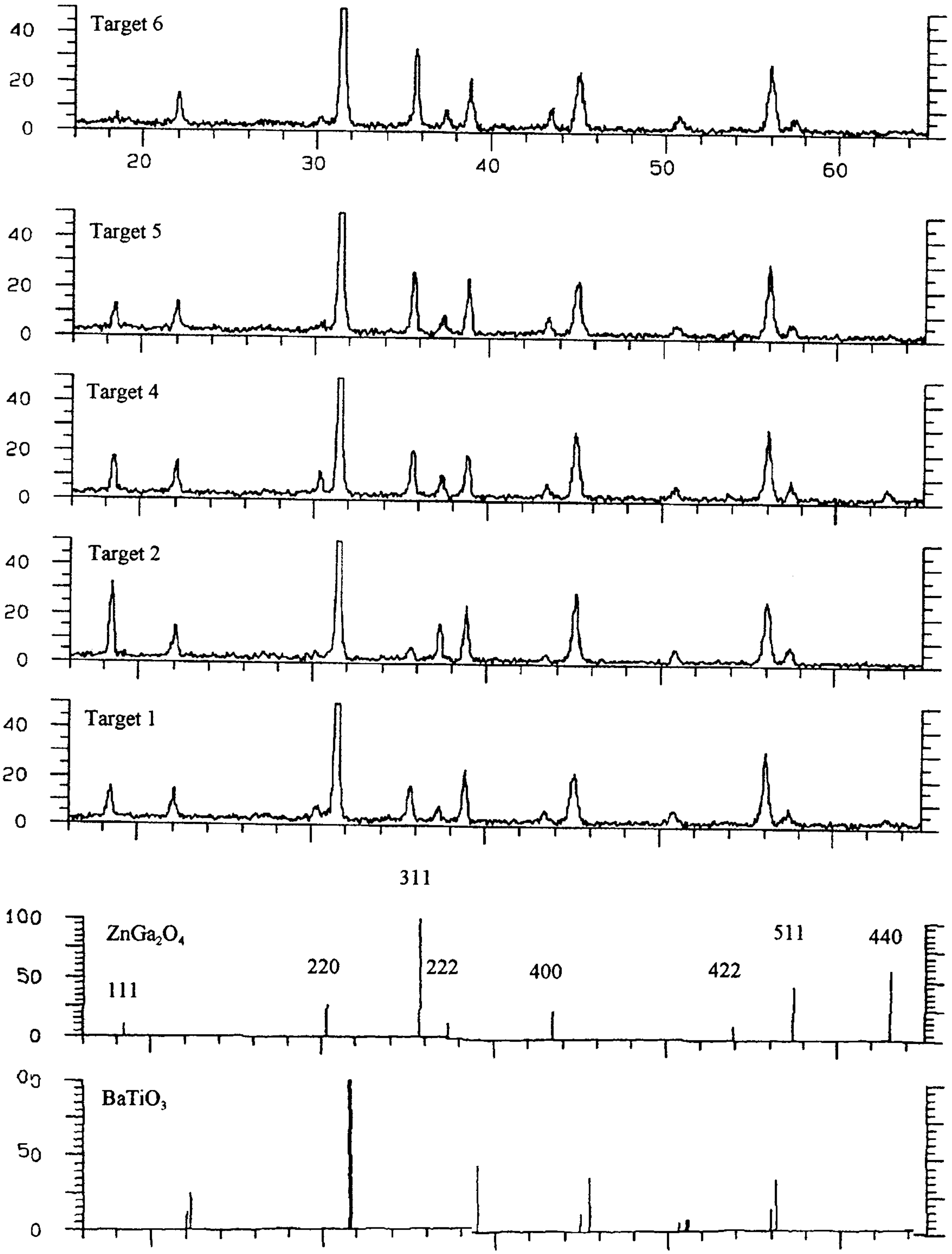

Figure 6-16) XRD patterns as a function of sputtering target for films annealed at 900°C for 12 hours.

not accompanied by the appearance of peaks corresponding to any of the simple oxides which were used to form the targets. This decrease in the XRD line intensities correlates with the sublimation of Cd and Zn from the films, as shown in the EDX data presented in Figures 6-8 to 6-10.

The dependence of the diffraction patterns on cadmium processing is illustrated in Figure 6-15 for films annealed 12 hours at 850°C, and in Figure 6-16 for films annealed for 12 hours at 900°C. Both sets of films were annealed at 7.5×10^{-6} torr. These two figures quite dramatically show the difference in the (111) peak intensity between films from target 1 and the cadmium processed films. In the case of Figure 6-16, the (111) peak is noticeable in all films up to those from target 5, while this is not the case for the diffraction patterns in Figure 6-15. There is also an anomalous (111) peak in films annealed for 12 hours, as shown in Figure 6-14. Despite this discrepancy, the tendency toward a more random, powder-like crystallographic orientation with cadmium processing is supported by the data in both Figures.

6.2.1.3 Scanning Electron Microscopy

All films looked similar when examined in the SEM, regardless of the degree of cadmium processing or the post-deposition annealing conditions. A typical surface morphology is shown in Figure 6-17. The most obvious feature of the films is the heavy degree to which they are pitted. The pits are distributed randomly across the surface of

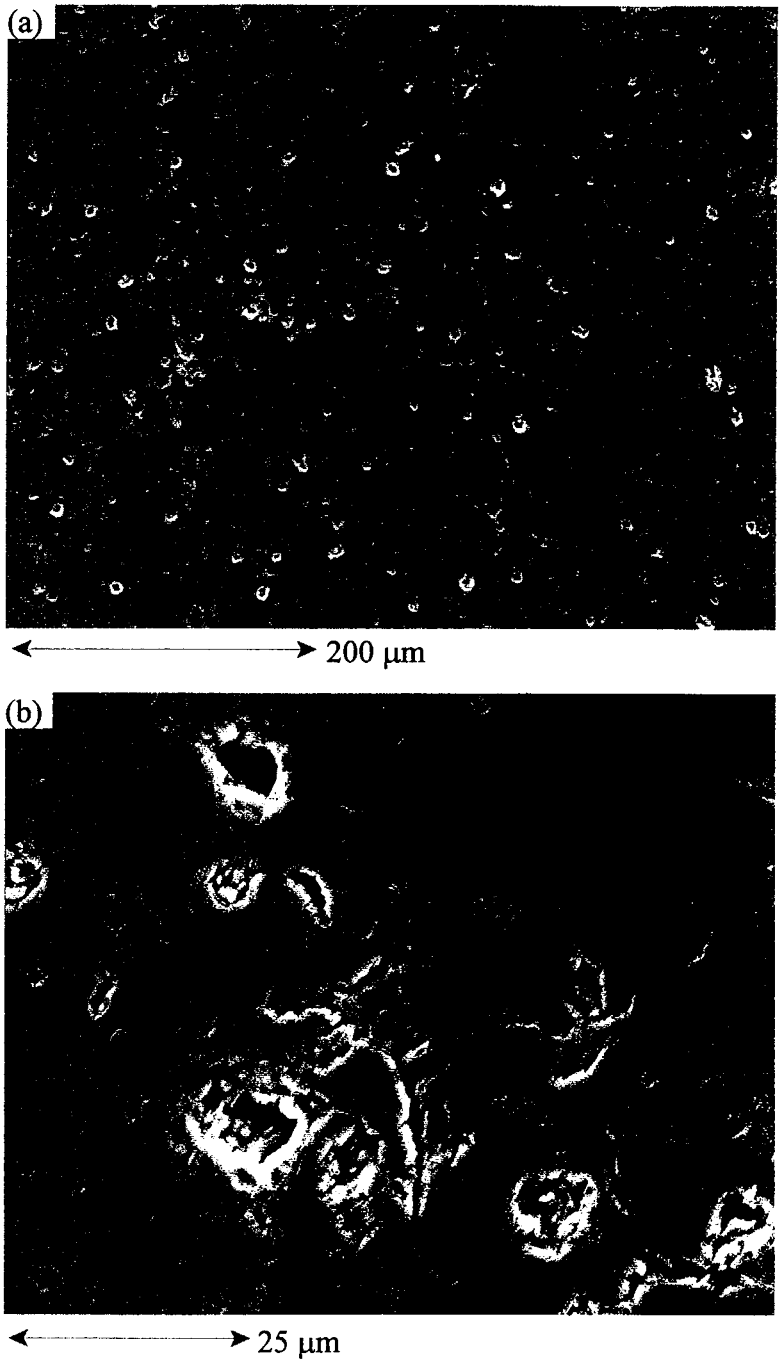

Figure 6-17) SEM micrographs showing the pitted surface of the phosphor films. In this case the film was sputtered from target 3 and was annealed at 900°C for 12 hours: a) low magnification image; b) high magnification image.

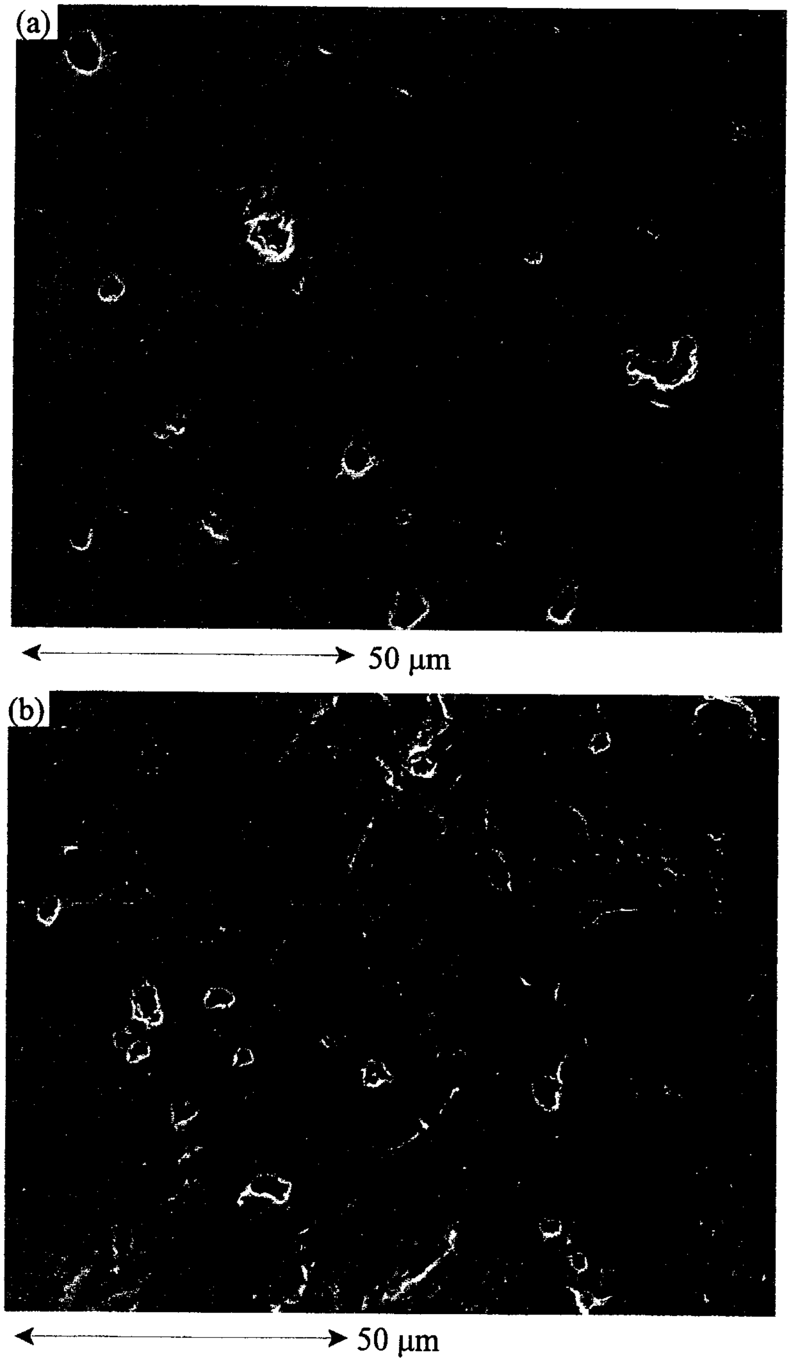

Figure 6-18) SEM micrographs showing the exposed pores in the $BaTiO_3$ substrate, a) the polished top surface; b) side view of a scribed and broken substrate.

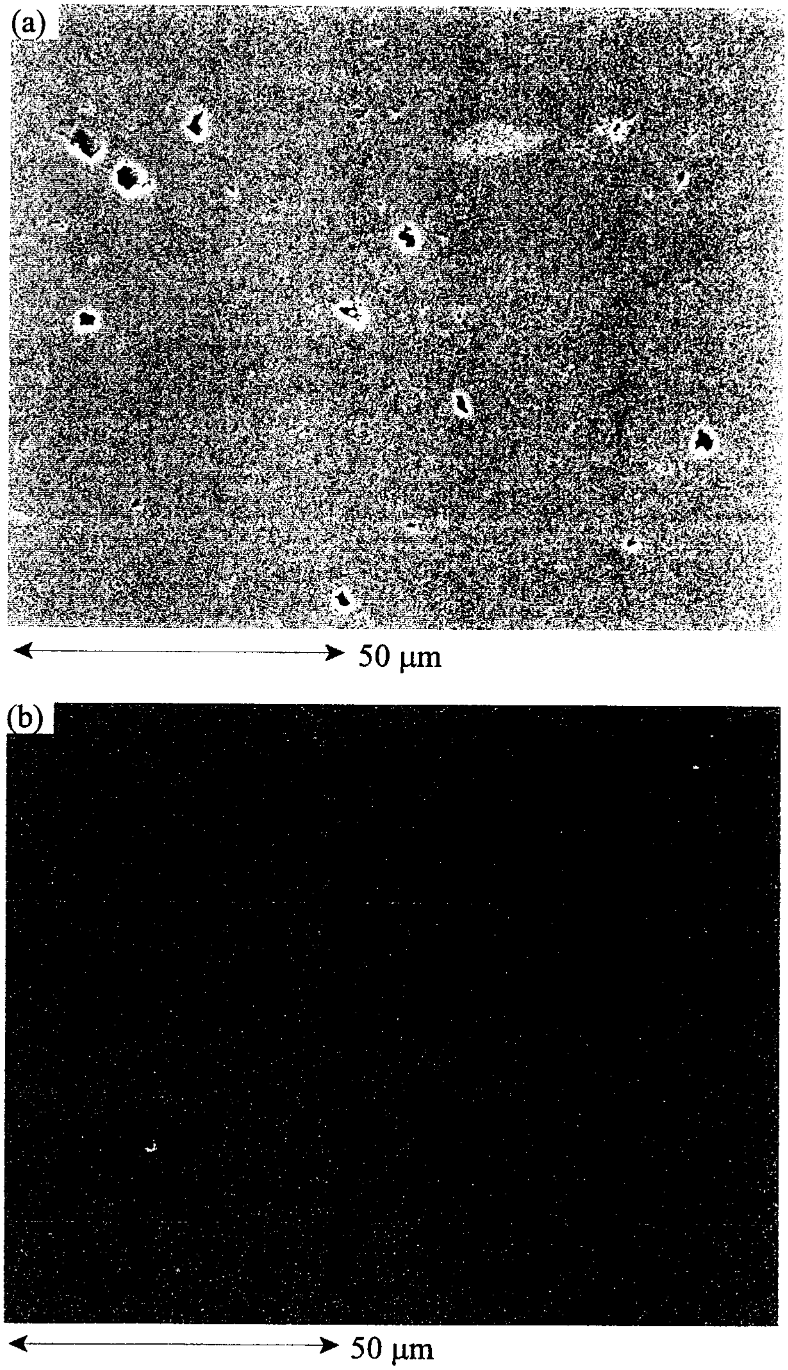

Figure 6-19) SEM micrographs of as deposited films from target 4: a) on a polished $BaTiO_3$ substrate; b) on a silicon substrate.

the film and extend to an unknown depth, potentially punching through the film, although this cannot be determined from these images.

The origin of this pitted morphology is the $BaTiO_3$ substrates used in these devices. The substrates are made by tape casting and contain a large number of pores. When the substrates are polished prior to the film deposition, many of these pores are exposed, resulting in a pitted substrate surface. This can be seen in Figure 6-18 which shows both a plan and profile view of the uncoated substrate material. The density of pits on the uncoated substrate is similar to that of the density of pits in the films. The films on $BaTiO_3$ substrates are compared to those on Si in Figure 6-19. Films on silicon are very smooth and unpitted in sharp contrast to those on the polished ceramic substrates, indicating the influence of the pores in the substrate.

Despite the X-ray diffraction which shows the films to be crystalline, the grain size is too small to be seen in the SEM. The microscope used has a maximum spatial resolution of approximately 1000Å. The fine grain size is due to the low deposition and annealing temperature relative to the melting point of the compound (>1500°C for stoichiometric $ZnGa_2O_4$).

6.2.1.4 Atomic Force Microscopy

High resolution images of the phosphor films were obtained via atomic force microscopy. The scans are all 1 μm x 1 μm and have a grayscale height range of 50 nm

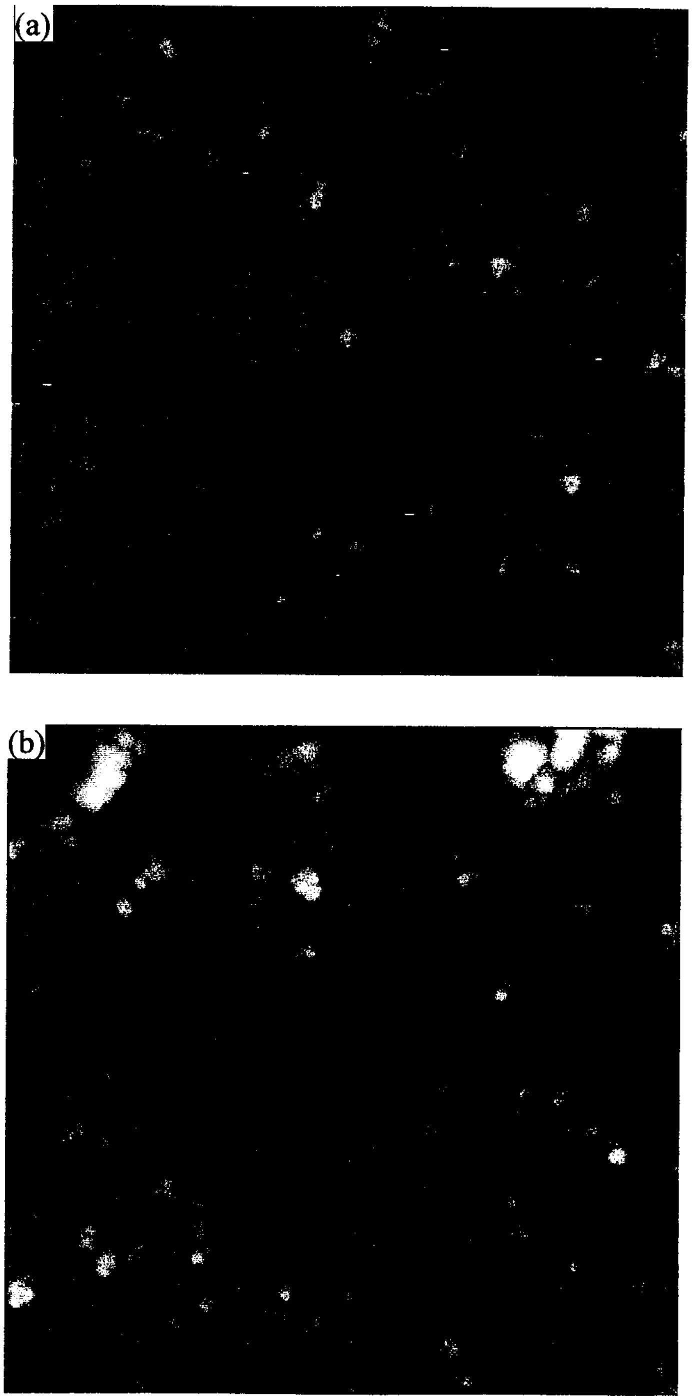

Figure 6-20) AFM micrographs of films from target 4 as a function of anneal temperature, a) 750°C; b) 800°C; c) 850°C; d) 875°C; e) 900°C; f) 950°C. The images are all 1μm x 1μm with a 50 nm grayscale.

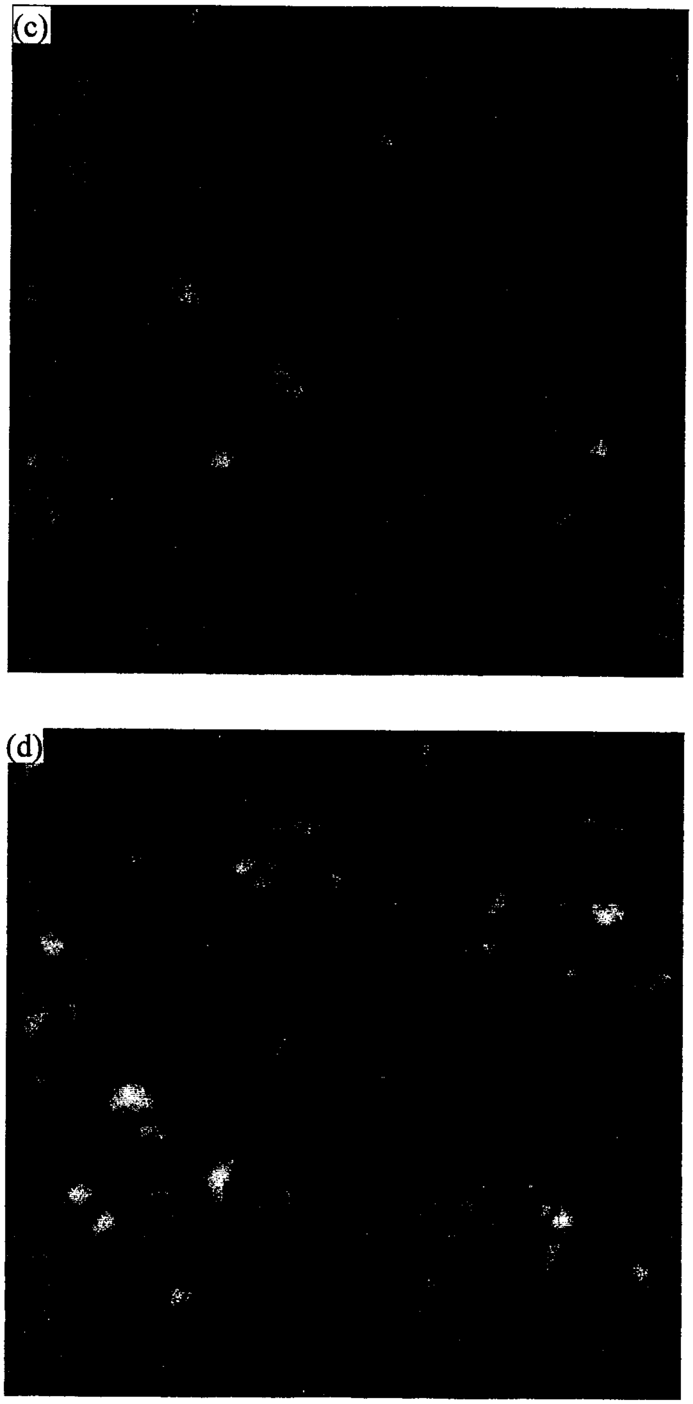

Figure 6-20 (*Continued*)

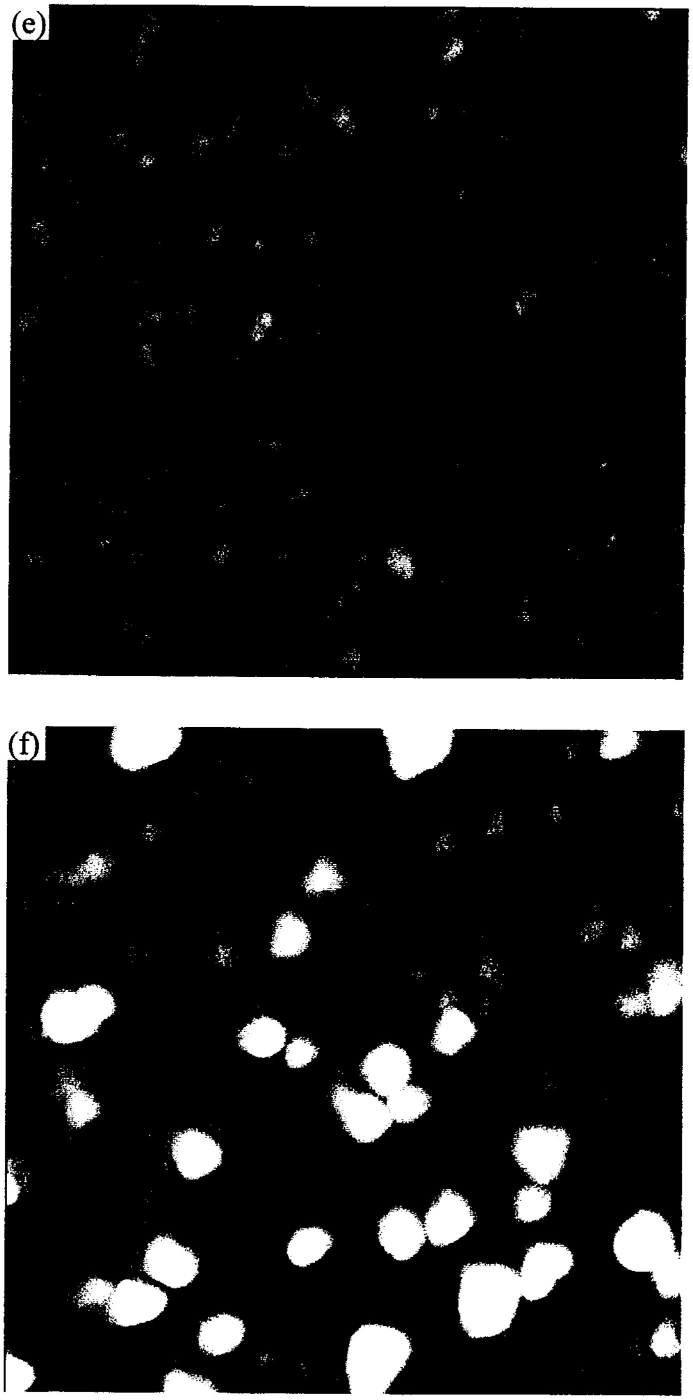

Figure 6-20 (*Continued*)

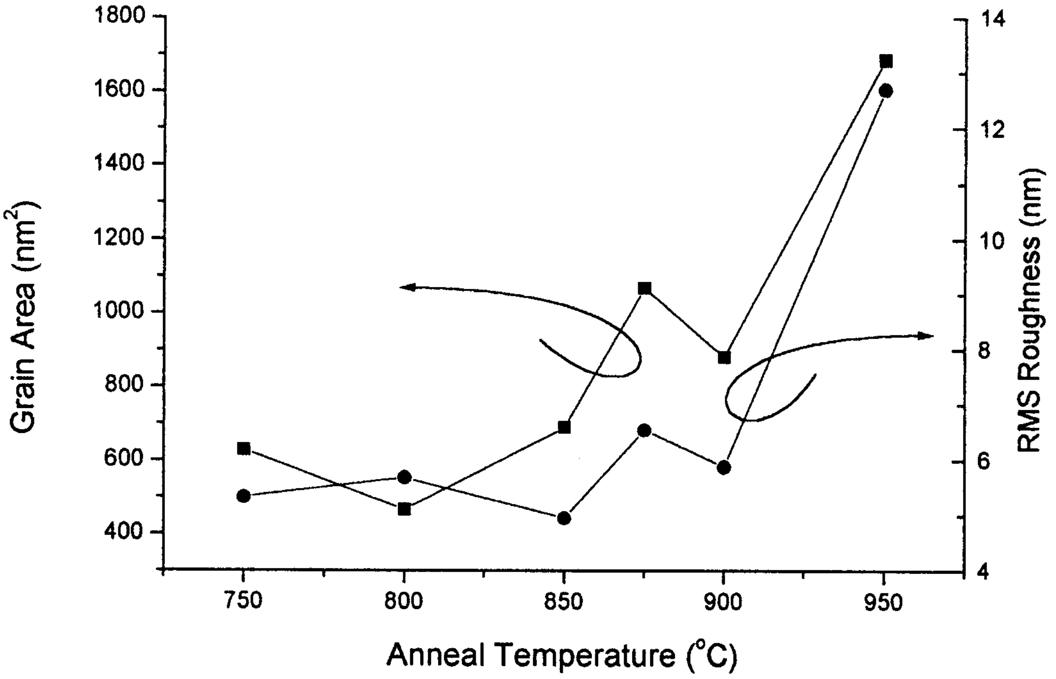

Figure 6-21) Grain area and surface roughness of films from target 4 annealed for 12 hours at various temperatures.

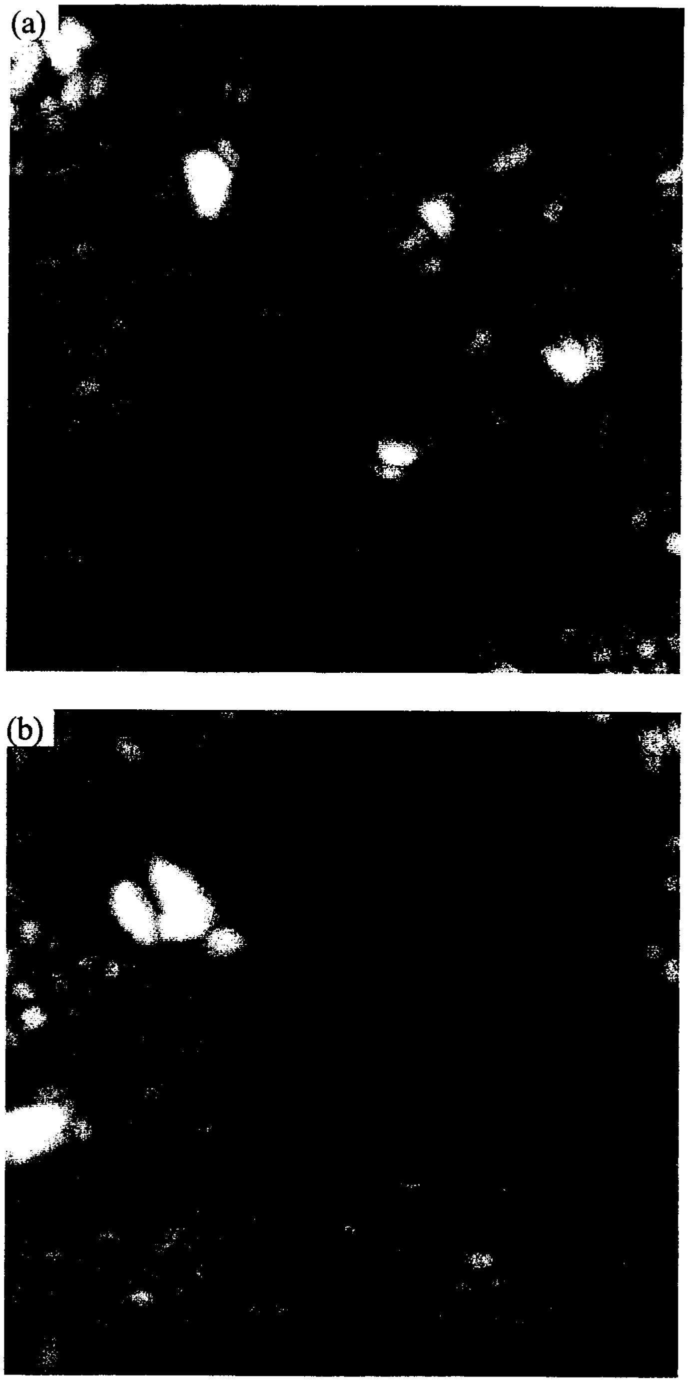

Figure 6-22) AFM micrographs of films from target 4 annealed at 900°C for various times, a) 1 hour; b) 3 hours; c) 6 hours; d) 12 hours; e) 24 hours; f) 48 hours. All images are 1 μm x 1 μm with a 50 nm grayscale.

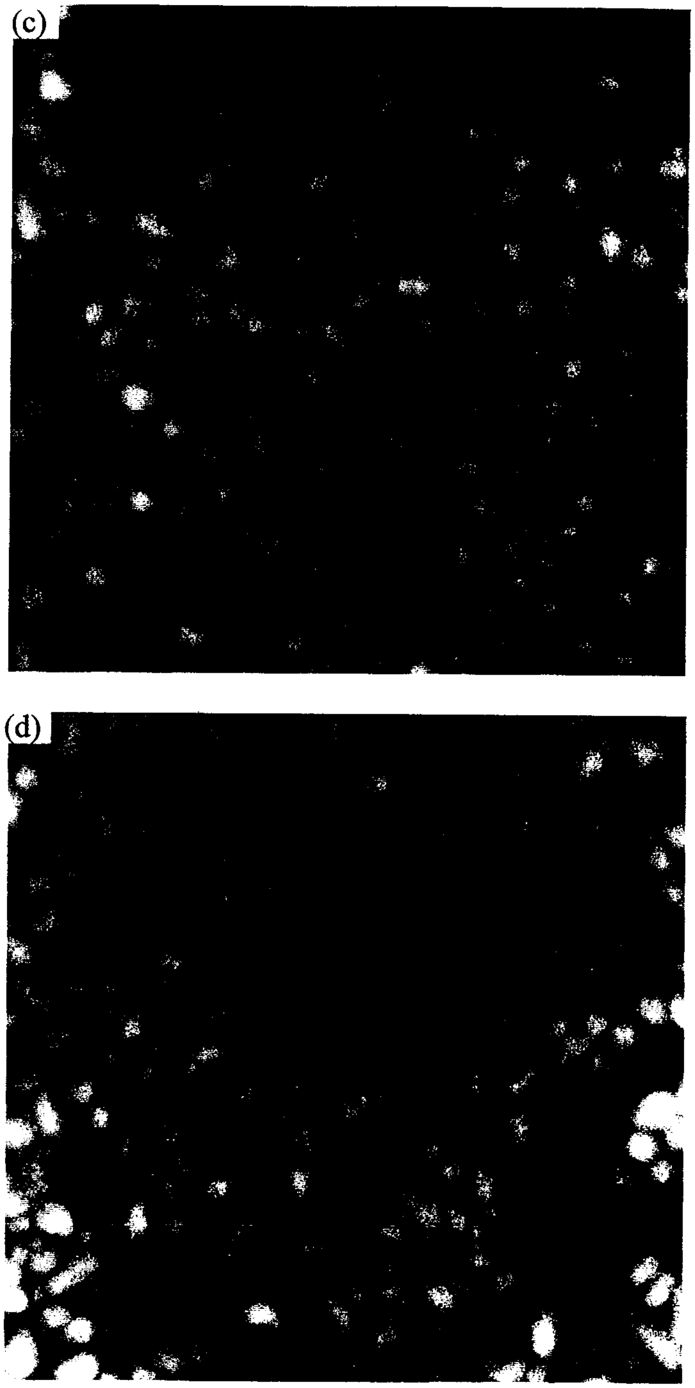

Figure 6-22 (*Continued*)

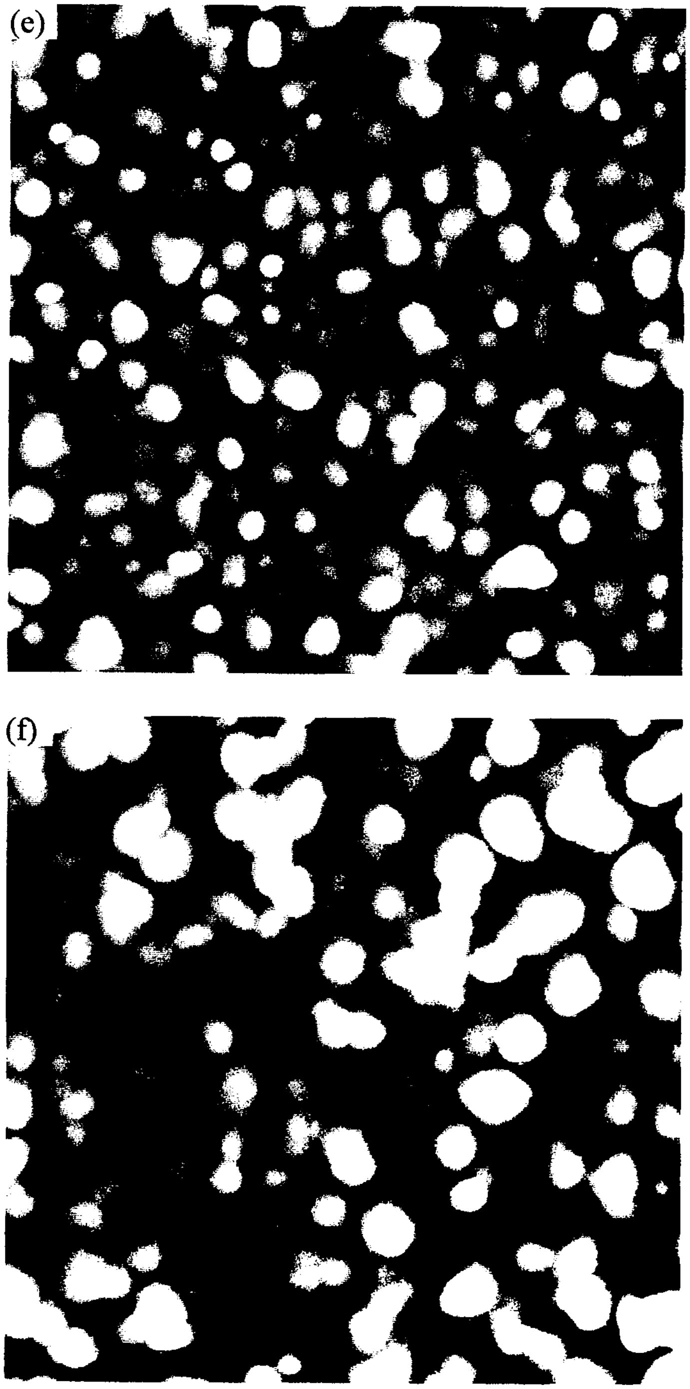

Figure 6-22 (*Continued*)

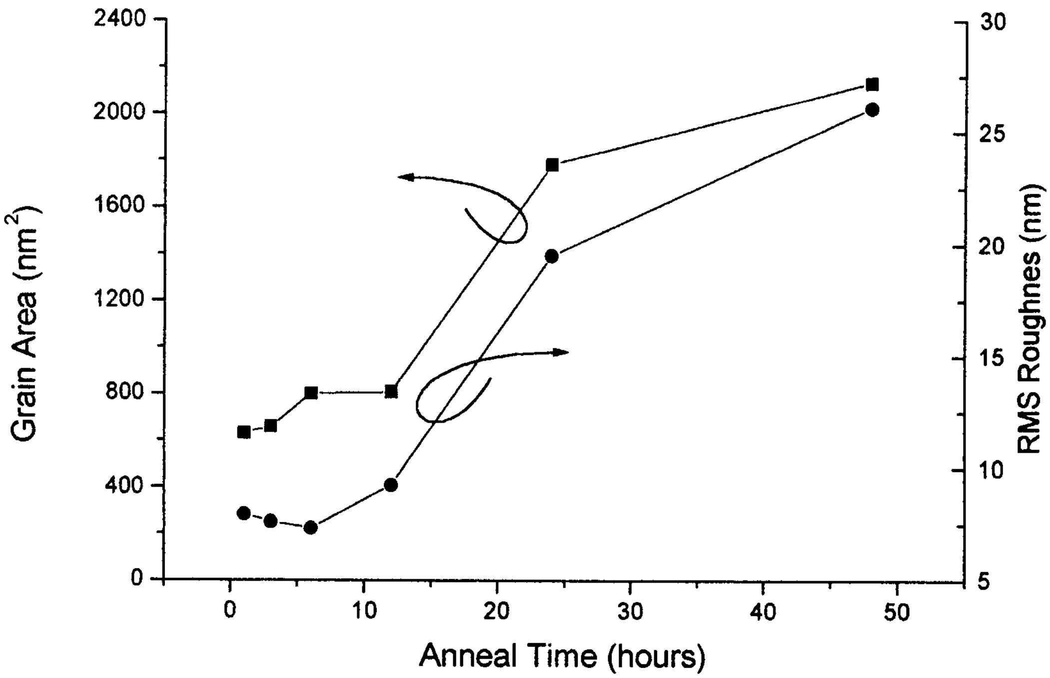

Figure 6-23) Grain area and surface roughness of films from target 4 annealed at 900°C for various times.

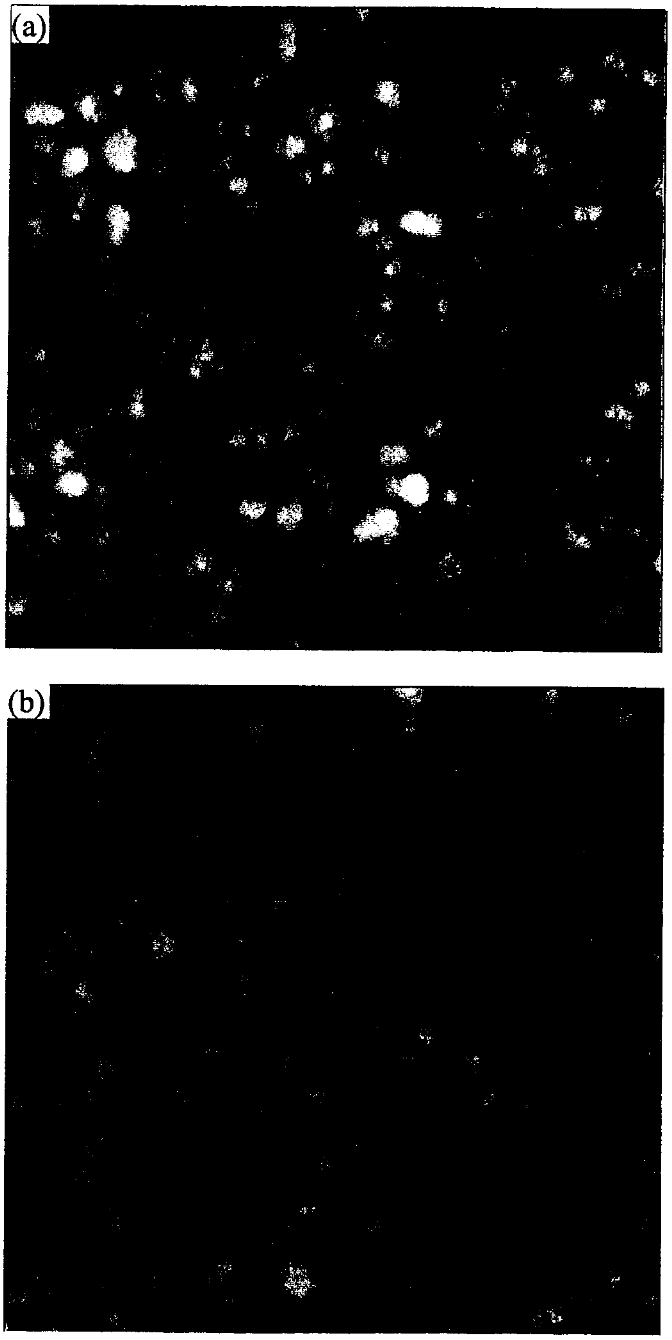

Figure 6-24) AFM micrographs of films annealed for 12 hours at 900°C as a function of cadmium content in the unfired target, a) target 1; b) target 2; c) target 3; d) target 4; e) target 5; f) target 6; g) target 7.

All images are 1 μm x 1 μm with a 50 nm grayscale.

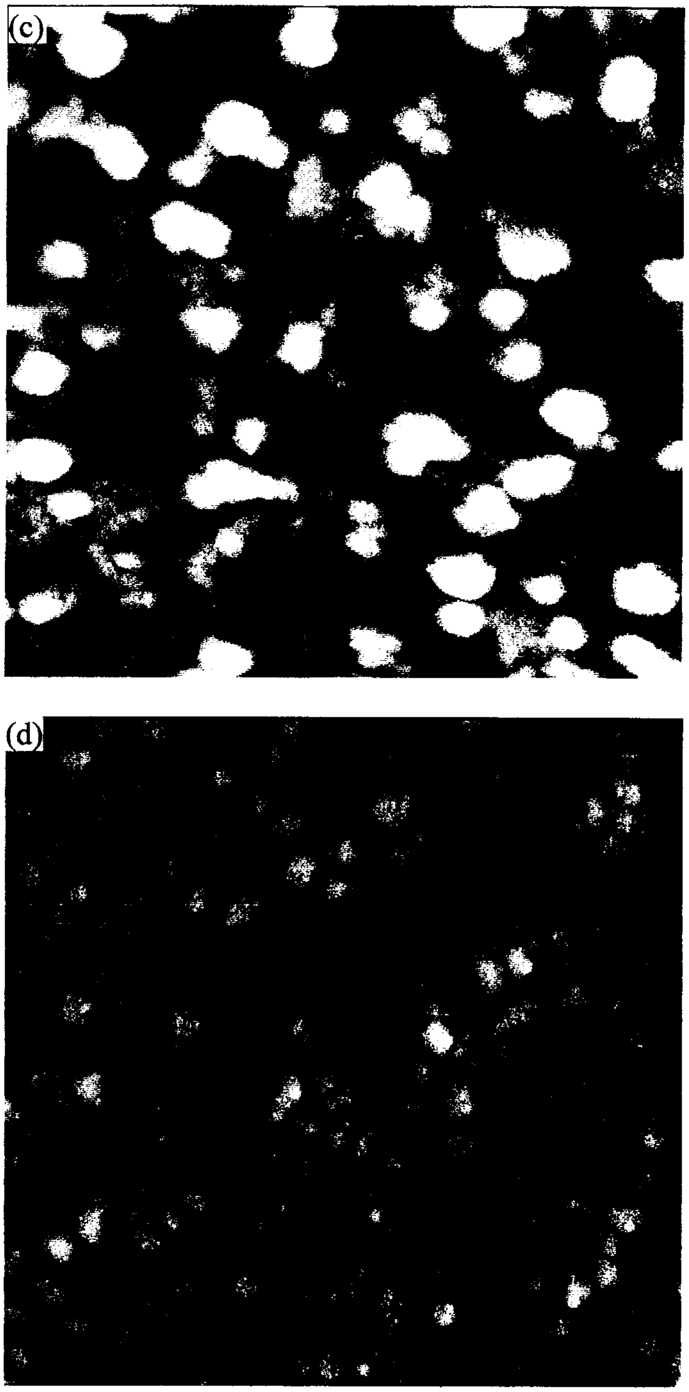

Figure 6-24 (*Continued*)

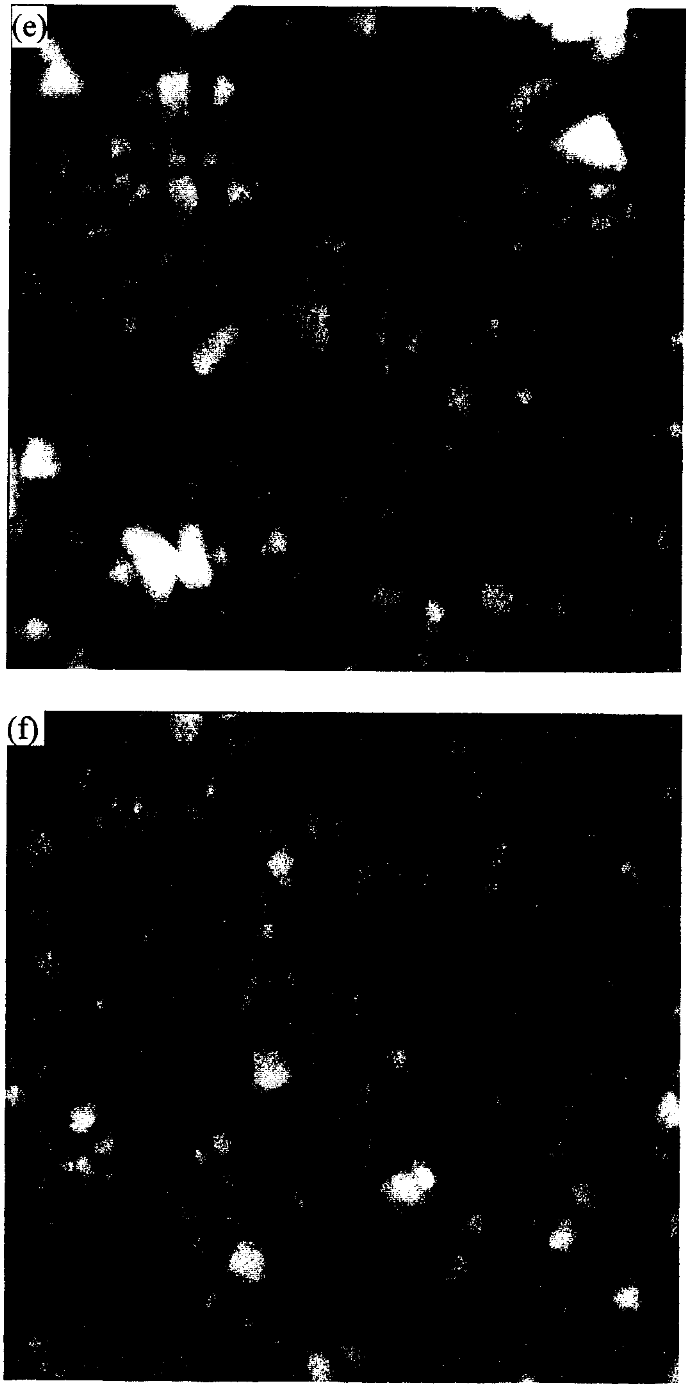

Figure 6-24 (*Continued*)

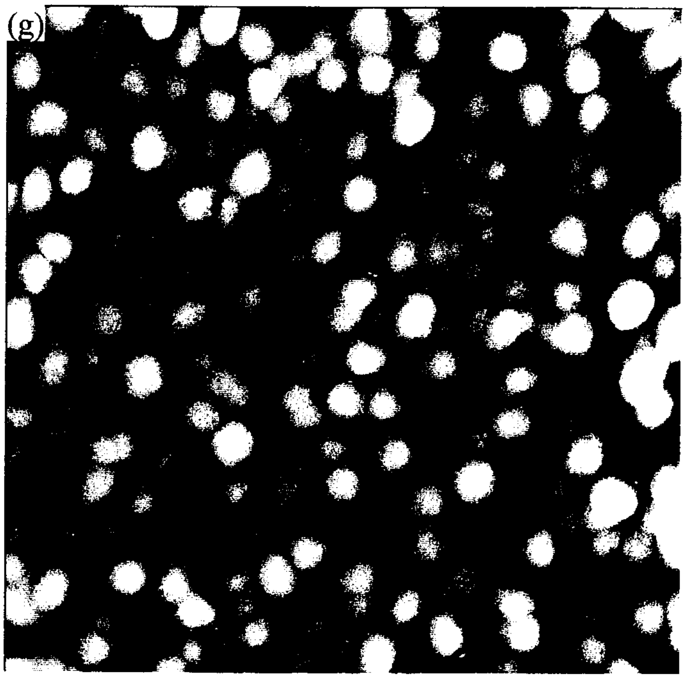

Figure 6-24 (*Continued*)

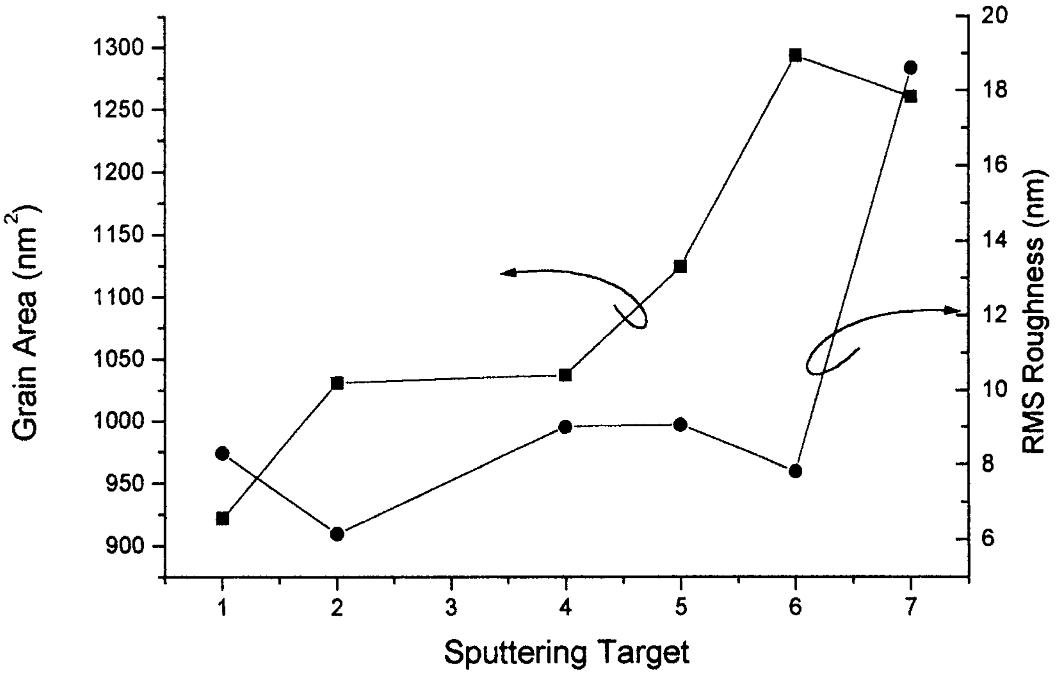

Figure 6-25) Grain area and surface roughness of films as a function of sputtering target. All films were annealed at 900°C for 12 hours.

(black lowest, white highest). All films were annealed in a vacuum furnace with a base pressure of 7.5×10^{-6} torr. The effect of anneal temperature on the films is shown in the AFM images in Figure 6-20, for cadmium processed films from target 4. All the films were annealed in vacuum for 12 hours. Figure 6-21 shows a plot of the grain size and RMS roughness of the films as determined from the AFM images. The grains are on the order of 500-600 nm^2 in size for temperatures up to 800°C. For higher anneal temperatures the grain size grows steadily, reaching a maximum of 1600 nm^2 at 950°C, or roughly 2.5x the size of the grains annealed below 800°C. The surface roughness moves in lock-step with the grain size, which has a significant impact on the optical outcoupling. Since diffusion is a thermally activated process, increased grain growth at higher temperatures is to be expected.

The impact of anneal time on the microstucture is illustrated by the AFM micrographs shown in Figure 6-22. The films were all annealed at 900°C in vacuum for times ranging from 1 hour to 48 hours. Figure 6-23 shows the grain size and surface roughness for these films. As is to be expected, the grain growth is most dramatic for films annealed for very long times. Between 1 hour and 12 hours, the grain size increases from 600 nm^2 to 800 nm^2. RMS roughness also varies slowly over this time scale. The grains are dramatically larger in the films annealed for 24 and 48 hours. Grain growth does not follow the ideal parabolic rate law, however this law does not take into account the constraints on the system due to the thickness of the film and the evolution of the chemical composition (Kingery et al., 1976). Once again the surface roughness follows the same trend with anneal time as the grain size.

Finally, the effect of the cadmium processing on the coarsening behaviour can be seen in the AFM images presented in Figure 6-24. The grain size and surface roughness derived from these images are shown in Figure 6-25. The maximum size of the grains increases steadily as the degree of cadmium processing is increased, more or less levelling off by the films from target 6. The grain size increases from 925 nm^2 for the films from the cadmium free target 1, up to 1250 nm^2 for films from targets 6 and 7, which were subjected to the most aggressive cadmium processing. Interestingly, surface roughness is essentially unchanged for cadmium processed films up to target 6, jumping by a factor of ~2x for the films from target 7. Since all of the cadmium has sublimed from the films while the spinel structure has been maintained (see X-ray diffraction patterns in Figure 6-16) the vacancies resulting from cadmium sublimation are clearly the playing an important role in grain growth.

6.2.2 Luminescence From Thin Films

6.2.2.1 Photoluminescence

As deposited or after an air anneal, the films showed no luminescence. The films were vacuum annealed in order to reduce the manganese to the Mn^{2+} state in order to obtain luminescence. The base pressure during annealing was 1.0x10^{-6} torr. When

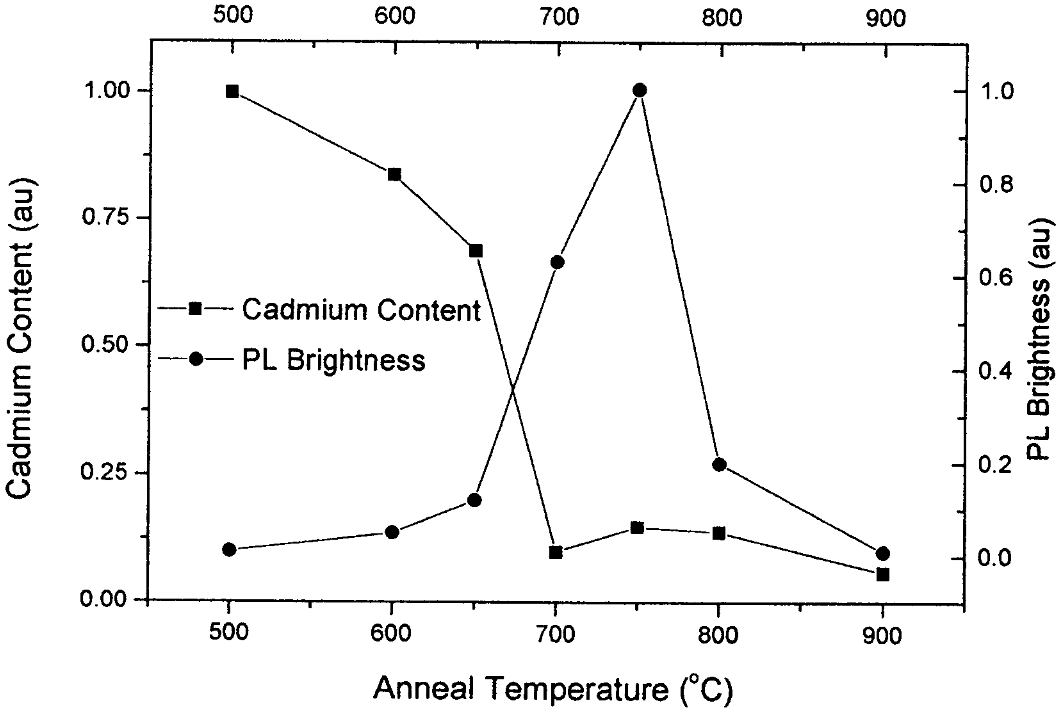

Figure 6-26) Relative PL brightness and cadmium content of films sputtered from target 4 versus annealing temperature.

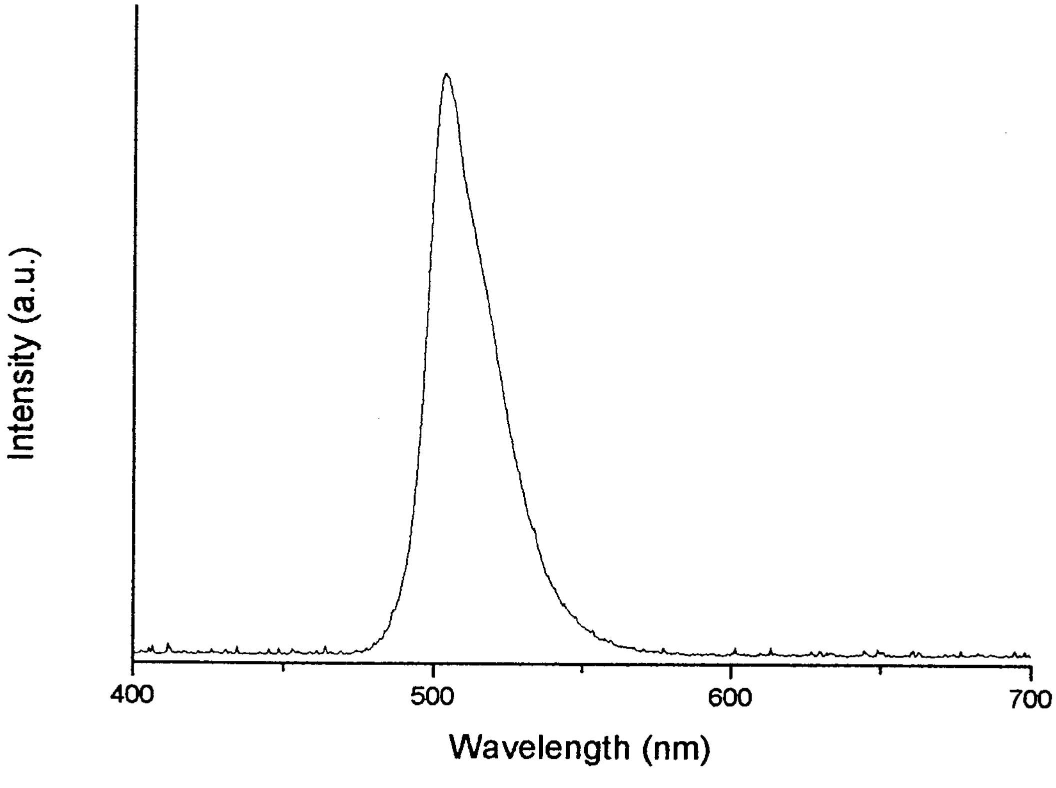

Figure 6-27) EL emission spectrum of a film sputtered from target 1, annealed at 900°C for 12 hours.

excited by 254 nm radiation, the films emitted an identical spectrum to that of the powders, which was shown in Figure 6-2. The emission intensity showed a dramatic dependance on the annealing temperature. This is shown in Figure 6-26 which plots the brightness of the PL versus the annealing temperature. The brightness rises dramatically above 650°C, peaking at 750°C, before dropping off sharply, with almost no PL by 900°C. Also shown in this Figure is the relative amount of cadmium in the films. As can be seen, the peak brightness is associated with the complete loss of cadmium from the films. The loss of cadmium, and its impact on the diffusion and reduction characteristics of the host drives improved Mn^{2+} incorporation and microstructural improvements. The subsequent decrease in PL corresponds to the loss of zinc and the complete structural decomposition of the host, as shown in Figure 6-6.

6.2.2.2 Electroluminescence

The films were deposited to a thickness of 5000 Å ± 500Å. When the devices were excited by the application of an electric voltage, they showed the same green emission as the films and powders excited optically. All films were annealed in a vacuum furnace with a base pressure of 7.5×10^{-6} torr. An EL emission spectrum is shown in Figure 6-27, and is identical to the photoluminescence spectrum. The most significant difference between the various films was the luminance, efficiency and transferred charge under EL excitation. These three parameters are compared for all films by measuring the parameters at 40 V above threshold, the industry standard measure of device performance. Because of the soft turn-on of these devices, the threshold voltage was determined by extending the steepest section of the B-V curve to the voltage axis. There were no trends in threshold voltage with annealing conditions, all lying between 100 V and 150 V, except films annealed for 24 hours or longer. For these films the threshold voltage increased to between 150 V and 200 V. The uncertainty in EL brightness is ±10% for each sample. This level of uncertainty was determined by measuring the variation in peak brightness of 3-4 pixels on each sample, in addition to the B-V measurements from threshold up to the maximum voltage of 600 V_{P-P}. While it was not feasible to examine multiple samples for each set of processing parameters, approximately 1/3 of the samples were repeated (new sputtering run and anneals) in order to gain a grasp of the reproducibility. The data presented represents the average of the measured EL characteristics for these samples, with the uncertainties added in quadrature. Due to the cluttered nature of the EL traces, error bars were not included in the Figures referred to in the following two sections. However, the Figures, with error bars, are shown in the appendix. The performance curves there have been divided between two graphs in order to present the information clearly.

It should be noted that all references to targets and their composition/cadmium content refer to the composition prior to the firing of the targets. Target number refers to the numbers given the targets in Table 6-2.

6.2.2.2.1 The Effect of Anneal Temperature

The luminance at 40 V above threshold for samples annealed at a range of temperatures is shown for samples driven at both 60 Hz and 600 Hz in Figures 6-28 and 6-29 respectively. Except for the cadmium processed films from targets 6 and 7, the EL brightness increases with annealing temperature up to between 875°C and 900°C. All films annealed above 900° showed a decrease in brightness. Devices annealed at 850°C and 950°C are also very close in luminance, but have a maximum luminance of roughly 75% of the brightest films. The highest brightness occurs in films sputtered from target 2, although the difference between the films from targets 1 through 4 is <10% over virtually the entire temperature range. The peak brightness obtained was 50 cd/m^2 at 60 Hz (targets 1 and 2) and 340 cd/m^2 at 600 Hz (targets 2 and 3). These values are roughly 10x that of the films from target 7, which were the most aggressively cadmium processed devices.

The efficiency of these devices at 60 Hz and 600 Hz is shown in Figures 6-30 and 6-31 respectively. At both frequencies the two most obvious features of the Figures is the rise in efficiency with temperature, but also the divergence of efficiency between the films from the various targets. At 750°C, the efficiency of all the devices is clustered below 0.1 lm/W. By 900°C the efficiencies range from less than 0.1 lm/W for the sample from target 7, to 0.5 lm/W at 60 Hz and 0.35 lm/W at 600 Hz in cadmium processed

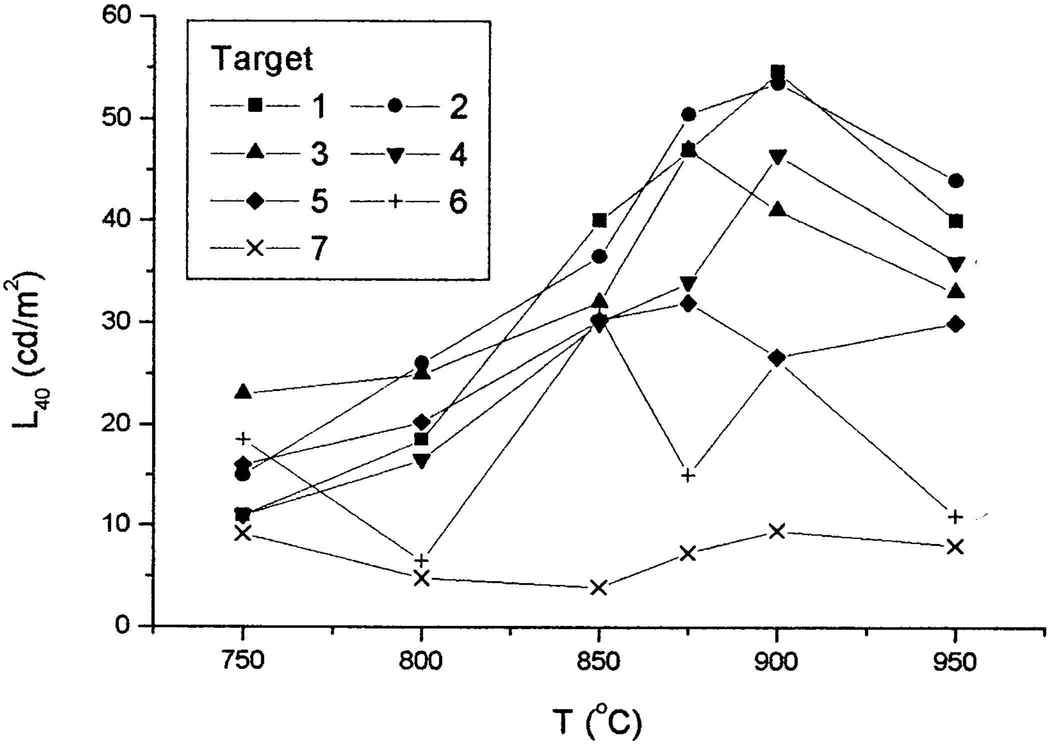

Figure 6-28) EL brightness at 40 V above threshold as a function of anneal temperature for all cadmium contents at 60 Hz. Films were annealed for 12 hours.

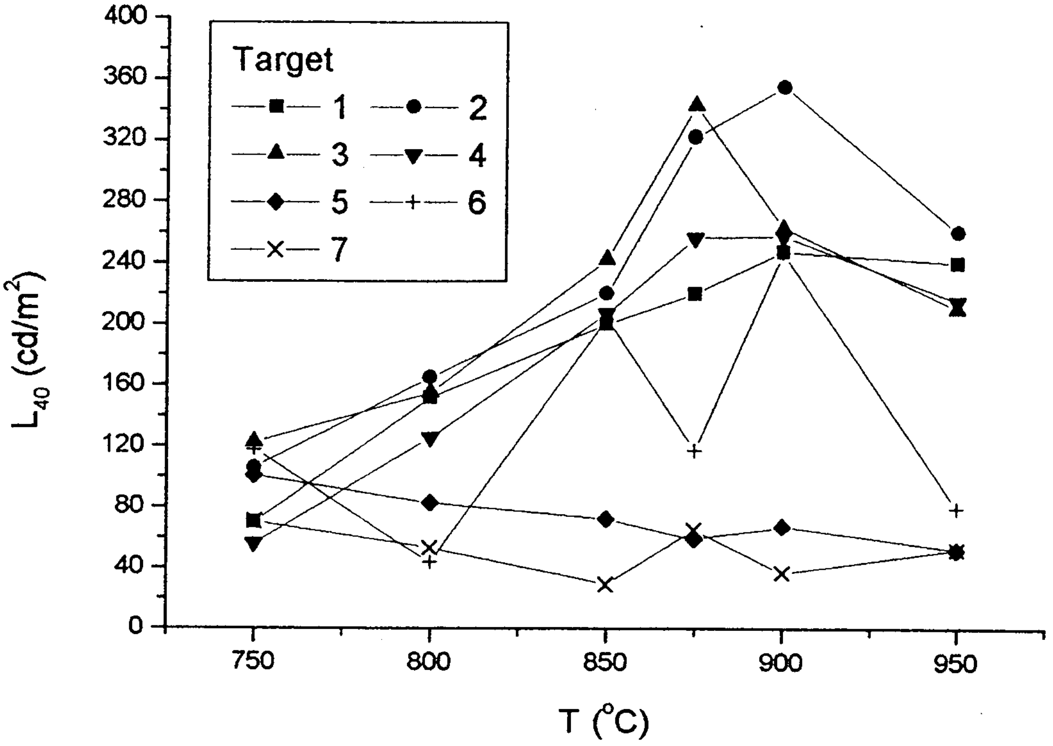

Figure 6-29) EL brightness at 40 V above threshold as a function of anneal temperature for all cadmium contents at 600 Hz. Films were annealed for 12 hours.

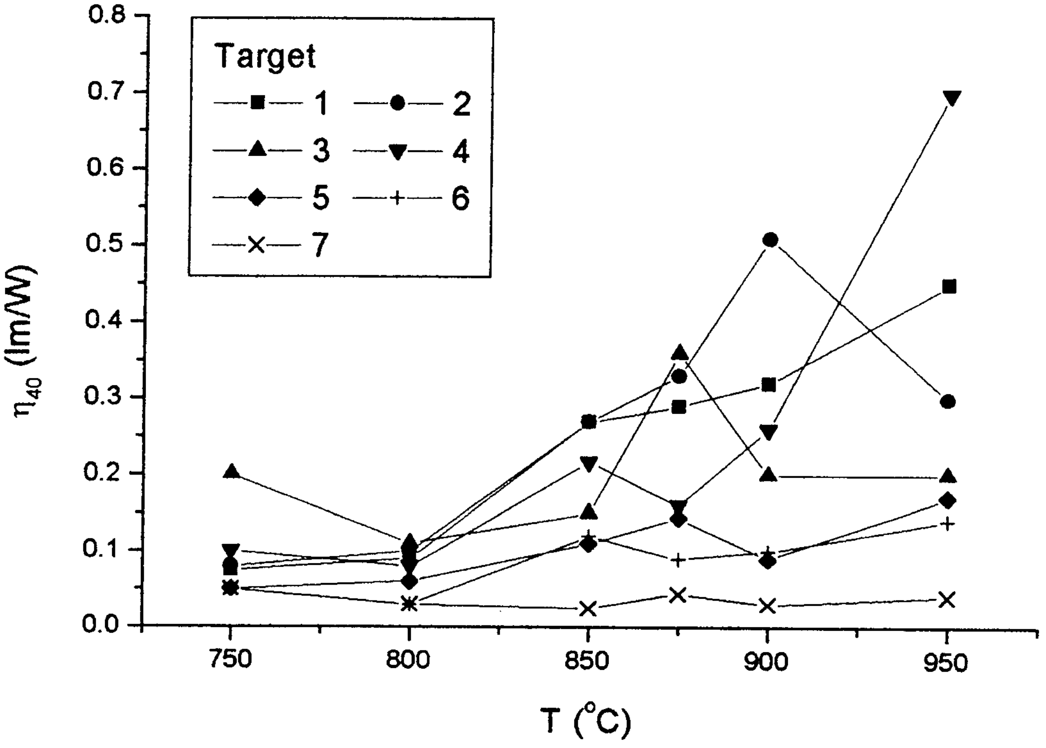

Figure 6-30) EL efficiency at 40 V above threshold as a function of anneal temperature for all cadmium contents at 60 Hz. Films were annealed for 12 hours.

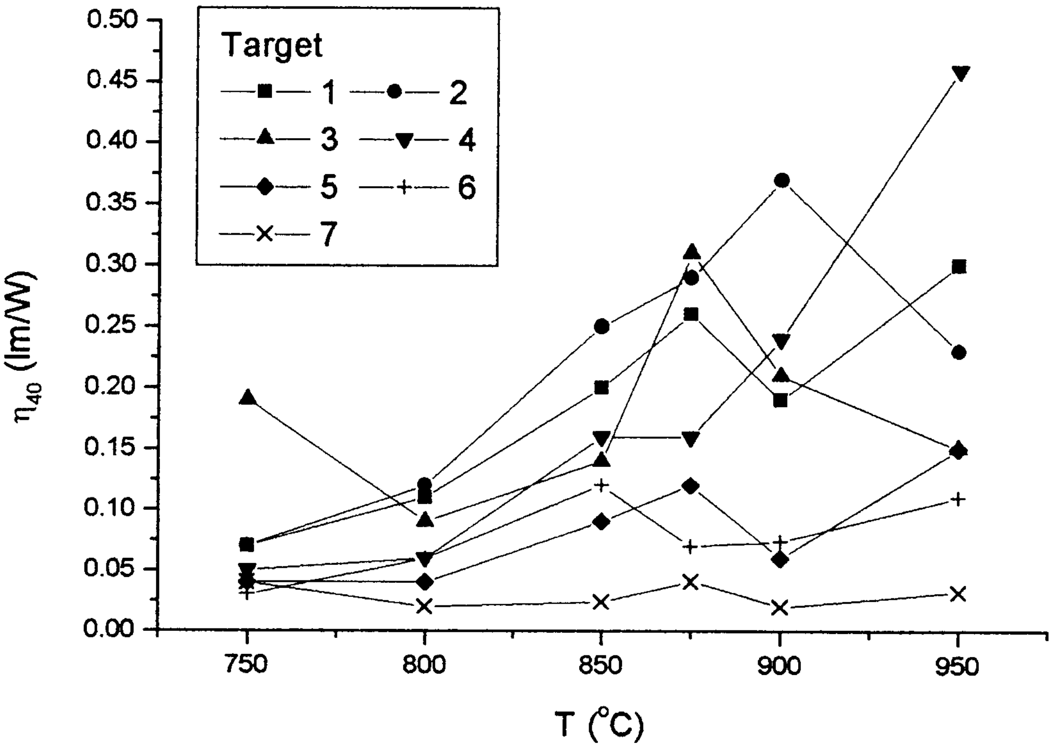

Figure 6-31) EL efficiency at 40 V above threshold as a function of anneal temperature for all cadmium contents at 600 Hz. Films were annealed for 12 hours.

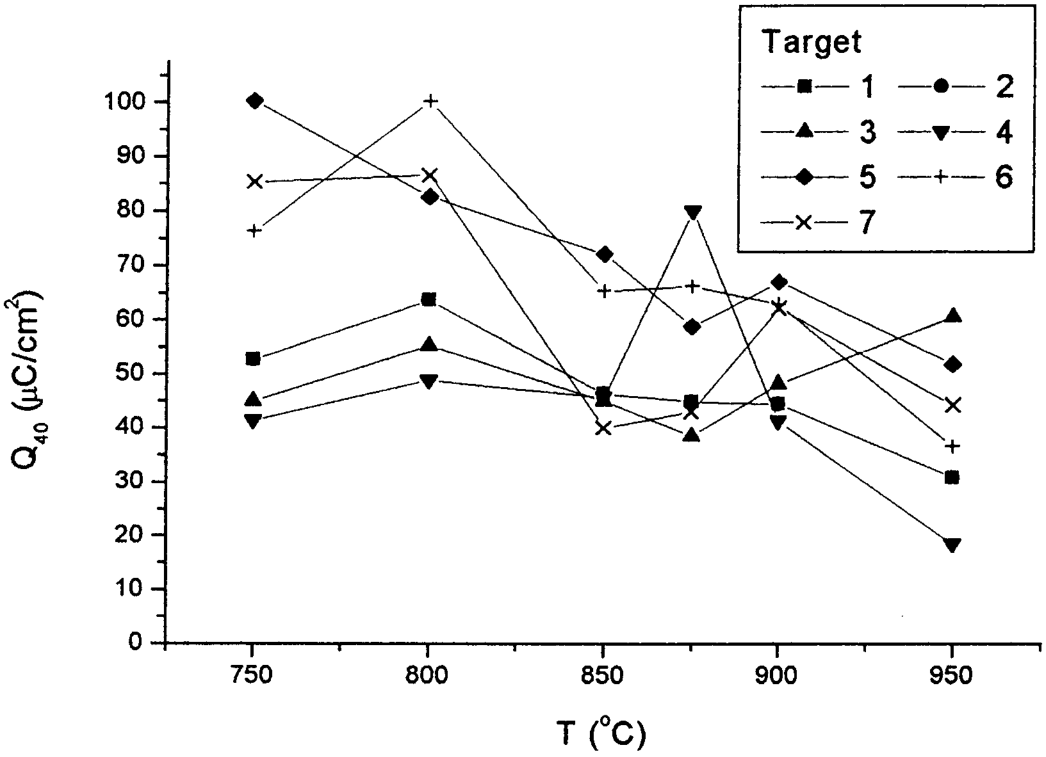

Figure 6-32) Transferred charge at 40 V above threshold as a function of anneal temperature for all cadmium contents at 60 Hz. Films were annealed for 12 hours.

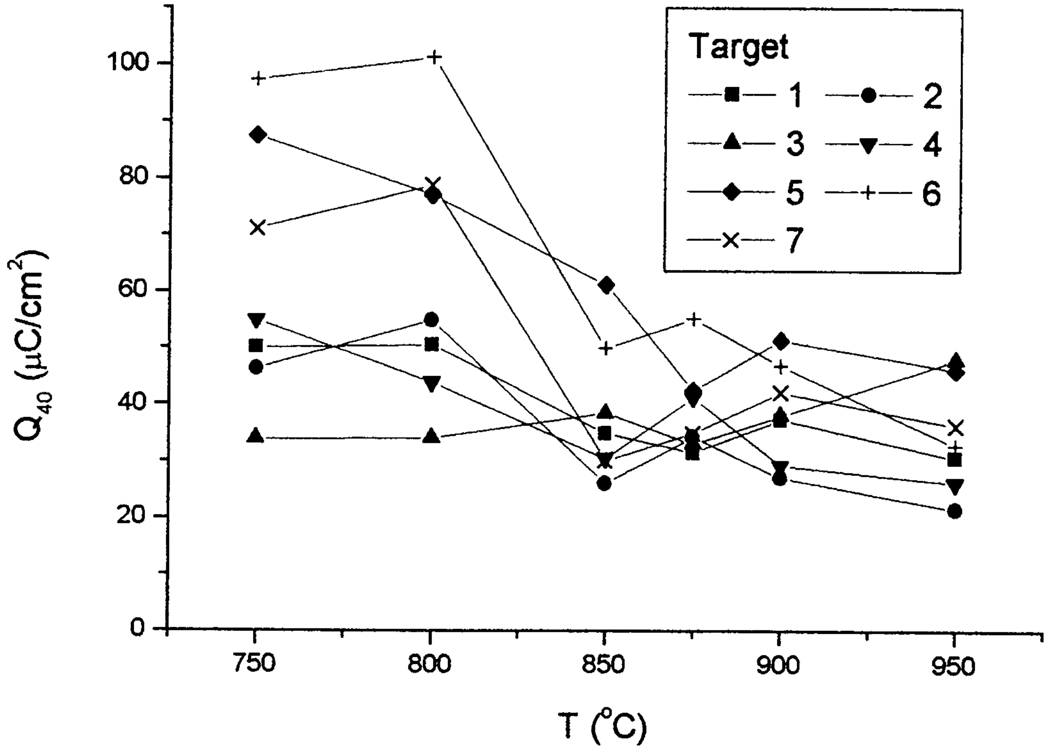

Figure 6-33) Transferred charge at 40 V above threshold as a function of anneal temperature for all cadmium contents at 600 Hz. Films were annealed for 12 hours.

films from target 2. The highest efficiency devices annealed at 900°C were sputtered from target 2. While a decrease or levelling off in efficiency is seen above 900°C for most compositions, the device from target 4 showed an anomalous jump when annealed at 950°C, almost doubling its efficiency. This extremely large change in efficiency suggests the sample was irregular. It should be noted that the efficiency for devices from targets 1 through 4 lie very close to each other at both frequencies, and that the efficiency for these devices roughly doubles between 800°C and 875°C, showing the importance of Mn^{2+} incorporation and microstructural improvements on the performance of the devices. Films from target 7, which were the most aggressively cadmium processed, have an efficiency of ~0.05 lm/W regardless of anneal temperature, suggesting that the concentration of manganese in these devices is quenching the luminescence.

The transferred charge in the devices is shown in Figure 6-32 for devices driven at 60 Hz, and in Figure 6-33 for devices operated at 600 Hz. The overall trend is a steady decrease in charge density as the anneal temperature is increased. In general, the films which were more aggressively cadmium processed had higher initial transferred charge, with films from targets 5,6 and 7 having 1.5-2x the transferred charge of the other 4 films. The other clearly visible trend is toward a reduced spread in the amount of transferred charge with increased anneal temperature. After a 750°C anneal, the transferred charge density ranges from ~30μC/cm^2 for the target 3 sample up to 100 μC/cm^2 for the target 7 sample. The 950°C samples on the other hand are spread between 20 μC/cm^2 for the target 2 sample up to ~50 μC/cm^2 for the target 4 and target 3 samples. Five of the seven samples, including the targets 6 and 7 samples, lie between 20 $\mu C/cm^2$ and 40 $\mu C/cm^2$. Another significant feature is that the transferred charge is roughly 25% higher at 60 Hz than at 600 Hz, except for the two lowest annealing temperatures for which there is no significant difference. This may indicate the slow release of charge from traps in the films which does not occur as appreciably at the higher frequency.

6.2.2.2.2 The Effect of Anneal Time

The luminance at 40 V above threshold peaks for anneals between 6 hours and 12 hours, as can be seen in Figures 6-34 and 6-35 for 60 Hz and 600 Hz, respectively. The peak luminance was achieved in the cadmium processed films from targets 2 to 4 when annealed for 6-12 hours, with films from target 4 being the brightest (55 cd /m^2 at 60 Hz and 440 cd/m^2 at 600 Hz) followed by targets 2 and 3, although all three devices lie within uncertainty of each other. Films from targets processed with larger amounts of cadmium were all significantly duller. Films from target 7 had a peak luminance which was only 20% of that of the brightest devices, and no luminance was visible beyond 12 hours, as was the case for the films from target 6. The brightness increased by a factor of 1.5-2x between the 1 hour and 6 hour anneals for all devices except for those from target 7. The luminance of all devices annealed for more than 12 hours dropped precipitously, due to host lattice chemical decomposition. For all the other films, by 48

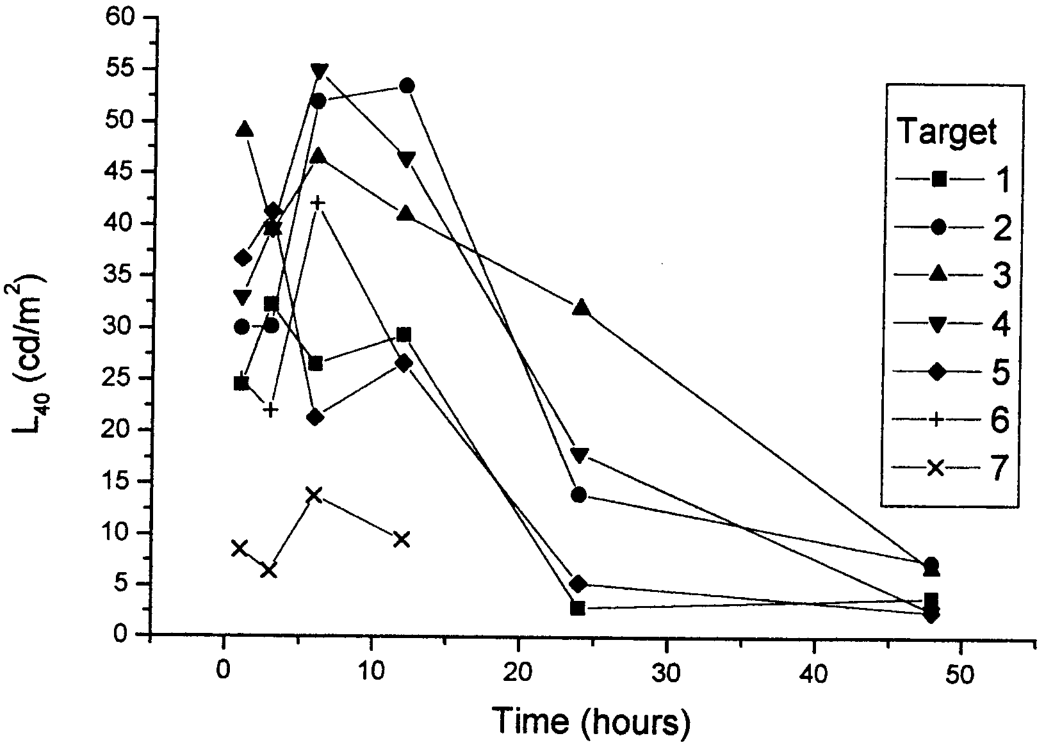

Figure 6-34) EL brightness at 40 V above threshold as a function of anneal time for all cadmium contents at 60 Hz. Films were annealed at 900°C.

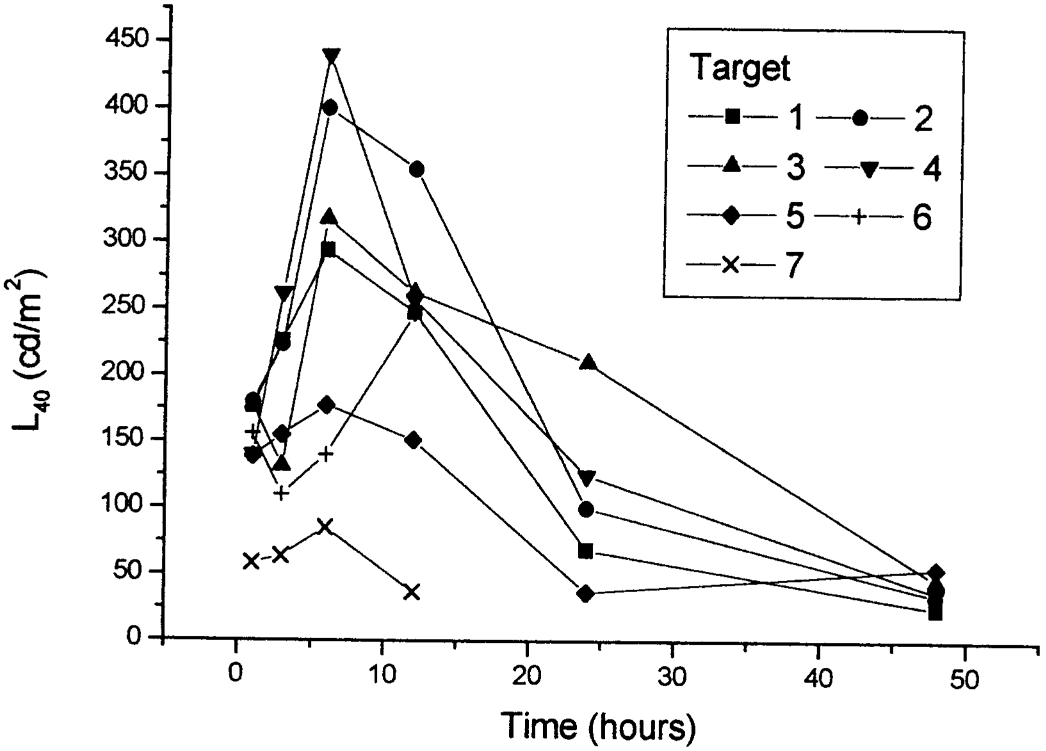

Figure 6-35) EL brightness at 40 V above threshold as a function of anneal time for all cadmium contents at 600 Hz. Films were annealed at 900°C.

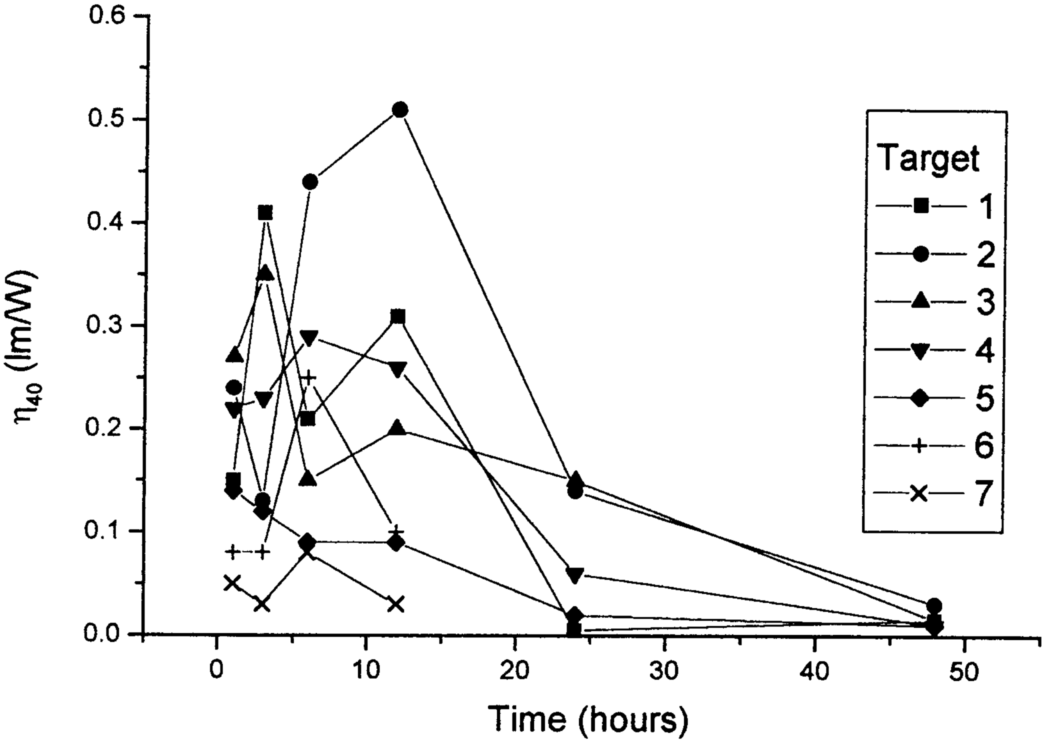

Figure 6-36) EL efficiency at 40 V above threshold as a function of anneal time for all cadmium contents at 60 Hz. Films were annealed at 900°C.

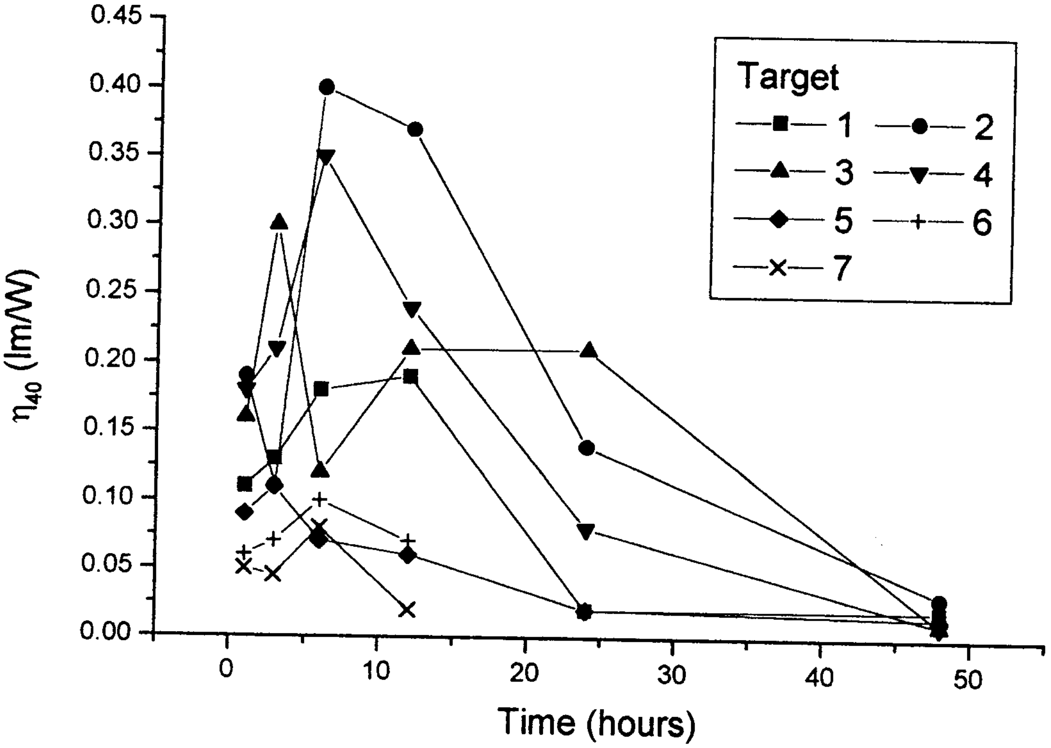

Figure 6-37) EL efficiency at 40 V above threshold as a function of anneal time for all cadmium contents at 600 Hz. Films were annealed at 900°C.

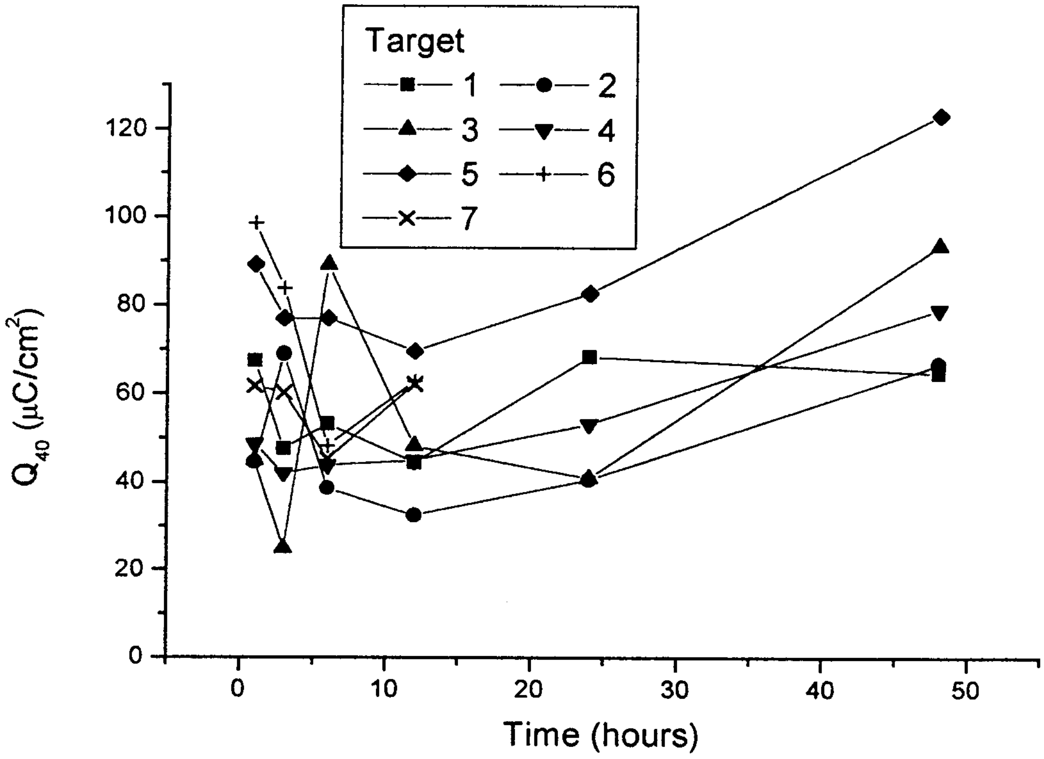

Figure 6-38) Transferred charge at 40 V above threshold as a function of anneal time for all cadmium contents at 60 Hz. Films were annealed at 900°C.

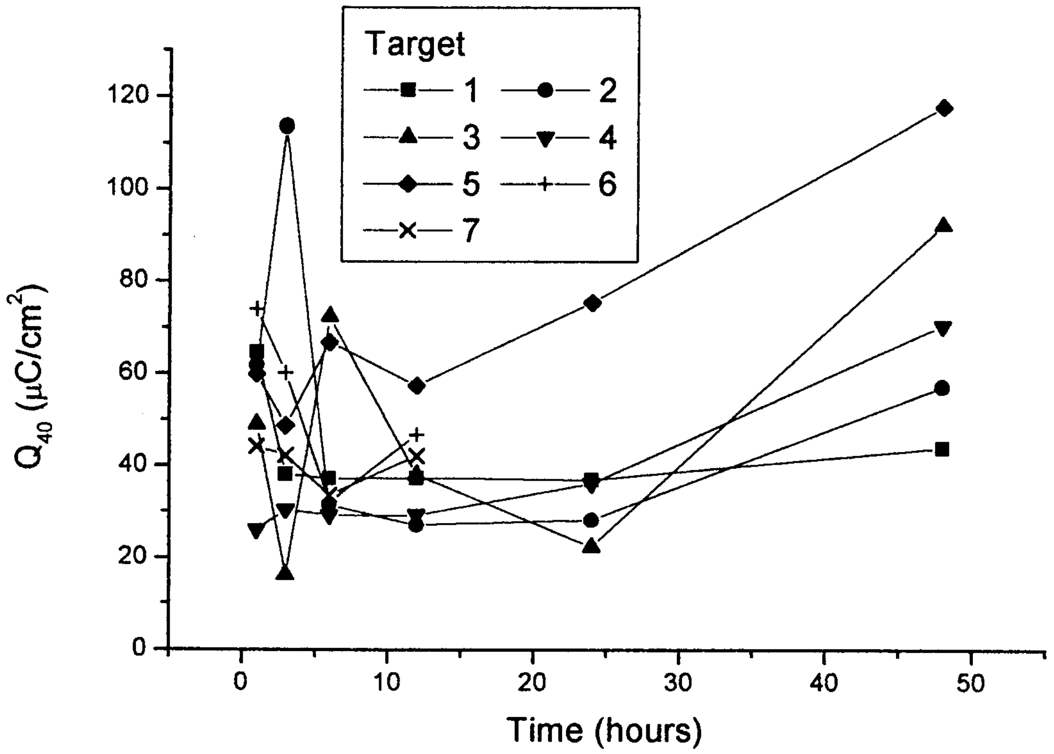

Figure 6-39) Transferred charge at 40 V above threshold as a function of anneal time for all cadmium contents at 600 Hz. Films were annealed at 900°C.

hours the luminance had decrease to ~ ⅓ that of films annealed for 1 hour.

The efficiency traces exhibit a shape similar to that of the luminance curves, peaking after 6 hours. This is shown in Figure 6-36 for 60 Hz measurements and 6-37 for 600 Hz measurements. Like the luminance, the efficiency drops rapidly with anneal time after the peaks. The highest efficiency was obtained for the devices from target 2, annealed for 6 to 12 hours. These devices showed a peak efficiency of approximately 0.5 lm/W at 60 Hz and 0.4 lm/W at 600 Hz. The more aggressively cadmium processed films from targets 5, 6 and 7 were in general always less efficient than the other films, by up to as much as a factor of 10. The peak efficiency at 600 Hz is in general 20% lower than that at 60 Hz, due to the long relaxation time of manganese relative to the drive frequency.

The transferred charge curves have a U-shape when plotted against anneal time, as shown in Figures 6-38 and 6-39 for measurements at 60 Hz and 600 Hz. This is likely due to the elimination of shallow traps and interface states decreasing total transferred charge, followed by a reduction of the host which results in n-type conductivity, which dissipates energy without exciting the dopants. Since long anneal times correspond with the loss of both zinc and cadmium, the remaining material is gallium oxide. The relatively high electron mobility in reduced Ga_2O_3 has led to its investigation as a potential transparent conducting oxide (Ueda et al., 1997). The minimum value of transferred charge for each level of cadmium processing was reached at between 6 and 12 hours. There does not appear to be any trend in transferred charge with the level of cadmium processing until very long anneal times, at which point the amount of transferred charge scales with the degree of cadmium processing, although all points lay within the uncertainty of each other. The lowest transferred charge occurred for the films from target 2 annealed for 12 hours, and was approximately 30 $\mu C/cm^2$ at both frequencies. The films from targets 1, 3 and 4 reached minimum values of transferred charge slightly higher than the target 2 case, roughly 40 $\mu C/cm^2$. Films from targets 6 and 7 showed an increase in transferred charge of roughly 1.5x that of the target 2 devices. The exception is the target 5 devices, which had roughly twice the transferred charge of the target 2 samples.

6.2.2.2.3 EL Decay Time

When the device is driven by an AC voltage, there is a pronounced asymmetry in the light output, as can be seen in Figure 6-40. When a positive bias is applied to the ITO electrode, charge is injected from the phosphor-dielectric interface. These carriers are injected at a higher voltage than when the ITO is biassed negative and charge injection occurs from the phosphor-ITO interface. Because charges originating from the phosphor-dielectric interface have a higher average energy, a larger fraction of these electrons are capable of exciting the luminescent centres, and hence a brighter light pulse is generated during that half of the drive cycle. This effect has been well documented in sulphide phosphors (Mueller, 2000).

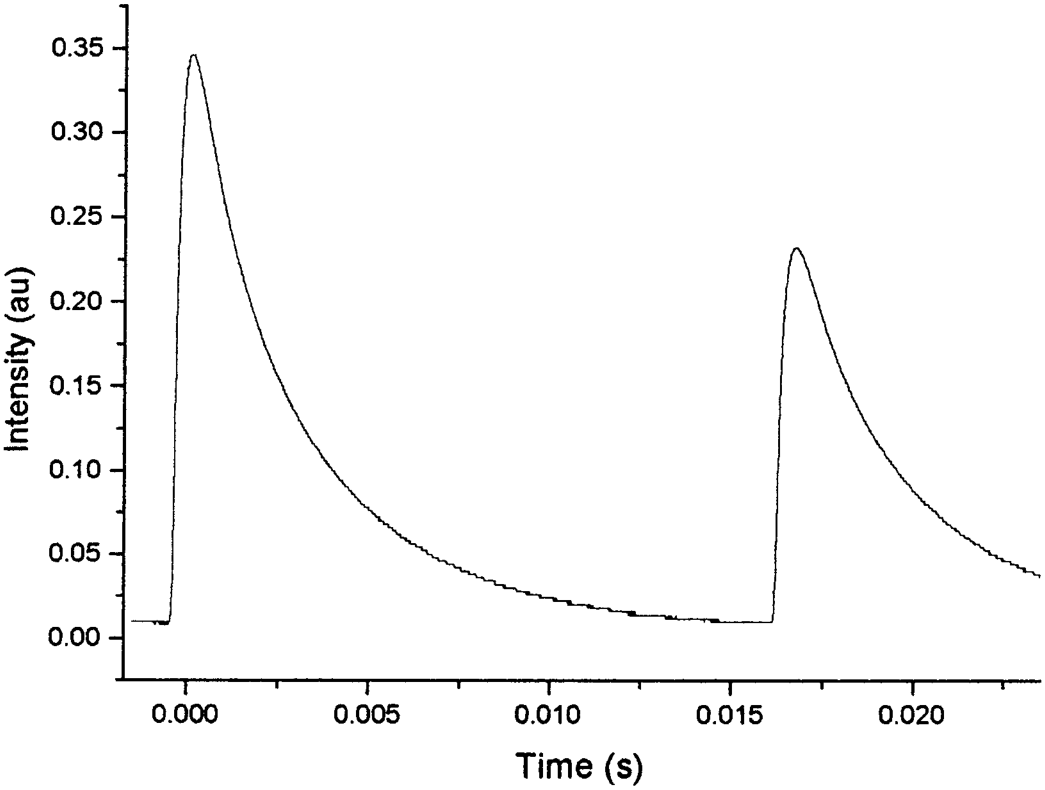

Figure 6-40) EL decay curves for a device from target 4 annealed at 900°C for 12 hours. The smaller peak occurs when charge is injected from the ITO-Phosphor interface.

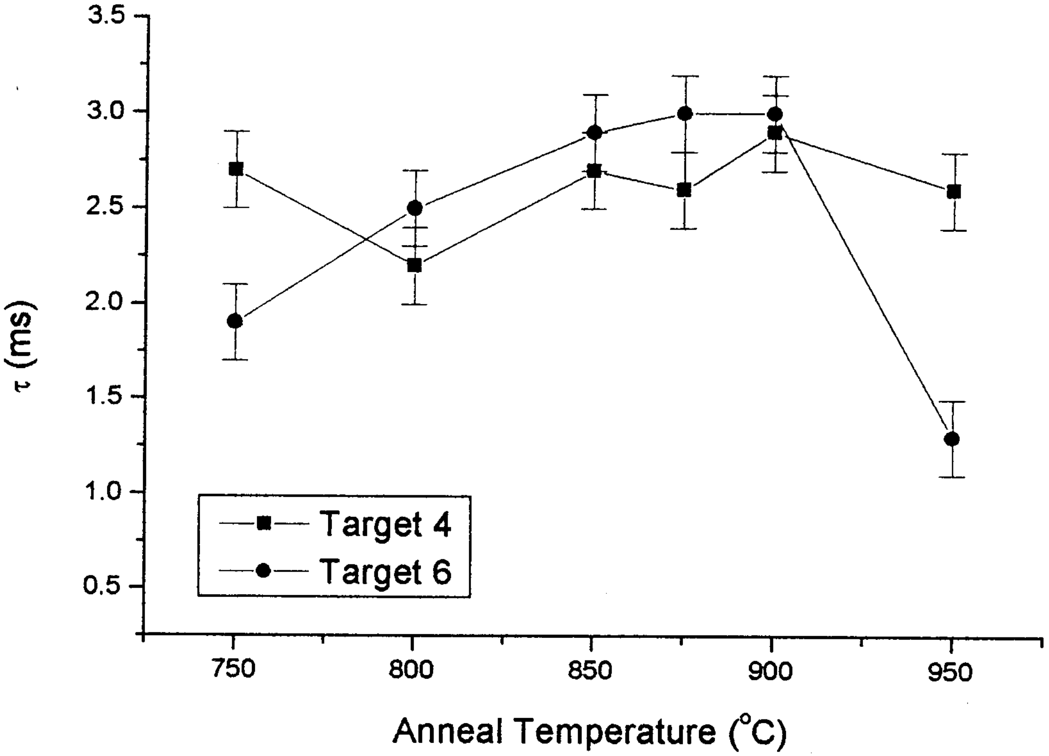

Figure 6-41) Dependence of EL decay time on the anneal temperature of films annealed for 12 hours.

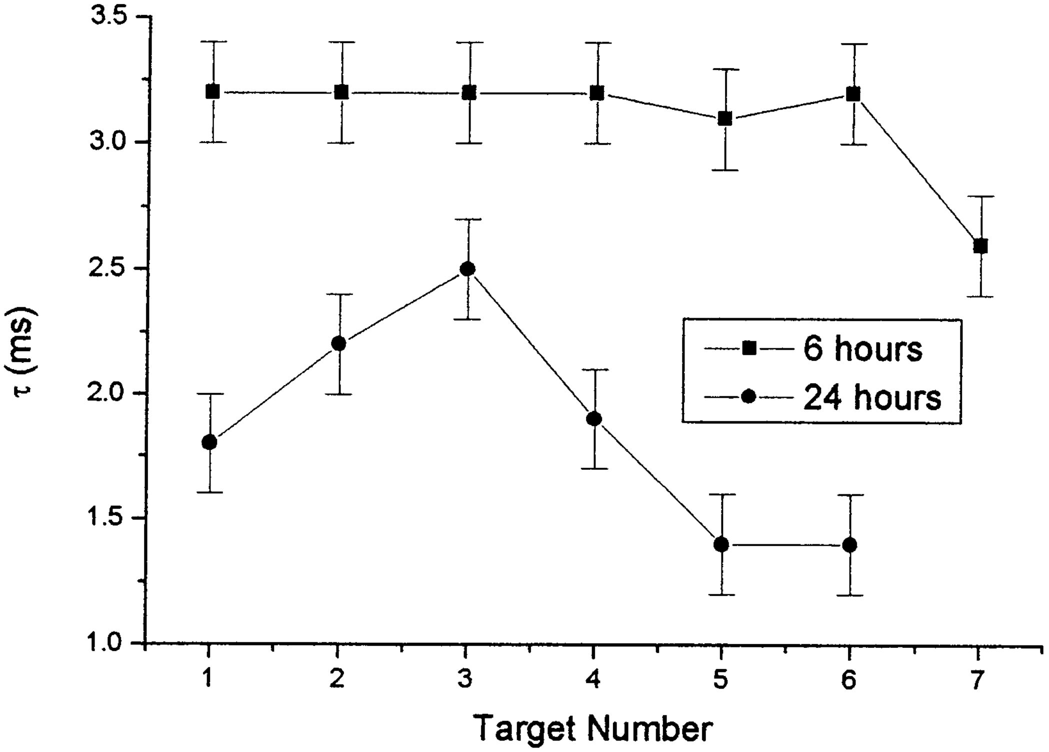

Figure 6-42) Dependence of EL decay time on the sputtering target for films annealed at 900°C for 6 hours and 24 hours.

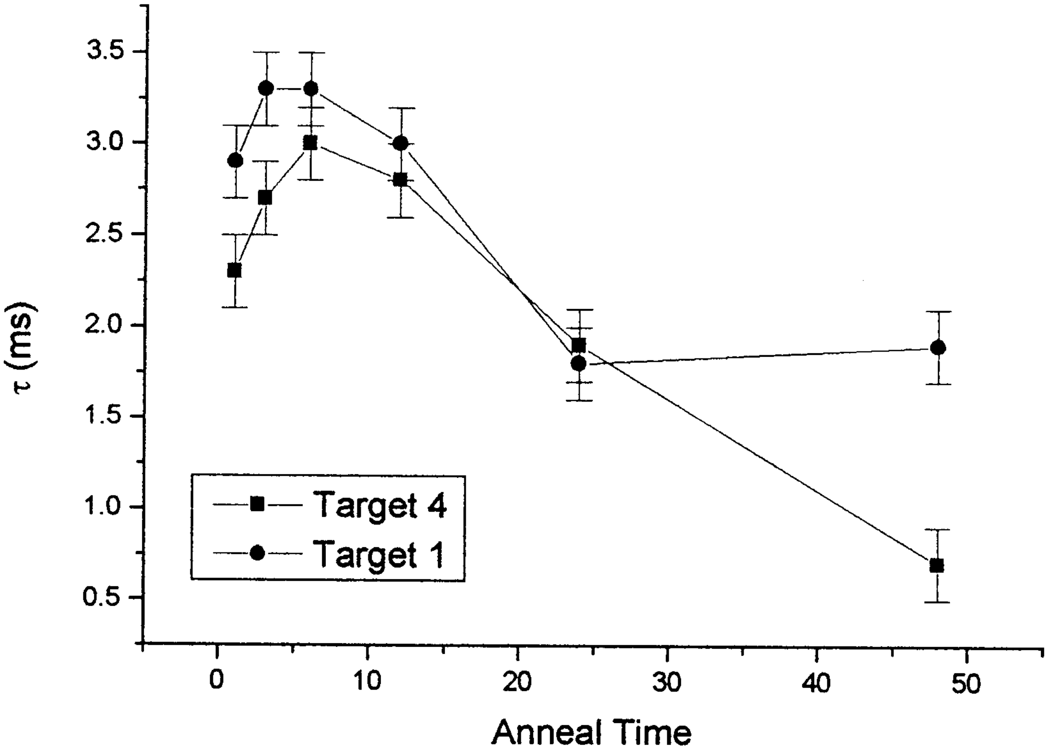

Figure 6-43) Dependence of EL decay time on the anneal time of films annealed at 900°C.

The annealing temperature plays an important role in determining the decay time, as shown in Figure 6-41 for the case of cadmium processed films sputtered from targets 4 and 6. The decay times agree within uncertainty for all temperatures in the case of the films from target 4, however for the target 6 films, there is first a slight rise in decay time as the temperature increases, before a large drop at 950°C. Films from both targets had a maximum decay time of 3.0 ms after a 900°C anneal.

The dependance of decay time on the degree of cadmium processing is shown in Figure 6-42 for films annealed for 6 hours and 24 hours. For the shorter anneal time the variation with cadmium processing is quite small, being essentially constant out to target 6, before dropping only slightly. In the case of films annealed for 24 hours though, the decay time rises from 1.8 ms for films from target 1 to 2.4 ms for films from target 3, and then dropping to 2/3 of the maximum time by the target 6 films.

By far the most pronounced variation in decay time is shown in Figure 6-43. As the annealing time is increased, the decay time also increases, up to the 12 hour anneals, shown in Figure 6-43. The decay time then drops to well below the initial value. Films from target 4 have shorter decay times for all anneal times, reaching a maximum value of 3 ms. By 48 hours, the decay time drops to below 1 ms. The target 1 samples have a maximum decay time of 3.3 ms, and drop to 1.8 ms by 24 hours. The decrease in decay time is due to the quenching of the luminescence in the decomposition products.

It should be noted that although the decay times have been calculated by determining the time for the brightness to decay to 1/e of the peak brightness, the decay cannot be fit with a single exponential. This indicates that there are competing processes through which the excited manganese relaxes to the ground state (most likely the radiative emission process and one or more competing nonradiative decays). Competing relaxation processes result in decays which are described by a power series, not a simple exponential (Imbusch, 1978).

6.3 Discussion

6.3.1 Photoluminescence

The invariance of the powder PL spectrum with respect to cadmium processing of the powder mixture can be rationalized by considering the structure of the spinel material. The manganese substitutes into the tetrahedrally coordinated A-sites within the spinel lattice. Most, if not all of the cadmium which dissolves in the lattice will also occupy the tetrahedral sites. (We can be confident that a significant portion of the cadmium remains, since films sputtered from powders contain cadmium levels close to those of the starting materials.) Because the A-sites are isolated from one another (i.e. no two A-sites share a common oxygen ion(s)) the perturbation of the lattice resulting from the substitution of cadmium for zinc does not alter the nearby A-sites into which the manganese may have substituted, and hence does not affect the emission of the manganese centres. The same argument applies to vacancies on the A sub-lattice or Ga^{3+} which has moved from a B to an

A site. This contradicts earlier published work which showed a small red shift in the manganese emission with the substitution of cadmium for zinc in the starting materials (Kim et al., 1999). This difference can be attributed to the higher processing temperature used in the earlier work (1200°C versus 1000°C used in this study), along with the subsequent aggressive reduction in 5% H_2 : 95% N_2 atmosphere. This would have resulted in much more thermal disordering within the material, which would result in more cadmium, and possibly zinc occupying B-sites which do share a common oxygen with the A-sites into which the manganese substitutes. High firing temperatures have been shown to impact the spectrum of $ZnGa_2O_4$:Mn (Poort et al, 1997), and it is likely that this effect is even more pronounced in the less refractory cadmium containing compounds, which are known to be partially inverse, with approximately 20-25% of the cadmium occupying octahedral sites (Huber, 1969).

While the emission is unaffected by cadmium substitution, the excitation spectra clearly show a change with the degree of cadmium processing, as shown in Figures 6-3 and 6-4. The change in the excitation spectra is visible in the absorption band near 240 nm, which has been attributed to the absorption of excitation energy by the gallate groups within the host (Shea et al., 1994). The data is not sufficient to determine whether the shift is due to a change in the coordination of the gallium ions within the spinel phase or to the chemical decomposition of the spinel, however it is clear that this host lattice absorption is being affected, shifting 3 nm with the initial cadmium oxide content in the pellets going from 0% to 25%, due to the perturbation of the gallate group by the substitution of cadmium for zinc in the starting materials, or by vacancies left by Cd sublimation. Because of the arguments presented above, the emission of the manganese centres is not affected when the energy is transferred from the gallate group to these ions.

The most dramatic effect of cadmium is the sharp increase in PL brightness from cadmium free powders compared to those processed with just 5% of the Zn substituted by Cd in the starting materials, as shown in Figure 6-5. The cadmium processing affects the ease with which manganese can be reduced, since powders processed with just 5% cadmium showed no observable Mn^{3+} (i.e the powders had a completely white body colour, as compared to the pinkish colour of the pellet 1 $ZnGa_2O_4$:Mn sample). This eliminates the need for a two stage firing process in which the binaries are first reacted to form the spinel followed by a reduction of the manganese, which has been used by other researchers (Shea et al., 1994; Poort et al., 1997). It should be pointed out that unlike the films, not all of the cadmium is lost when firing the powders, since films sputtered from these materials contain cadmium at or near the relative concentration in the starting materials used to form the targets. This suggests that most of the cadmium is not lost when the binaries are reacted to form the pellets and targets, however the presence of Ga_2O_3 in the powder diffraction patterns, Figure 6-1 clearly indicates the loss of some of the Cd. The effective incorporation of the manganese is obviously strongly influenced by cadmium sublimation. This can be attributed to the large vacancy concentration which results from the loss of Cd, which enhances diffusion in the host . This enhanced diffusion leads to microstructural improvements during annealing which result in improved luminescence.

Beyond the 15% CdO processed powder mixtures, the decrease in luminescent intensity is the result of the loss of cadmium from the material during firing under vacuum conditions. This quenches the luminescence in two possible ways. One is that the manganese becomes concentrated in the spinel phase, leading to concentration quenching. The other mechanism is that a fraction of the manganese is incorporated either into the excess Ga_2O_3 or into some other phase in which the absorption bands overlap with the emission from the spinel phase, resulting in the absorption of spinel phase Mn^{2+} emissions, and the subsequent re-emission of this material at wavelengths outside of the visible spectrum. The lack of luminescence from $CdGa_2O_4$:Mn may also be a factor contributing to the reduced luminescence of the powder material. There is certainly a significant amount of cadmium incorporated in the powders, since powders used to form targets resulted in films with cadmium contents at or above those of the initial, unfired powders, as shown in Table 6-3. The complete lack of luminescence from $CdGa_2O_4$:Mn may be due to the incorporation of Mn^{2+} in both tetrahedral and octahedral sites, with the octahedral manganese quenching any luminescence from the tetrahedral ions, however further study would be needed to confirm this. The substitution of some zinc by cadmium in the spinel powders may result in the incorporation of manganese in undesirable environments, which detrimentally affects the luminescence.

In the case of the thin films, the peak brightness occurs after all of the cadmium has sublimed, as indicated by the EDX and PL data for sputtered films shown in Figure 6-26. This data shows that the activation of manganese occurs synchronously with the loss of **all** the cadmium, indicating that vacancies caused by cadmium substitution and subsequent loss play an important role in the incorporation of manganese in its luminescent 2+ oxidation state. The loss of cadmium sets an upper limit on the maximum vacancy concentration Subsequent zinc loss and decomposition of the spinel structure results in a decrease in PL brightness, for the same reasons as was mentioned above for the powders.

6.3.2 Electroluminescence

The explanation of trends observed in the electroluminescent behaviour is more complicated relative to the photoluminescence since these phenomena depend not just on the phosphor, but also on the EL device structure and materials. Because the excitation of the phosphor is dependent on the structure and characteristics of the EL device, these parameters must be taken into account when explaining the observations.

Like in the case of PL from thin films, post deposition annealing is necessary in order to obtain any luminescence from the EL devices. However, in this case the annealing does not just activate the manganese ions within the film, it also impacts the charge injection and transport properties of the films, as illustrated by the transferred charge in Figures 632 and 6-33 which drops dramatically as a function of anneal temperature, while the EL brightness actually increases up to ~900°C before decreasing, as shown in Figures 6-28 and 6-29. This suggests that as deposited the films contain shallow interface states and defects which release charge below the threshold for manganese excitation, thus consuming energy without contributing to the luminescence.

Changes in the structure of the films are quite obvious from the X-ray diffraction patterns of the cadmium free films from target 1, shown in Figure 6-11. The decrease in the intensity of the (1 1 1) reflection with both increasing temperature and time indicates that the films are undergoing non-preferential grain growth, with the end result that the films have a more random distribution of grain orientations. The films from the cadmium processed targets 2 through 7 show no such texture, as illustrated in Figures 6-15 and 6-16, which indicates that there is no preferred orientation for nucleation and growth in these films. The cadmium clearly acts to promote a more random orientation of nuclei on the substrate during deposition. This implies that this atom is more mobile on the surface, and can more easily move around to find low energy sites to nucleate and grow new grains during deposition.

Grain growth can be followed in the AFM micrographs. Analysis of these images show that the morphology of the films is quite strongly affected by both the annealing conditions and the composition of the films as deposited. Grain growth kinetics depend exponentially on temperature, with an activation energy close to that required for grain boundary diffusion (Kingery, et al., 1976). For this reason, the most substantial grain growth is seen in Figures 6-21 and 6-23 at very long times or higher temperatures. The films remain very fine grained however, since the annealing temperatures used are quite low relative to the melting point of the material. The role of cadmium in the as deposited films is illustrated in Figure 6-25. The grain size in the annealed films increases as the degree of cadmium processing increases. Since it is known that all the Cd is lost during annealing, this data supports the assertion that the vacancies left by Cd sublimation enhance the diffusion kinetics. The Cd content of the films as deposited sets the upper limit on the vacancy concentration after annealing (assuming the structure is maintained and there is no phase separation), while the zinc content sets the Zn:Ga ratio in the films. Diffusion coefficients have been shown to increase linearly with vacancy concentration (Flynn, 1972). It is clear from the XRD data that despite the loss of stoichiometry the spinel structure is maintained.

The decrease in the intensity of the spinel XRD reflections is due to changes in the composition and structure of the film with annealing. It has been determined that above 600°C in reducing atmospheres $ZnGa_2O_4$ is unstable (Beauger et al., 2000). Even in air, $CdGa_2O_4$ is unstable at elevated temperatures, resulting in cadmium sublimation. The spinel structure however remains stable, with the excess Ga_2O_3 dissolved in solution (Datta and Roy, 1968). The EDX spectra clearly show loss of both cadmium and zinc when the films are annealed. Although the solubility of Ga_2O_3 in $Cd_xZn_{1-x}Ga_2O_4$ has not been investigated, it is obvious from the X-ray patterns in Figure 6-13 and 6-14 that the spinel structure begins to break down beyond about 12 hours; under the specific conditions used to anneal films for PL the decomposition began at temperatures above 600°C. Since no lines corresponding to Ga_2O_3 appear in the diffraction pattern, and this component has a low vapour pressure, this material must be amorphous or very fine grained when formed by the decomposition of the spinel.

The effect of cadmium processing and structure on the luminescent characteristics is also quite evident. Optimum brightness was obtained for films annealed between six and twelve hours at 900°C, as shown in Figure 6-34. These films were sputtered from targets 2 through 4, in which cadmium processing involved between 5% and 15% of the ZnO substituted by CdO in the initial powder mixtures. This is identical to the trend seen in the PL brightness of the powders, indicating that it is the loss of cadmium which is improving the microstructure and Mn^{2+} incorporation, leading to the improved EL luminance. The improved Mn^{2+} incorporation after a 6 hour anneal is also illustrated in Figure 6-43, in which the maximum EL decay time is shown to occur after 6 hours at 900°C for two different compositions. The Cd sublimation results in a large vacancy concentration which enhances diffusion rates, thereby accelerating the microstructural improvements during annealing. The intensity of the manganese emissions in the PL films peaked at a lower temperature due to the lower oxygen partial pressure during the annealing of these films, which resulted in reduction of the manganese at lower temperatures. The dramatic improvements in EL performance are seen at temperatures and times before the dramatic increases in grain size (an increase in grain size by 25% over the 1 hour annealed films), indicating that the improved EL performance is due principally to the effect of annealing on point defects and interfaces, although the importance of reduced grain boundary area can not be ignored. The drop in EL luminance with higher cadmium content can be attributed to the decomposition of the spinel, due first to the loss of all the cadmium followed by the loss of the zinc. The nonstoichiometry leads to phase separation and the subsequent incorporation of manganese within the resultant phases, which quenches the luminescence. It could also be due to the concentration of Mn in the spinel material, leading to concentration quenching. This is supported by the EL decay time data shown in Figure 6-41. For the case of films from target 6, which due to their high initial cadmium content would suffer the most from decomposition, the decay drops dramatically at high annealing temperatures. This indicates that a non-radiative relaxation process is competing with the radiative emission, thus reducing the average decay time. The increased transferred charge at long anneal times also reduces efficiency by dissipating energy without exciting manganese dopants.

It should be noted that no effort was made to optimize the dopant concentration. Previous work on $ZnGa_2O_4$:Mn in TFEL devices put the optimum manganese level at 2% of the zinc (Minami et al., 1995) in contrast to an optimum manganese content of 0.6% in powder samples prepared for PL (Shea et al., 1994). The higher manganese content needed in EL devices is due to the requirement that the device itself supply the excitation energy and the electron impact cross-section of the manganese ions within the host. Loss of cadmium and decomposition acts to concentrate the manganese within the spinel, which reduces the luminescent efficiency. A sharp decrease in luminescent efficiency in $ZnGa_2O_4$:Mn with high Mn content has been attributed to the formation of Mn^{2+}-Mn^{2+} pairs (Endo et al., 1996).

While direct comparisons with other research are not possible, all brightness results are within a factor of 2-3x previously reported work. The efficiency on the other hand shows just the opposite trend, being substantially lower than the efficiencies reported for $ZnGa_2O_4$:Mn (Minami, 1998). The power dissipated during each EL cycle is proportional to the transferred charge. In these devices, the amount of charge driven across the devices is one to two orders of magnitude larger than that seen in the $ZnGa_2O_4$ devices reported in the literature. Annealing results first in a reduction of the transferred charge due to improved crystallization of the host, eliminating defects and interface states that inject charges below the threshold voltage for luminescence. This applies to all temperatures, and annealing times below 12 hours as shown in Figures 6-38 and 6-39. While the transferred charge is reduced, the brightness of the films actually increases, meaning that the electron energy distribution during the breakdown lines up more favourably with the electron impact cross-section of the manganese ions, and hence more of the excitation energy is actually converted to light, rather than being dissipated as heat. When longer anneal times are used, the amount of transferred charge rises substantially. This is the result of the reduction of both the host material as well as phases resulting from the decomposition of the host. The resistivity of Ga_2O_3, ZnO:Al, $ZnGa_2O_4$ and $ZnGa_2O_4$:Mn decreases by between three to six orders of magnitude when fired in a reducing atmosphere (Bondar, 2000). This results in a substantial increase in the amount of charge moving at applied voltages below the threshold for luminescence, and hence the power dissipated by the devices rises sharply with no commensurate increase in luminance. The pitted morphology may also have an impact, as discussed below.

The efficiency and transferred charge as a function of the level of cadmium processing exhibit mirror behaviours with respect to anneal time. While the transferred charge decrease is initially followed by a large increase, the efficiency rises, reaching a maximum at the same point the transferred charge is at its minimum, before decreasing again, as shown in Figures 6-36 and 6-37 for the efficiency and 6-38 and 6-39 for the transferred charge. The brightness curves in Figures 6-34 and 6-35 are similar in shape to those of the efficiency. These trends support the assertion that the phosphor decomposition is the cause of the reduced performance at long anneal times.

Unfortunately, the EL data is difficult to interpret due to the scatter in the measured points. The assertion that the optimum cadmium processing level lies between 5% CdO and 15% CdO is however strongly supported by the bulk of the data. It should be noted that the EL data is in sharp contrast to the PL data which is both well behaved and reproducible. This would seem to indicate that the complications with the EL data lie in two possible causes. One is the variability in the EL performance of a sample for any given set of annealing conditions. This uncertainty was reduced by careful sample preparation. The fresh targets were sputtered for 4 hours in order to establish the modified surface necessary for good composition control. Also, the high oxygen partial pressure and low substrate temperature used during deposition limited the loss of the more volatile components. At the EL testing stage, samples which did not have uniform maximum EL brightness across the entire substrate were discarded and new samples prepared. The second is the impact of the substrate used on the device performance. Reaction and interdiffusion with the substrate are possible. The more likely problem however is the pitted morphology of the devices, as discussed below.

It is difficult to say what effect the pitted morphology of the films has on the EL performance. These regions of the film could certainly display undesirable electrical properties, possibly being conduction pathways which become active at low voltages, adding to the transferred charge, but not the luminescence. It is also not possible to say what the average pit size and density is for each pixel examined, which may also explain the scatter in the observed EL trends. The impact of the substrates on the relative device performance was minimized by depositing all of the films on substrates from the same tape casting, thus limiting any variation induced by the ceramic substrates. The degree to which the porosity of the substrates impacts the performance could be evaluated by using higher density $BaTiO_3$ substrates, or substrates which have been treated to eliminate the effect of porosity on the films.

The device performance could also be improved by depositing a dielectric layer between the ITO and the phosphor, since this would improve the charge injection characteristics when the carriers are supplied by the ITO side of the device.

6.3.3 Summary

Powders show a pronounced variation in photoluminescent brightness with cadmium processing level, peaking in materials with 10% of the zinc substituted by cadmium in the starting mixture. The emission spectrum is unchanged however, peaking at 504 nm with colour coordinates x=0.08 and y=0.69. The invariance of the emission with respect to cadmium processing can be rationalized through a consideration of the spinel crystal structure. The dependence of the brightness on the cadmium processing of the as deposited films is due to the improved crystallization which occurs when cadmium is substituted for zinc. Cadmium sublimation resulted in a large vacancy concentration, which in turn increased diffusion rates. The enhanced diffusion results in microstructural improvements which, in turn, lead to higher luminance and lower transferred charge. However, at high cadmium processing levels, the volatility of cadmium results in substantial excess Ga_2O_3 in the powders, which when containing manganese is non-luminescent, and hence partially quenches the luminescence. It is also possible that the manganese segregates to the spinel phase and concentration quenching deceases the luminescence.

Films exhibited the spinel structure, with cadmium free films having a significantly enhanced (111) peak, indicating some texture. As the films were annealed at progressively higher temperatures or longer times, the distribution of grain orientations shifted towards the random orientation of the powder standard. Films with any cadmium processing displayed this random orientation as deposited, even for as little as 5% cadmium substituted for zinc in the unfired sputtering target. The morphology of the films was strongly affected by the substrates. The films had a pitted morphology due to the porous substrates used.

Annealing of thin films resulted in the sublimation of Cd and a partial decomposition of the spinel, and the partial loss of Zn in some cases. The excess gallium oxide is either amorphous, or the grains so fine that they do not appear in the X-ray diffraction patterns. The decomposition of the spinel however results in a steady decrease in the intensity of the diffraction lines for the spinel phase.

Optimum EL performance was obtained in films sputtered from targets processed with 5% to 15% cadmium oxide in the starting materials which were annealed at 900°C for 6 to 12 hours. This was a higher temperature than that which gave the highest brightness in films studied by PL due to the higher oxygen partial pressure during the EL anneals. Improvements in the EL performance are due to the improved crystallization of the host which reduced defect and trapping states which supplied current below the threshold voltage for excitation of the luminescent centre, as well as improved incorporation of the Mn^{2+}. Beyond 12 hour anneals though, the loss of stoichiometry resulted in the spinel and/or the decomposition products becoming reduced and electrically conductive, producing a dramatic increase in the transferred charge and a resultant decrease in luminescent efficiency. Luminance also decreased substantially for anneals over 12 hours.

A sharp drop in luminescent decay time for films annealed over 12 hours indicates the presence of manganese in a non-luminescent form. At these long anneal times, not only had all the Cd sublimed, but large amounts of Zn were also lost. The resultant Ga_2O_3 rich material did not exhibit any luminescence, indicating that either the manganese had concentrated in the remaining material leading to concentration quenching, or it had phase separated into a non-luminescent phase.

Chapter 7

Conclusions and Future Work

7.1 Introduction

A modified processing scheme has been developed in order to fabricate zinc gallate based TFEL phosphors. By introducing a large vacancy concentration via the sublimation of cadmium from the host, the processing temperature required for bright and efficient operation is reduced. Powders produced in this manner are significantly brighter after a single vacuum firing, eliminating the need for a second firing in a reducing atmosphere.

7.2 Conclusions

When $(CdO)_x:(ZnO)_{1-x}:Ga_2O_3:Mn$ powders were reacted at high temperature in vacuum, with $0<x<0.5$, all compositions exhibited the spinel structure, with only the $x \geq 0.2$ phosphors showing enough loss of the group II element for excess Ga_2O_3 to be visible in the x-ray diffraction pattern. All powders showed the identical photoluminescent emission spectrum when excited by 254 nm radiation. The peak wavelength is 504 nm, and the colour coordinates are x=0.08 and y=0.69. The invariance of the emission spectrum with cadmium content can be rationalized by considering the spinel structure. The crystallographic sites into which both the cadmium and manganese substitute, hence vacancies resulting from cadmium sublimation, never share a common oxygen, so the perturbation of the lattice introduced by cadmium processing is not felt by the manganese, and hence the emission wavelength is unaffected. However, the effect of cadmium content in the starting material does manifest itself in the PL intensity. The peak intensity was found for processed powders initially containing 10% CdO substituted into the starting materials. This enhanced luminescence is due to improved crystallization and manganese incorporation. Materials with higher initial cadmium contents exhibited a reduced brightness as the initial cadmium content increases. This is caused by the instability of the host in a reducing atmosphere resulting in the incorporation of manganese in undesirable phases which quench the luminescence.

The composition of films as deposited showed that films sputtered from 5% to

20% cadmium processed targets had excess Cd relative to the amount included in the starting materials for the targets, with cadmium content progressively approaching that of the target starting composition as target cadmium content increased. Films from 25% and 50% cadmium processed targets had the same stoichiometry as the starting materials, within the uncertainty of the measurement technique. Zinc content was always close to that of the target. This indicates a lower solubility for excess Cd in films closer in composition to $CdGa_2O_4$. EDX spectra of annealed films showed that all of the cadmium was lost during annealing in vacuum. Comparison of films annealed in air versus those annealed in vacuum showed only a slight loss in cadmium for the air annealed samples. The cadmium loss set the upper limit on the concentration of A-site vacancies within the spinel host. Long anneal times also resulted in the loss of zinc and subsequent loss of crystallinity, due to the instability of the spinel structure in the reducing atmosphere. PL measurements on thin films showed that the peak brightness coincided with the loss of all the cadmium from the films, indicating that manganese incorporation and improvements in the host crystal's microstructure are assisted by the higher diffusion rates due to the vacancies produced by Cd sublimation.

Films which were sputtered from the powders all crystallized in the spinel structure. Films sputtered from targets fabricated with no cadmium showed a significant enhancement in the intensity of the (111) diffraction line relative to the (311) which dominates the powder pattern. The effect of annealing the cadmium free films for progressively longer times or higher temperatures resulted in a decrease in the (111) line as the films approached a completely random grain orientation. The films from cadmium processed targets exhibited no preferred orientation upon deposition, indicating that the cadmium incorporated into these films enhanced the nucleation and growth of all crystal orientations. The intensity of the diffraction lines dropped dramatically for films annealed longer than 12 hours due to the Cd loss and decomposition of the spinel phase in the reducing atmosphere. The resultant phase(s) were either amorphous or the grain size was too small to form a diffraction pattern.

Films were examined by SEM and found to be heavily pitted. It was determined that this was due to exposed pores on the surface of the $BaTiO_3$ substrates. Films deposited on Si showed no pitting. When examined by AFM, the grain size of the film was found to be in the nanometre range. With increasing annealing temperature, time or larger amounts of cadmium in the starting materials the grain size of the films increased in step with the RMS roughness. For the cases of grain size versus temperature or time, the effect is at first small, then rises rapidly as the extremum was approached. In the case of cadmium processed films, the grain growth is a result of the vacancies left by Cd sublimation, enhancing diffusion and hence grain growth. This resulted in a steadily increasing grain size with increased cadmium use during processing. Grain size increased by approximately 25% under the anneal conditions required to obtain peak EL performance.

The EL performance showed strong trends with the variation in cadmium processing, annealing time and temperature. With temperature as the variable, the optimum performance was obtained by annealing between 875°C and 900°C. This was achieved for films sputtered from targets prepared with 5% to 15% cadmium, due to the improved crystallization imparted by the cadmium sublimation. The efficiency tended to peak between 850°C and 900°C, this despite the fact that the amount of transferred charge dropped continuously with temperature. This means that the drop in efficiency was due to the drop in luminance.

When the annealing time was varied, the luminance peaked at between 6 hours and 12 hours. Once again the optimum performance was for films sputtered from targets prepared with 5% to 15% cadmium. Beyond 12 hours the luminance dropped sharply due to the decomposition of the host. The trend in efficiency was similar, peaking at 12 hours before dropping off. Both the increase in efficiency and its subsequent drop off with time are due to a combination of luminance and transferred charge. The charge driven across the device shows a U-shape when plotted versus time, reaching a minimum value between 6 hours and 12 hours before rising agin. This is just the opposite of the luminance behaviour. The increase in transferred charge seen at long anneal times is due to the reduction of the host, resulting in free charge carriers at sub-threshold voltages.

When EL performance is plotted as a function of sputtering target the temperature trends are reinforced. Peak luminance occurs for films annealed between 875°C and 900°C from targets with low percentages of cadmium used during processing. Similar behaviour is seen for the efficiency. Transferred charge decreases slightly with increased initial target cadmium processing up to 20% at which point it jumps up. For samples annealed for increasing times, the best performance is for films from low percentages of cadmium used in processing annealed for 6 hours to 12 hours. The transferred charge once agin shows a U-shape, this time with cadmium processing level, reaching a minimum value at 12 hours in films fabricated from targets processed with 10-15% CdO. The dramatic rise in transferred charge in all cases is due to the reduction of the spinel and its decomposition products, all of which are conductive when fired under reducing conditions.

The EL decay time is also strongly dependent on processing conditions. The decay time varies slightly with temperature for films from targets processed with 15% CdO, however films with 25% CdO processed targets show first a rise from 1.9 ms at 750°C up to 2.8 ms at 900°C before dropping off. The dependence on cadmium processing is insignificant for 6 hour anneals, but varies by 1 ms for films annealed 24 hours. By far the most pronounced effect though is due to annealing time. Decay time peaks at 6 hours regardless of composition, indicating that the dopant incorporation is optimized at this anneal time.

This is the first time this materials system has been studied in thin film form. The substitution of cadmium for zinc in unannealed thin films has resulted in a significant decrease in the processing temperatures required for good electroluminescent performance, from over 1000°C to approximately 900°C. Despite the lower firing temperature, the luminance is still comparable to phosphors fired at the higher temperatures.

The performance of Cd processed $Zn_{1-x}Cd_xGa_2O_{4-x}$:Mn compares very favourably with current green EL phosphors such as $Zn_2Si_{0.5}Ge_{0.5}O_4$:Mn. The latter has a maximum emission at 528 nm and colour coordinates of x=0.20 and y=0.70. This emission is much yellower than the 504 nm emission of the gallate. Due to this more saturated green emission cadmium processed $ZnGa_2O_4$:Mn thin films show excellent potential as a green phosphor in either monochrome displays or, if combined with suitable red and blue phosphors, in full colour applications. This phosphor has the advantage of high chemical stability over the currently used sulphide phosphors such as ZnS:TbOF. It also exhibits its saturated green emission without the use of filters. The main drawbacks of the zinc gallate relative to zinc sulphide are the lower luminance and efficiency observed in this study, however both of these parameters can be improved through better processing and optimization.

7.3 Future Work

Cadmium processing has proven itself a useful tool for phosphor preparation, however many questions still remain. It is clear from the x-ray diffraction patterns that the powders contain excess gallium oxide. The films on the other hand show no lines from Ga_2O_3 despite the fact that all of the Cd has sublimed during annealing. This would seem to indicate that it is possible to introduce a substantially higher vacancy concentration in the films than the powders. A better understanding of the phase relationships in this materials system, and the details of the cadmium sublimation and host decomposition would be valuable. The manner in which the excess gallium oxide is incorporated should also be determined. It may remain exclusively on the B sublattice, or it could partially shift to the tetrahedral sites as is the case for excess Al^{3+} in $MgAl_2O_4$.

As a photoluminescent phosphor, cadmium processed zinc gallate has the advantage of requiring only a single firing in order to obtain bright luminescence. Optimization of th dopant concentration and firing process would further improve this phosphor.

As an EL device, it is also important to understand the long term stability of the films. If the high vacancy concentration is metastable, EL operation and performance may gradually degrade. Aging studies of the devices are needed in order to determine how useful these devices could be commercially. Different substrates should also be considered in order to determine the impact of the device structure and fabrication on the overall performance of this phosphor.

Finally, the manganese concentration has a dramatic impact on the brightness and efficiency of the device. Optimization of the manganese content would be necessary prior to the use of this phosphor in any application.

Appendix

EL Performance Figures

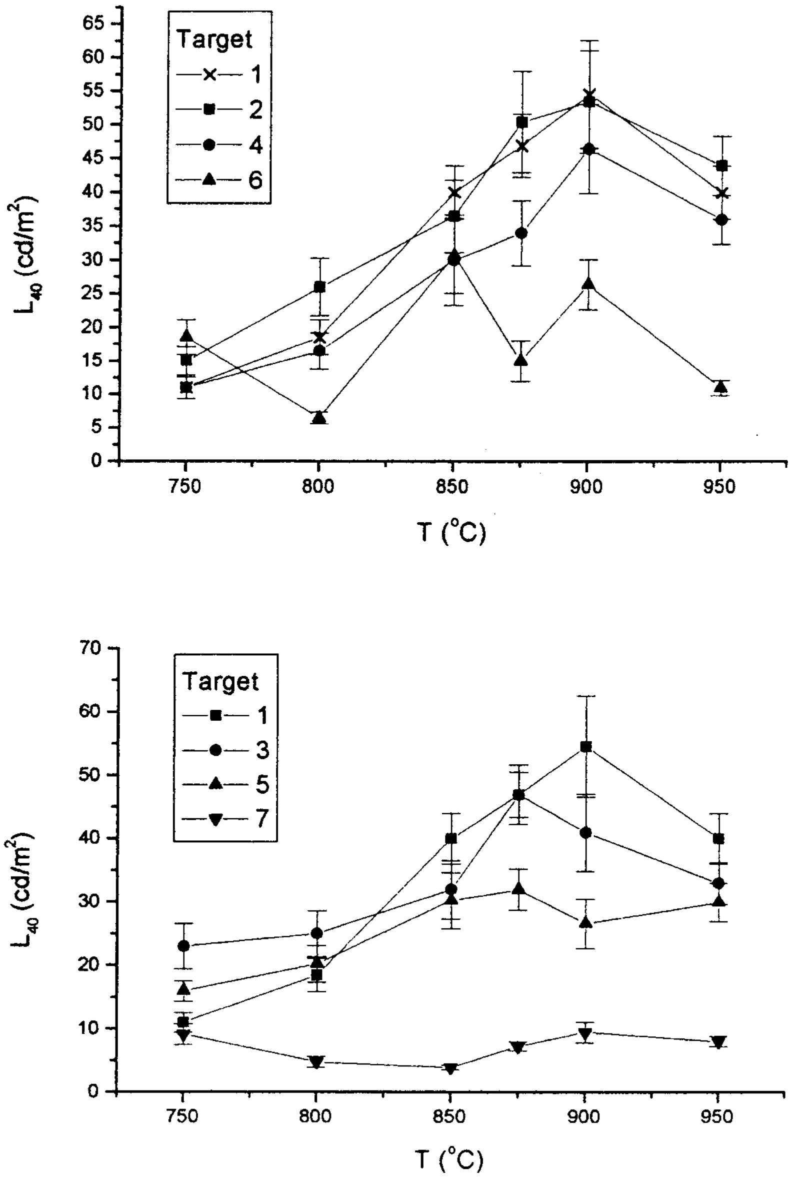

Figure A-1) EL brightness at 40 V above threshold as a function of annealing temperature for various cadmium contents at 60 Hz, showing the uncertainty in the measurements. Films were annealed for 12 hours.

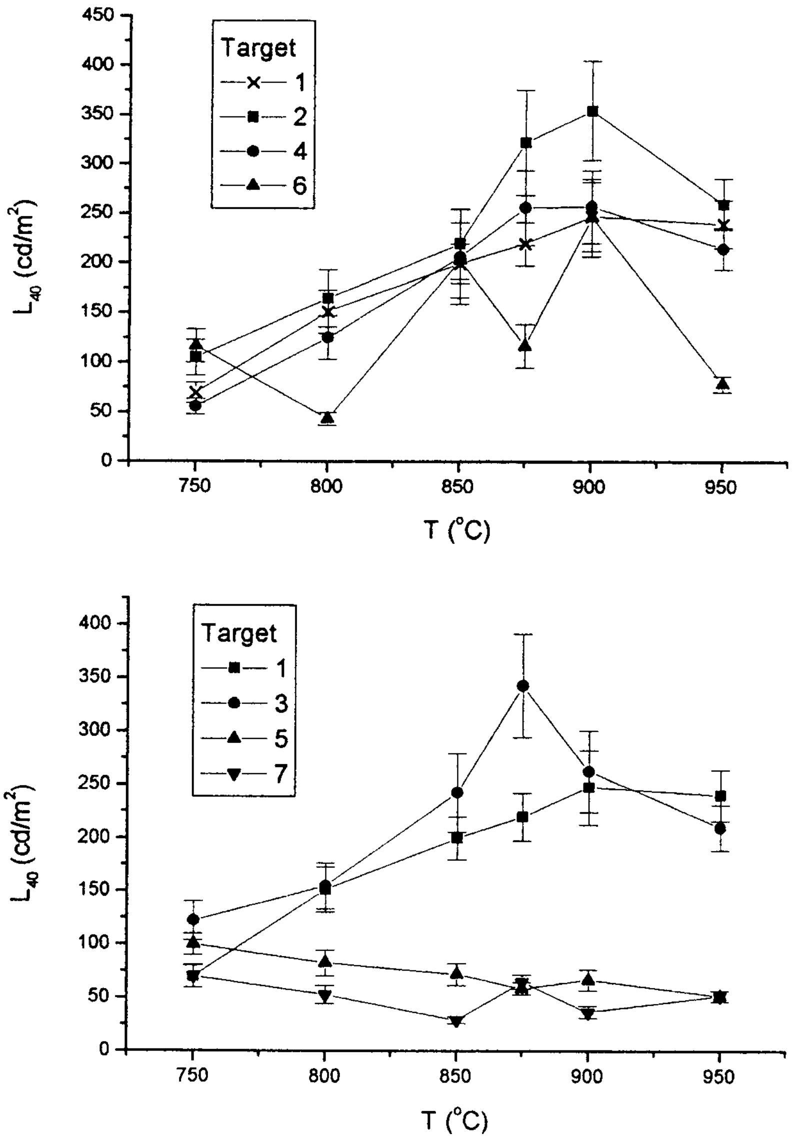

Figure A-2) EL brightness at 40 V above threshold as a function of annealing temperature for various cadmium contents at 600 Hz, showing the uncertainty in the measurements. Films were annealed for 12 hours.

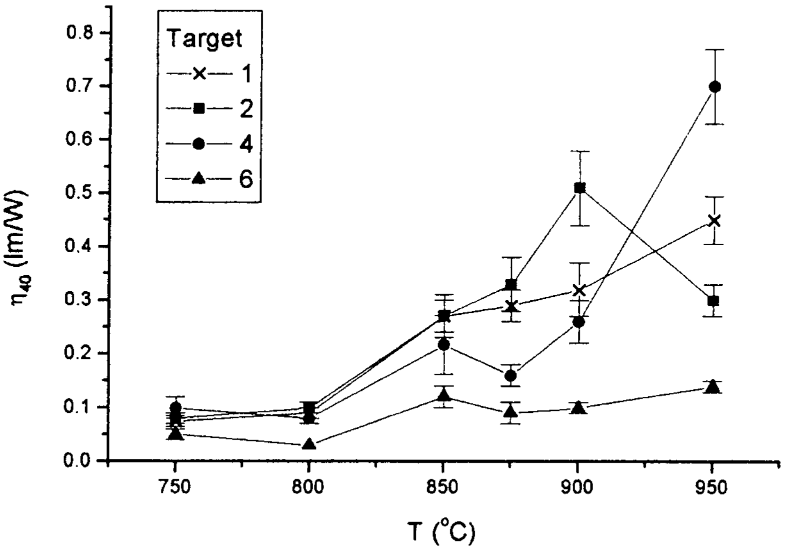

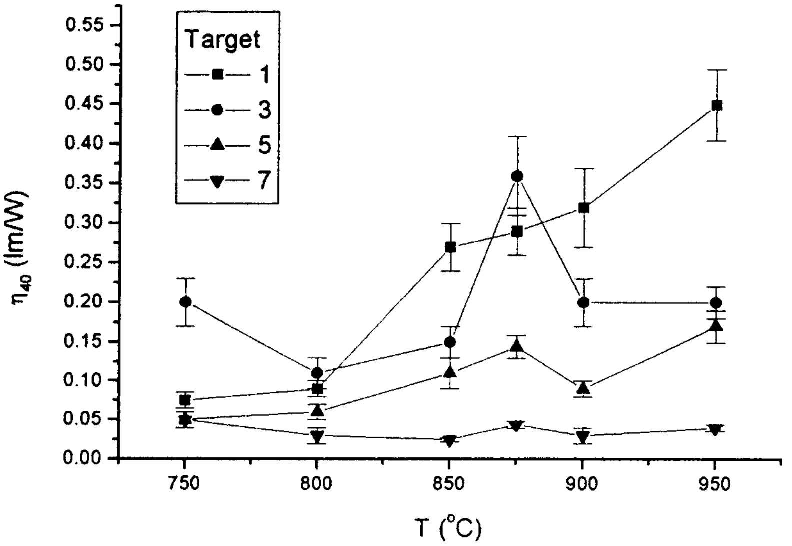

Figure A-3) EL efficiency at 40 V above threshold as a function of annealing temperature for various cadmium contents at 60 Hz, showing the uncertainty in the measurements. Films were annealed for 12 hours.

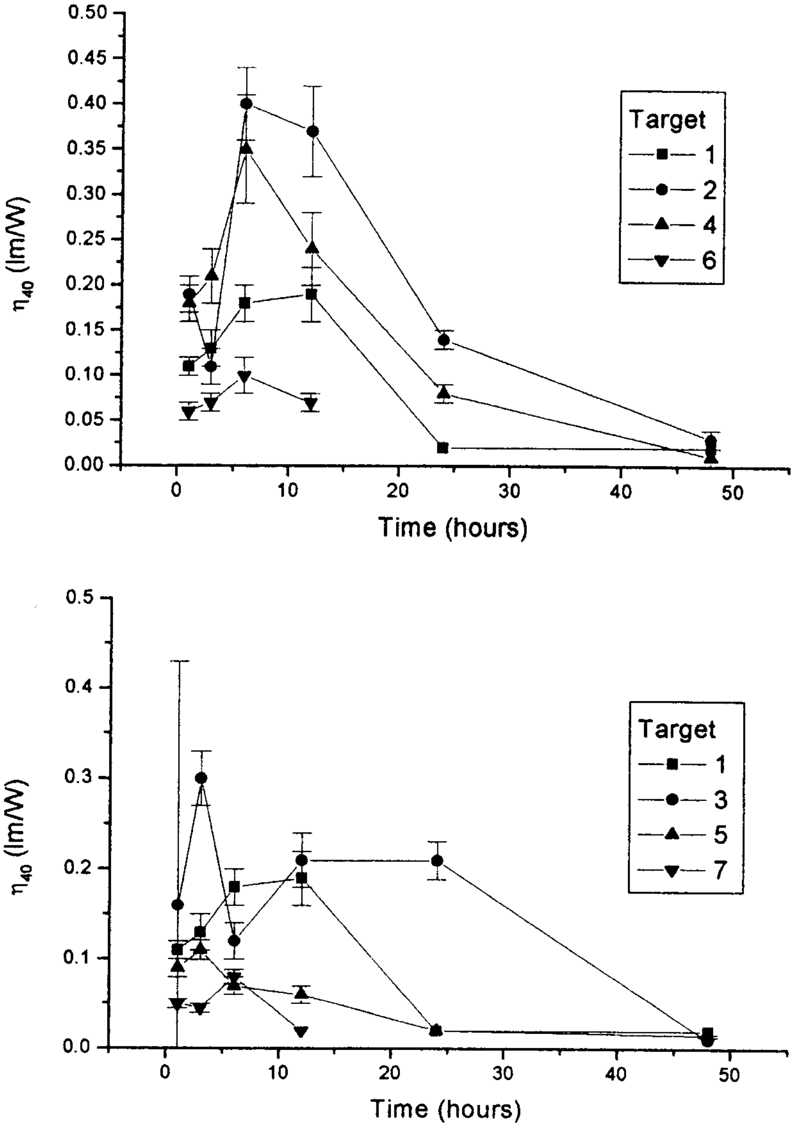

Figure A-10) EL efficiency at 40 V above threshold as a function of anneal time for various cadmium contents at 600 Hz, showing the uncertainty in the measurements. Films were annealed at 900°C.

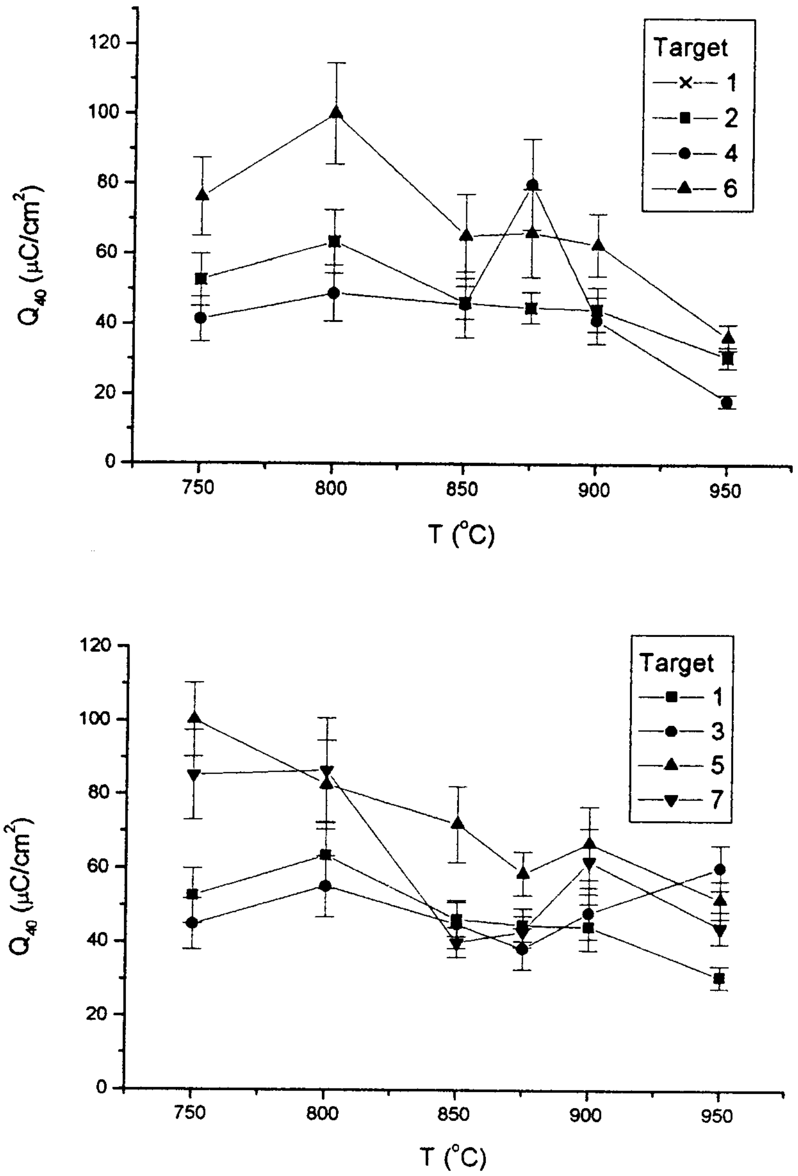

Figure A-5) Transferred charge at 40 V above threshold as a function of annealing temperature for various cadmium contents at 60 Hz, showing the uncertainty in the measurements. Films were annealed for 12 hours.

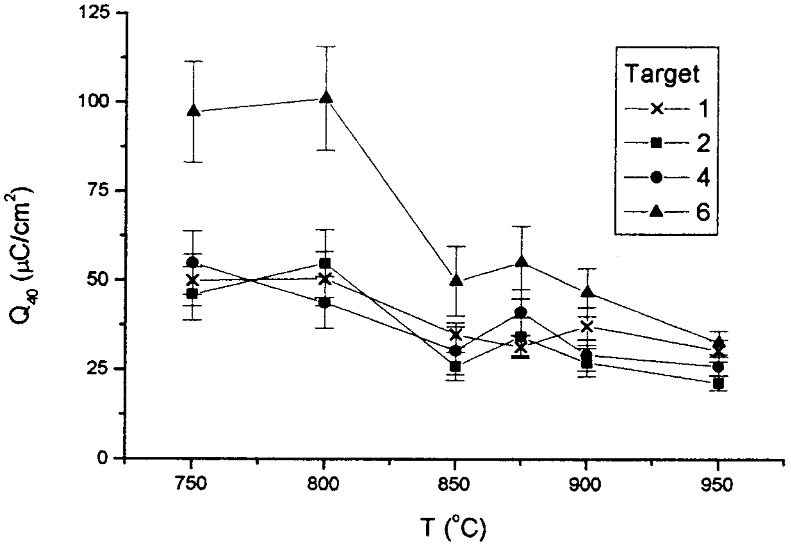

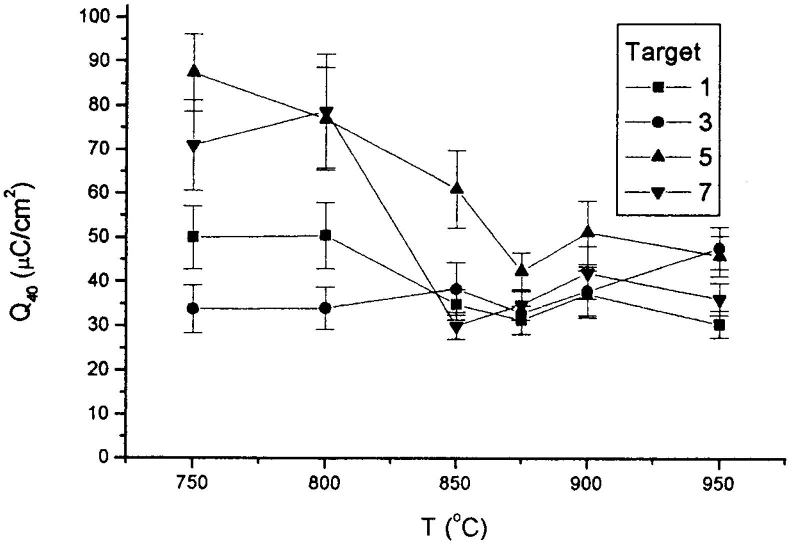

Figure A-6) Transferred charge at 40 V above threshold as a function of annealing temperature for various cadmium contents at 600 Hz, showing the uncertainty in the measurements. Films were annealed for 12 hours.

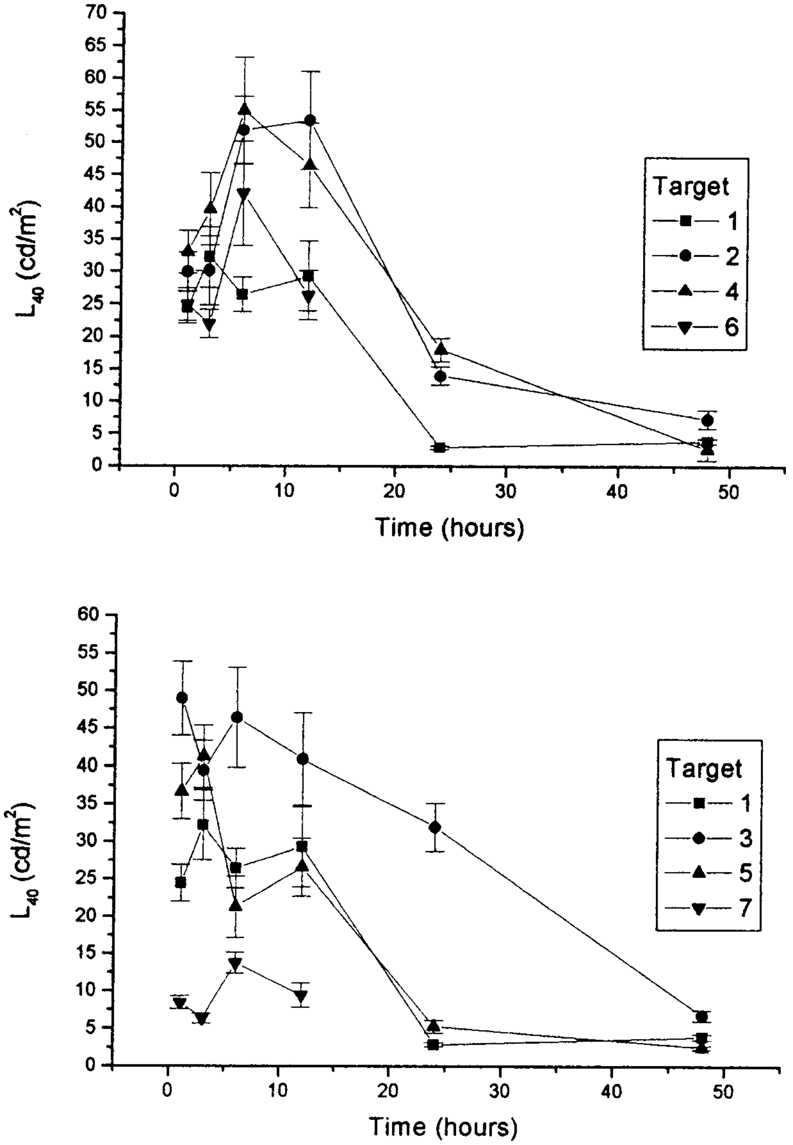

Figure A-7) EL brightness at 40 V above threshold as a function of anneal time for various cadmium contents at 60 Hz, showing the uncertainty in the measurements. Films were annealed at 900°C.

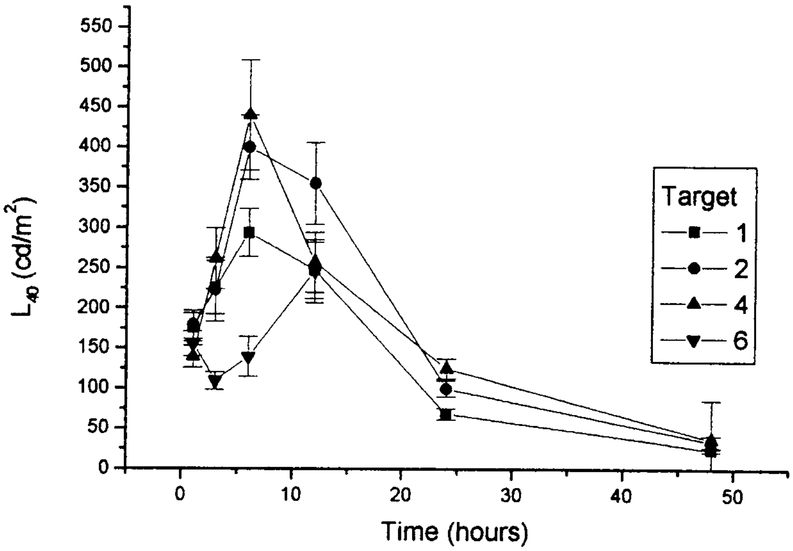

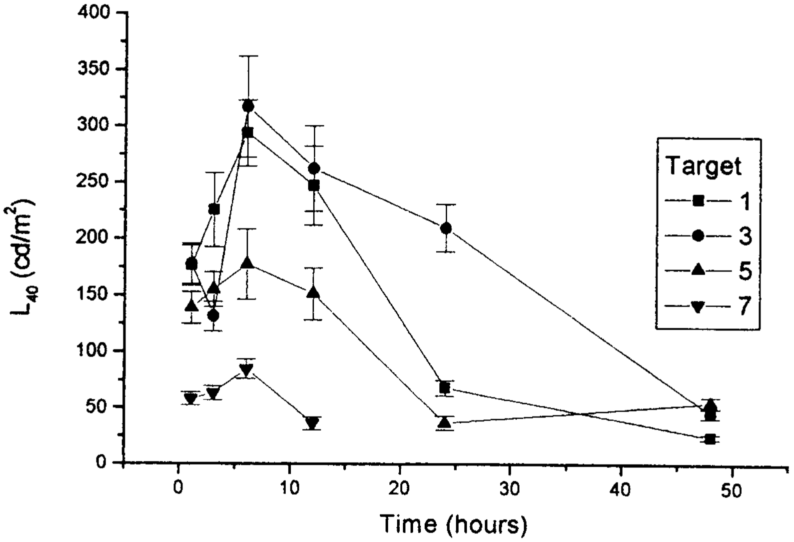

Figure A-8) EL brightness at 40 V above threshold as a function of anneal time for various cadmium contents at 600 Hz, showing the uncertainty in the measurements. Films were annealed at 900°C.

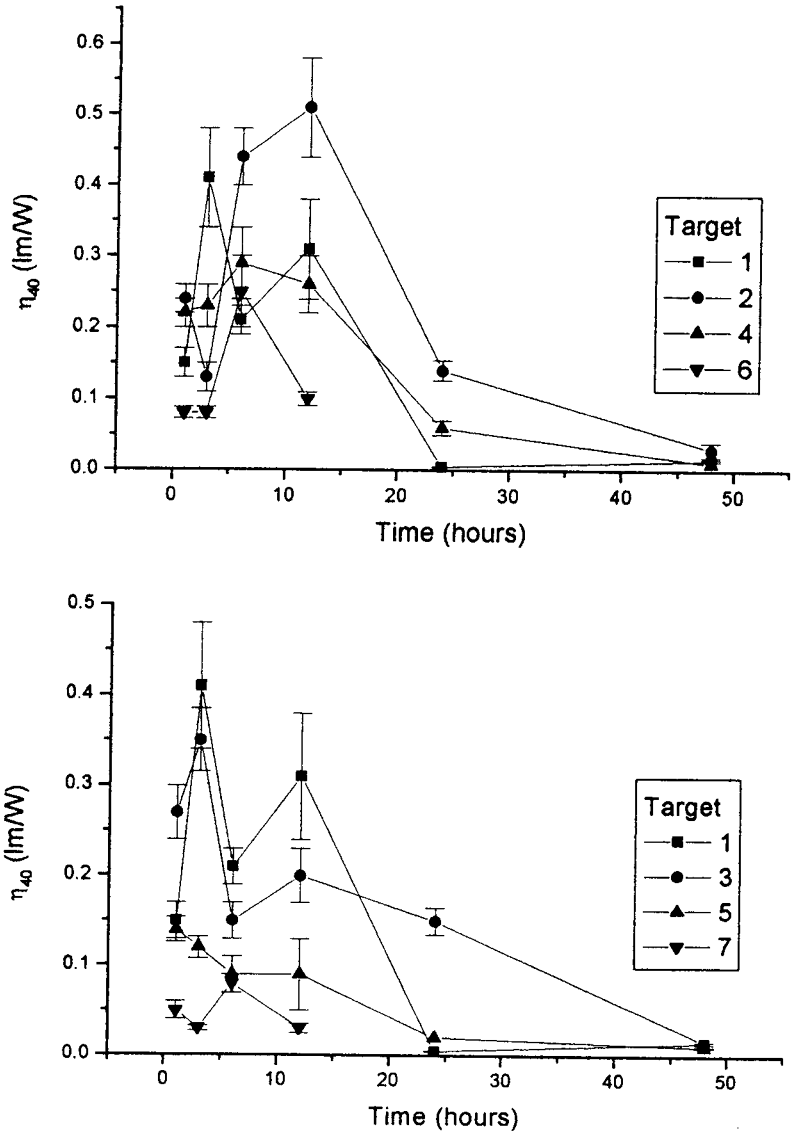

Figure A-9) EL efficiency at 40 V above threshold as a function of anneal time for various cadmium contents at 60 Hz, showing the uncertainty in the measurements. Films were annealed at 900°C.

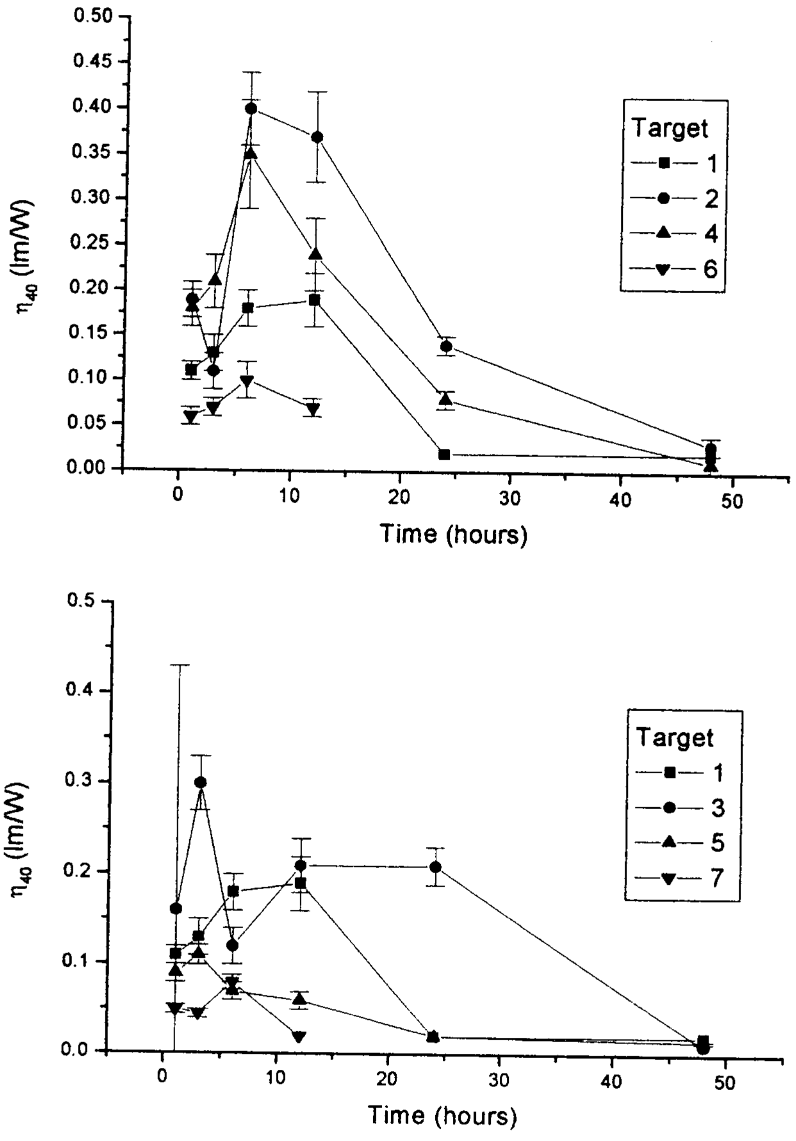

Figure A-10) EL efficiency at 40 V above threshold as a function of anneal time for various cadmium contents at 600 Hz, showing the uncertainty in the measurements. Films were annealed at 900°C.

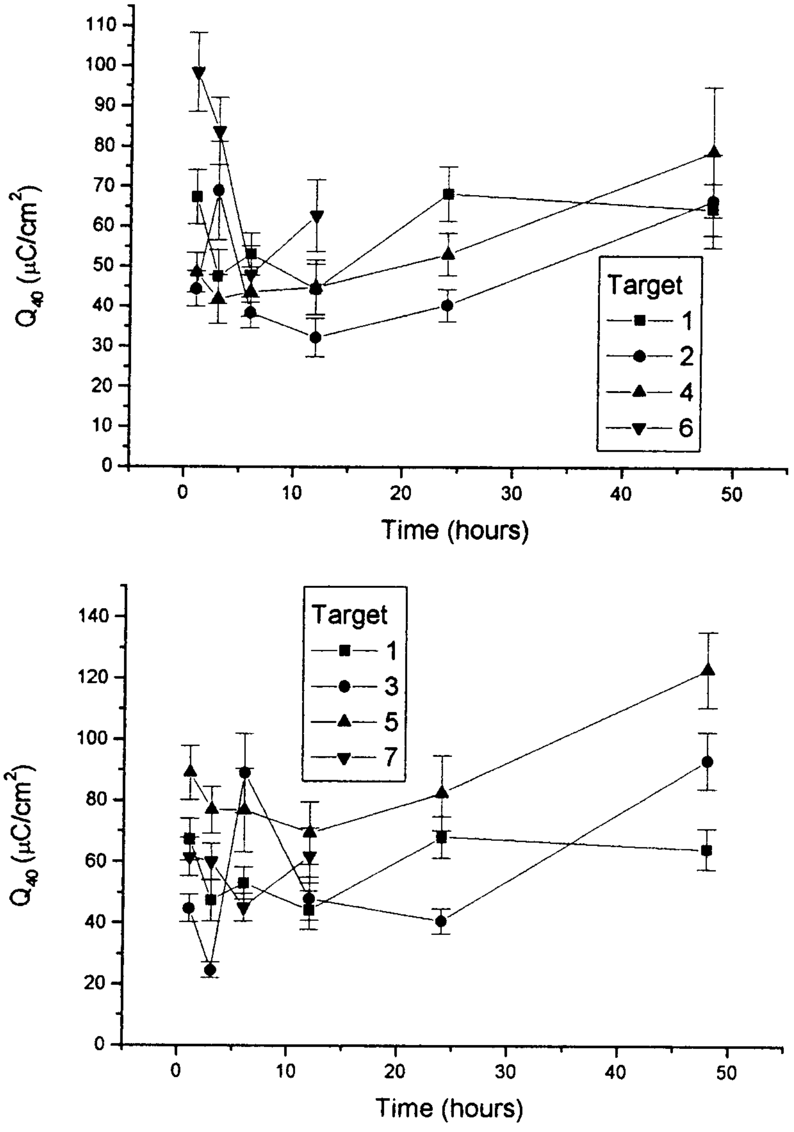

Figure A-11) Transferred charge at 40 V above threshold as a function of anneal time for various cadmium contents at 60 Hz, showing the uncertainty in the measurements. Films were annealed at 900°C.

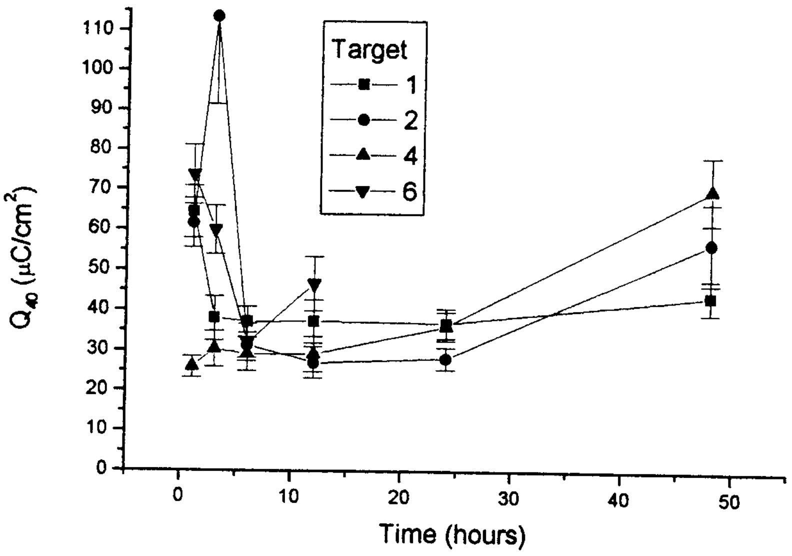

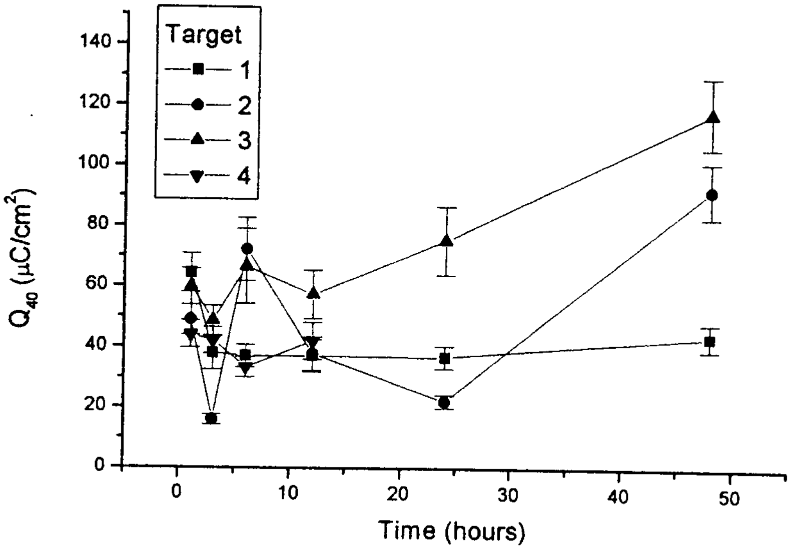

Figure A-12) Transferred charge at 40 V above threshold as a function of anneal time for various cadmium contents at 600 Hz, showing the uncertainty in the measurements. Films were annealed at 900°C.

References

Allen, J.W. (1989). *Springer Proc. In Physics 38, Proc. 4th Int. Workshop on Electroluminescence*, Springer-Verlag, Heidelberg, p.10.

Arean, C.O. and Diaz, E.G. (1982). *Mater. Chem.*, **7**, 675.

Atkins, P.W. (1978). Physical Chemistry, W.H. Freeman and Company, San Francisco.

Beauger, C., Grosseau, P., Guilholt, B., Huguenin, D. and Iacconi, P. (2000). *J. Therm. Anal. Calorim.*, **59**, 827.

Bender, J.P. and Wager, J.F. (2000). *6th International Conference on the Science and Technology of Display Phosphors, Extended Abstracts*, San Diego, CA, 69.

Bender, J.P., Wager, J.F., Kissick, J., Clark, B.L., and Keszler, D.A. (2002) *J. Lumin.*, **99**, 311.

Blasse, G. (1964). *Phillips Res. Repts.*, **3**, 1.

Bondar, V. (2000). *Mater. Sci. Eng.*, **B69-70**, 510.

Brehm, J.J. and Mullin, W.J. (1989). Introduction to the Structure of Matter, John Wiley and Sons, Toronto.

Buschendorf, F. (1931). *Z. phys. Chem.*, **14**, 300.

Carkner, D. and Kitai, A.H. (1992). *SID 1992 Digest*, **23**, 336.

Chase, E.W., Hepplewhite, R.T. Krupka, D.C. and Kahng, D. (1969). *J. Appl. Phys.*, **40,** 2512.

Choi, S.K., Moon, H.S., Mho, S.-I., Kim, T.W. and Park, H.L. (1998) *Mater. Res. Bull.*, **33**, 693.

Coovert, R.E., King, C.N. and Teunge, R.T.(1982). *SID Digest*, 128.

Cotton, F.A.,Advanced Inorganic Chemistry 2nd ed., John Wiley and Sons, London, 1966.

Datta, R.K. and Roy, R. (1968). *J. Am. Ceram. Soc.*, **51**, 297.

Destriau, G. (1936). *J. Chim. Physique*, **33,** 587.

Eisberg, R.and Resnick, R. (1985). Quantum Physics of Atoms, Molecules, Nuclei and Particles 2nd ed., John Wiley and Sons, Toronto.

Endo, T., Uheda, K. and Takizawa, H. (1996). Functionally Graded Materials, I. Shiota and M.Y. Miyamoto eds., Elsevier, Amsterdam, 701.

Fan, J.C.C. and Goodenough, J.B. (1977). *Appl. Phys. A*, **48**, 3524.

Flynn, C.P. (1972). Point Defects and Diffusion, Clarendon Press, Oxford, p. 66-67.

Goffin, J., Buffier, N. and Huber, M. (1961). *Compt. rend.*, **252**, 2744.

Hayes, W and Stoneham, A.M. (1985). Defects and Defect Processes in Nonmetallic Solids, John Wiley and Sons, Toronto.

Hill, R.J., Craig, J.R. and Gibbs, G.V. (1979). *Phys. Chem. Minerals*, **4**, 317.

Hsieh, I.J., Feng, M.S., Kuo, K.T. and Lin, P. (1994a). *J. Electrochem. Soc.*, **141**, 1617.

Hsieh, I.J., Chu, K.T., Yu, C.F. and Feng, M.S. (1994b). *J. Appl. Phys.*, **76**, 3735.

Hoffman, C.W.W. and Brown, J.J. (1968). *J. inorg. nucl. Chem.*, **30**, 63.

Hornstra, J. and Keulen, E. (1972). *Philips Res. Repts.*, **27**, 76.

Huber, M. (1959). Kinetics of High-Temperature Processes, W.D. Kingery ed., The Technology Press of the Massachusetts Institute of Technology and John Wiley and Sons, New York, 19.

Huber, M. and Bénard, J. (1965). *Bull. Soc. Chim. France*, 1081.

Imbusch, G.F. (1978). Luminescence Spectroscopy, M.D. Lumb ed., Academic Press, New York.

Inoguchi, T., Takeda, M., Kakihara, Y., Nakata, Y. and Yoshida, M.(1974). *SID Digest*, 84.

Irgaslev, T.I. and Sirazhiddinov, N.A. (1975). *Uzb. Khim. Zh.*, **19**, 7.

Itoh, S., Kimizuka, T. and Tonegawa, T. (1989). *J. Electrochem. Soc.*, **136**, 1819.

Itoh, S., Toki, H., Sato, Y., Morimoto, K. and Kishino, T. (1991). *J. Electrochem. Soc.*, **138**, 1509.

Jeong, I.-K., Park, H.L. and Mho, S.-I. (1998). *Solid State Comm.*, **105**, 179.

Jia, W., Liu, H., Huang, S., Wu, X., Lu, L. and Yen, W.M. (1995). *J. Electrochem. Soc.*, **142**, 1637.

Kahng, D. (1968). *Appl. Phys. Lett.*, **13**, 210.

Kawanishi, M., Miura, N., Matsumoto, H. and Nakano, R. (1999). *Proceedingd of the Sixth International Display Workshop*, 821.

Kim, Y.J., Jeong, Y.H., Kim, K.D., Kang, S.G., Lee, K.G., Han, J.I., Park, Y.K. and Cho, K.I. (1998). *J. Vac. Sci. Technol. B*, **16**, 1239.

Kim, S.G., Lee, S.H., Park, N.H., Park, H.L., Min, K.-W., Mho, S.-I., Kim, T.W. and Hwang, Y.H. (1999). *Solid State Comm.*, **110**, 515.

Kim, J.Y., Jeon, D.Y., Yu, I. and Yang, H.-G. (2000). *J. Electrochem. Soc.*, **147**, 3559.

King, C.N. (1996). In Inorganic and Organic Electroluminescence, R.H. Mauch and H.-E. Gumlich eds., Wissenschaftliche & Technik Verlag, Berlin.

Kingery, W.D., Bowen, H.K. and Uhlmann, D.R. (1976). Introduction to Ceramics, Second Edition, John Wiley & Sons, Toronto.

Kitai, A.H., Xiao, T., Liu, G. and Li, J.H. (1997). *SID 97 Digest*, **28**, 419.

Kitai, A.H., Zhang, Y., Ho, D., Stevanovic, D.V., Huang, Z., Nakua, A. and Cook, K.A. (1999) *SID 1999 Digest*, **30**, 596.

Krebs, J.J., Stauss, G.H. and Milstein, J.B. (1979). *Phys. Rev. B*, **20**, 2586.

Lee, Y.E., Norton, D.P., Park, C. and Pouleau, C.M. (2001). *J. Appl. Phys.*, **89**, 1653.

Leskelä, M., Li, W.-M. and Ritala, M. (2000) in Semiconductors and Semimetals vol. 65 : Electroluminescence II, G.O. Mueller ed., Academic Press, San Diego.

Lever, A.B.P. (1984) Inorganic Electronic Spectroscopy, Second Edition, Elsevier, Amsterdam .

Leverenz, H.W. (1950) An Introduction to Luminescence of Solids, Wiley, New York.

Mach, R. and Mueller, G.O. (1996). *Phys. Stat. Solidi A*, **81,** (1984) 609.

Mach, R., Schrottke, L., Mueller, G.O., Reetz, R., Ktause, E. and Hildish, L. (1988) *J. Lumin.*, **40 & 41**, 799.

Mach, R., Mueller, G.O., Schrottke, L., Benalloul, O. and Benoit, J. (1990) In *Proc. 5th International Workshop on EL*, Helsinki; *Acta Polytech. Scand.* **17**, 161.

Minami, T. (1998). *4th International Conference on the Science and Technology of Display Phosphors, Extended Abstracts*, Bend, OR, 195.

Minami, T., Miyata, T., Takat, S. and Fukuda, I. (1990). *Jpn. J. Appl. Phys.*, **36**, L117.

Minami, T., Miyata, T., Takata, S.and Fukuda, I. (1991). *Jpn. J. Appl. Phys.*, **30**, L117.

Minami, T., Maeno, T., Kuroi, Y. and Takata, S. (1995) *Jpn. J. Appl. Phys.*, **34**, L684.

Minami, T., Kuroi, Y. and Takata, S. (1996). *J. Vac. Sci. Technol. A*, **14**, 1736.

Minami, T., Yamada, H., Kubota, Y. and Miyata, T. (1997a). *Jpn. J. Appl. Phys.*, **36**, L.1191.

Minami, T., Kuroi, K., Miyata, T., Yamada, H. and Takata, S. (1997b). *J. Lumin.*, **72-74**, 997.

Müller, G.O. (2000) in Semiconductors and Semimetals vol. 65 : Electroluminescence II, G.O. Mueller ed., Academic Press, San Diego.

Müller, G.O., Mach, R., Reinsperger, G.U. and Schulz, G. (1991) *Proc. SID*, San Diego, 16.

Müller-Mach,R., Müller, G.O. and Nakua, K. (1996). *2nd International Conference on the Science and Technology of Display Phosphors*, San Diego, CA, p. 91.

Müller-Mach, R., Müller, G.O., Fouassier, C., Garcia, A., Fa, X.W., Zhong, G.Z., Zhao, L.J. and Sun, J.M. (1999). In *3rd International Conference on the Science and Technology of Display Phosphors*, Huntington, CA

Nanto, H., Minami, T., Murakami, S. and Takata, S. (1988). *Thin Solid Films*, **164**, 363.

Narita, K. (1999). Phosphor Handbook, S. Shionoya and W.M. Yen eds., CRC Press, Boston.

Ono, Y.A., Kawakami, H., Fuyama, M. and Onisawa, K. (1987). *Jpn. J. Appl. Phys.*, **26**, 1482.

Ono, Y.A. (1993). Encyclopaedia of Applied Physics vol. 5, VCH Publishers Inc., New York.

Ono, Y.A. (1995). Electroluminescent Displays, World Scientific, Singapore.

Orgel, L.E. (1955). *J. chem. Phys.*, **23** 1004.

Park, S., Clark, B.L., Keszier, D.A., Bender, J.P., Wager, J.F., Reynolds, T.A. and Herman, G.S. (2002) *Science*, **297**, 65.

Poort, S.H.M., Cetin, D., Meijerink, A. and Blasse, G. (1997). *J. Electrochem. Soc.*, **144**, 2179.

Porta, P., Stone, F.S. and Schiavello, M. (1974). *J. Solid State Chem.*, **11**, 135.

Porta, P. and Anichini, A. (1980) *J.C.S. Faraday I*, **76**, 2448.

Rack, P.D. and Holloway, P.H.,(1998) *Mat. Sci. and Eng.*, **R21** 171.

Roy, D.M., Roy, R. and Osborn, E.F. (1953). *American Journal of Science*, **251**, 337.

Rudorff, W. and Reuter, B.Z. (1947). *Z. anorg. Chem.*, **253**, 194.

Sharp, A.G. (1992). Inorganic Chemistry 3rd ed., Longman Scientific and Technical, Singapore.

Shea, L.E. (1993) $ZnGa_2O_4$ and $ZnGa_2O_4:Mn^{2+}$ for Potential Use in Vacuum Fluorescent Displays, Thesis, Virginia Polytechnic Institute and State University.

Shea, L.E., Datta, R.K. and Brown, J.J. (1994). *J. Electrochem. Soc.*, **141**, 1950.

Schiessl, W., Potzel, W., Karzel, H., Steiner, M., Köfferlein, M., Kalvius, G.M., Melzer, M., Dietzmann, G., Martin, A., Halevy, I., Gal, J., Schäfer, W., Will, G., Mitchell, D.W. and Das, T.P. (1994) *Hyp. Int.*, **90**, 359.

Sickafus, K.E. and Wills, J.M. (1999). *J. Am. Ceram. Soc.*, **82**, 3279.

Sze, S.M (1985). Semiconductor Decices, Physics and Technology, Wiley, New York.

Tannas, L.E. (1985). Flat Panel Displays and CRTs, Von Nostrand Reinhold Company, New York.

Takeda, M., Kanatani, Y., Kishishita, H. And Uede, H. (1983). *Advances in Display Technology III*, Proc. SPIE, **386**, 34.

Tanabe, Y. and Sugano, S. (1954a). *J. phys. Soc. Japan*, **9**, 753.

Tanabe, Y. and Sugano, S. (1954b). *J. phys. Soc. Japan*, **9**, 766.

Tanaka, S., Kobayashi, H. and Sasakura, H. (1999). Phosphor Handbook, S. Shionoya and W.M. Yen eds., CRC Press, Boston.

Tran, T.K., Park, W., Tomm, J.W., Wagner, B.K., Jacobsen, S.M., Summers, C.J., Yocom, P.N. and McClelland, S.K. (1995). *J. Appl. Phys.*, **78**, 5691.

Ueda, N. and Hosono, H. (1997). *Appl. Phys. Lett., 70, 3561.*

Vecht, A., Werring, N.J. and Smith P.J.F. (1968). *Brit. J. Appl. Phys.*, **1,** 134.

Vecht, A., Smith, D.W., Chadha, S.S., Gibbons, C.S., Koh, J. and Morton, D. (1994). *J. Vac. Sci. Technol. B*, **12**, 781.

Von Hippel, A.R. (1954). Dielectrics and Waves, John Wiley and Sons, New York.

Wendschuh-Josties, M., O'Neill, H.St.C., Bente, K. and Brey G. (1995). *N. Jb. Miner. Mh.*, **6**, 273.

West, A.R. (1988). In Basic Solid State Chemistry, John Wiley and Sons, Toronto, p. 248.

Wu, X. (1996). In Inorganic and Organic Electroluminescence, R.H. Mauch and H.-E. Gumlich eds., Wissenschaftliche & Technik Verlag, Berlin.

Wyckoff, R.W.G. (1965). Crystal Structures vol.3, Interscience, New York.

Xiao, T., Kitai, A.H., Liu, G. and Nakua, A. (1997a). *SID 1997 Digest*, **28**, 415.

Xiao, T. and Kitai, A.H. (1997b). *Proc. SID*, Toronto, 310.

Yoshino, H., Ohura, M., Kurokawa, S. and Onishi, H. (1992). *Japan Display 1992*, 737.

Yu, C.F., Lin, P. (1996a). *J. Appl. Phys.*, **79**, 7191.

Yu, C.F., Lin, P. (1996b). *Jpn. J. Appl. Phys.*, **35**, 5726.